INVESTIGATING TRACT-SPECIFIC CHANGES IN WHITE MATTER WITH DIFFUSION TENSOR IMAGING

By

Lori R. Arlinghaus

Dissertation

Submitted to the Faculty of the

Graduate School of Vanderbilt University

in partial fulfillment of the requirements

for the degree of

DOCTOR OF PHILOSOPHY

in

Biomedical Engineering

May, 2009

Nashville, Tennessee

Approved:

Professor Adam W. Anderson

Professor Malcolm J. Avison

Professor Benoit M. Dawant

Professor John C. Gore

Professor Sohee Park

ACKNOWLEDGMENTS

I have several people to thank for their support throughout my time as a graduate student. First, I would like to thank my advisor, Dr. Adam W. Anderson, for his guidance, knowledge, and patience. It has been a pleasure working with him. I would also like to thank the members of my dissertation committee, Dr. Malcolm J. Avison, Dr. Benoit M. Dawant, Dr. John C. Gore, and Dr. Sohee Park, for their time and helpful input.

The work presented here is the result of collaborations with Dr. Dawant, Dr. Elisabeth Dykens, Dr. Herbert Meltzer, and Dr. Park, and funding was provided by NARSAD and the National Institutes of Health (NIH/NIBIB 1RO1-EB02777). I would like to thank Dr. Herbert Meltzer and Patrick Gallagher in the Department of Psychiatry and Dr. Park, Crystal Gibson, Dr. Junghee Lee, and Dr. Natasha Matthews in the Department of Psychology for their help with the schizophrenia study. I would like to thank Dr. Elisabeth Dykens, Rebecca Kossler, Miriam Lense, Elizabeth Roof, and Dr. Tricia Thornton-Wells for their help with the Williams syndrome study. Dr. Dawant, Rui Li, Xia Li, and Dr. Yong Li from the Medical Image Processing laboratory in the Department of Electrical Engineering and Computer Science provided the image registration software used in these projects, as well as extremely helpful advice, for which I am grateful.

I would like to thank several other people who have helped me along the way: Robin Avison, Donna Butler, Dr. Zhaohua Ding, Nancy Hagans, and Dr. Yonggang Lu from the Institute of Imaging Science, Janiece Harrison from the Department of Biomedical Engineering, and Dr. E. Brian Welch, Ronald Holthuizen, and Dr. Frank Hoogenraad from Philips Healthcare.

Finally, I would not be where I am today without the immense support and encouragement I have received from my family. Words cannot express how gateful I am for everything my parents have done for me over the years and for my fiancé, Jeff, who kept me smiling and kept me from getting lost in the details. Thank you.

TABLE OF CONTENTS

LIST OF TABLES

Table Page

LIST OF FIGURES

LIST OF ABBREVIATIONS AND SYMBOLS

Δ	Diffusion time
δ	Diffusion gradient duration
γ	Gyromagnetic ratio
$\lambda_{\parallel}$	Axial diffusivity
$\lambda_{\perp}$	Radial diffusivity
D	Diffusion coefficient
G	Gradient amplitude
ADC	Apparent diffusion coefficient
AL	Left arcuate fasciculus
AR	Right arcuate fasciculus
b0	Non-diffusion-weighted b-value
CL	Left cingulum
CR	Right cingulum
CSF	Cerebrospinal fluid
CYLN2	Cytoplasmic Linker 2
DLPFC	Dorsolateral prefrontal cortex
DTI	Diffusion tensor images/imaging
DWI	Diffusion weighted images/imaging
EC	External capsule
FA	Fractional anisotropy
FACT	Fiber assignment by continuous tracking
fMRI	Functional magnetic resonance imaging
FZD9	Frizzled 9
IDL	Interactive Data Language
IFO	Inferior fronto-occipital fasciculus

IFOL	Left inferior fronto-occipital fasciculus
IFOR	Right inferior fronto-occipital fasciculus
ILF	Inferior longitudinal fasciculus
LIMK1	LIM kinase 1
MR	Magnetic resonance
MTG	Middle temporal gyrus
NC	Normal controls
PDD	Principal diffusion direction
PF	Prefrontal
PGSE	Pulsed gradient spin echo
PLIC	Posterior limb of the internal capsule
RF	Radio frequency
ROI	Region of interest
SE	Spin echo
SENSE	Sensitivity encoding
SLF	Superior longitudinal fasciculus
STG	Superior temporal gyrus
STX1A	Syntaxin 1A
SZ	Schizoprhenic
TBA	Tract-based analysis
TBSS	Tract-based spatial statistics
UF	Uncinate fasciculus
UL	Left uncinate fasciculus
UR	Right uncinate fasciculus
VBA	Voxel-based analysis
WM	White matter
WS	Williams syndrome

CHAPTER I

INTRODUCTION

Diffusion tensor imaging (DTI) [1] is the first *in vivo* imaging technique to provide the contrast necessary to distinguish between separate axonal tracts within white matter (WM) tissue in the brain and provide information regarding the microstructure of the tracts. Because of this, DTI has become a popular neuroimaging tool with a wide variety of clinical applications, ranging from normal WM maturation [2] and aging [3] to diseases and disorders, such as Huntington's Disease [4], epilepsy [5], multiple sclerosis [6], Alzheimer's disease [7], and schizophrenia [8].

The issue of how best to analyze these rich data sets has become an increasingly important question, particularly as the number of group studies increases. Currently, the two most common means of analyzing DTI data are region of interest (ROI) and voxel-based analyses (VBA) of scalar diffusion parameter maps derived from the tensor data. Alternative methods involving fiber tracking to isolate specific tracts and compare diffusion parameters along [9–11] or within [12] the tracts have been proposed and are gaining popularity.

As the number of subjects in DTI studies increases, manual ROI placement in individual data sets becomes increasingly time-consuming and prone to error. VBA methods minimize user interaction; however, these methods are highly dependent on accurate co-registration of images to a standard space, which is not always possible given the current limits on DTI resolution and inter-subject anatomic variability. Inaccurate registration can lead to false-positive results along the edges of structures and ambiguity in determining which WM pathways are affected. Tract-based analysis (TBA) methods offer the possibility of isolating the same WM structure fairly accurately. However, the methods currently used suffer from limitations, such as manual identification of seed points for tracking, which can be time consuming for large studies, and challenges in determining point correspondence between subjects.

The specific aims of this research project were to (1) develop a tract-based analysis method

that could be used on a broad range of tracts with minimum user interaction, (2) compare the new method to traditional analysis methods, and (3) apply it to clinical applications.

This dissertation is organized in the following manner: First, a brief review of DTI and the analysis methods used in DTI studies is provided. The first manuscript, “Altered diffusion properties in white matter in Williams Syndrome,” presents a VBA study of WM diffusion properties in Williams syndrome. The results of this study reveal several regions of both decreased and increased FA in the Williams syndrome group compared to normal controls, consistent with the current literature and supporting the idea that axonal organization is altered in this disorder. This study also demonstrates some of the limitations of a traditional VBA analysis. The second manuscript, “Semi-automated, tract-based analysis of diffusion tensor imaging studies,” describes new methods developed for performing tract-based analysis of DTI data. These methods were applied to a schizophrenia study, and the results were compared to the results of a standard VB analysis of the data. The comparison revealed that the TBA method may be able to help overcome some of the shortfalls of VBA and help in distinguishing which WM tracts are involved in changes discovered by this method. The third manuscript, “Lateralized differences in white matter tracts passing through the external capsule in Williams syndrome” describes the application of TBA to investigate the WM changes found in the external capsules of the Williams syndrome subjects in the VBA study. The study examines fractional anisotropy along the two major WM tracts that pass through the regions-of-interest defined by the first study and shows that the tracts may have unique contributions to the changes found in the VBA study. Finally, a summary of the work presented in this dissertation and discussion of the methods and results is provided in the final chapter.

References

[1] Basser, P. J. and Pierpaoli, C. Microstructural and physiological features of tissues elucidated by quantitative-diffusion-tensor MRI. *Journal of Magnetic Resonance. Series B*, 111(3):209–19, June 1996.

[2] Baratti, C., Barnett, A. S., and Pierpaoli, C. Comparative MR Imaging Study of Brain Maturation in Kittens with T1, T2, and the Trace of the Diffusion Tensor. *Radiology*, 210(1):133–142, 1999.

[3] Pfefferbaum, A. et al. Age-related decline in brain white matter anisotropy measured with spatially corrected echo-planar diffusion tensor imaging. *Magnetic Resonance in Medicine*, 44(2):259–68, 2000.

[4] Reading, S. A. et al. Regional white matter change in pre-symptomatic Huntington's disease: A diffusion tensor imaging study. *Psychiatry Research*, 140(1):55–62, 2005.

[5] Gupta, R. K. et al. Diffusion tensor imaging in late posttraumatic epilepsy. *Epilepsia*, 46(9):1465–71, 2005.

[6] Kealey, S. M., Kim, Y., Whiting, W. L., Madden, D. J., and Provenzale, J. M. Determination of multiple sclerosis plaque size with diffusion-tensor MR Imaging: comparison study with healthy volunteers. *Radiology*, 236(2):615–20, 2005.

[7] Lee, B. C. P., Mintun, M., Buckner, R. L., and Morris, J. C. Imaging of Alzheimer's disease. *Journal of Neuroimaging*, 13(3):199–214, July 2003.

[8] Kanaan, R. A. et al. Diffusion tensor imaging in schizophrenia. *Biological Psychiatry*, 58(12):921–9, 2005.

[9] Mori, S. et al. Imaging cortical association tracts in the human brain using diffusion-tensor-based axonal tracking. *Magnetic Resonance in Medicine*, 47(2):215–23, 2002.

[10] Fillard, P., Gilmore, J., Piven, J., Lin, W., and Gerig, G. *Quantitative Analysis of White Matter Fiber Properties along Geodesic Paths*. Medical Image Computing and Computer-Assisted Intervention. 2003.

[11] Smith, S. M. et al. Tract-based spatial statistics: voxelwise analysis of multi-subject diffusion data. *Neuroimage*, 31(4):1487–505, 2006.

[12] Jones, D. K. et al. Age effects on diffusion tensor magnetic resonance imaging tractography measures of frontal cortex connections in schizophrenia. *Human Brain Mapping*, 27(3):230–8, March 2006.

CHAPTER II

BACKGROUND & MOTIVATION

Review of diffusion tensor imaging

Theory

Diffusion-tensor imaging [1] is based upon the observations of Hahn [2] and Carr and Purcell [3] that spin echo (SE) magnetic resonance (MR) sequences are sensitive to diffusion of the molecules being probed and the introduction of the pulsed gradient spin echo (PGSE) sequence [4], which allows the measurement of diffusion coefficients, such as that of water (3×10^{-9} m^2/s at 37° C). In the PGSE sequence (Figure 2.1), two gradient pulses are applied, one on either side of the 180° radio frequency (RF) pulse and each with amplitude G and duration δ. The net effect of these gradient pulses is the labeling of protons in molecules with a phase related to the distance the molecules have moved during the time Δ between the application of the two pulses. This net phase results in the attenuation of the signal (S). For the PGSE sequence, assuming unrestricted, isotropic diffusion and taking hardware limitations into account, the signal attenuation due to the diffusion of protons at the time of the echo (TE) depends upon the diffusion coefficient D and an attenuation factor b [5]:

$$\frac{S(TE)}{S_0} = \exp(-bD) \tag{2.1}$$

where $S(TE)$ is the signal at the time TE, S_0 is the signal when $G = 0$, and

$$b = \gamma^2 G^2 \delta^2 (\Delta - \delta/3) \tag{2.2}$$

Since the values of γ (the gyromagnetic ratio) , G , δ , and Δ are known, the diffusion coefficient (D) of the sample being imaged can be solved for by obtaining two images: one with diffusion gradients $(G \neq 0)$ and one without diffusion gradients $(G = 0)$ applied.

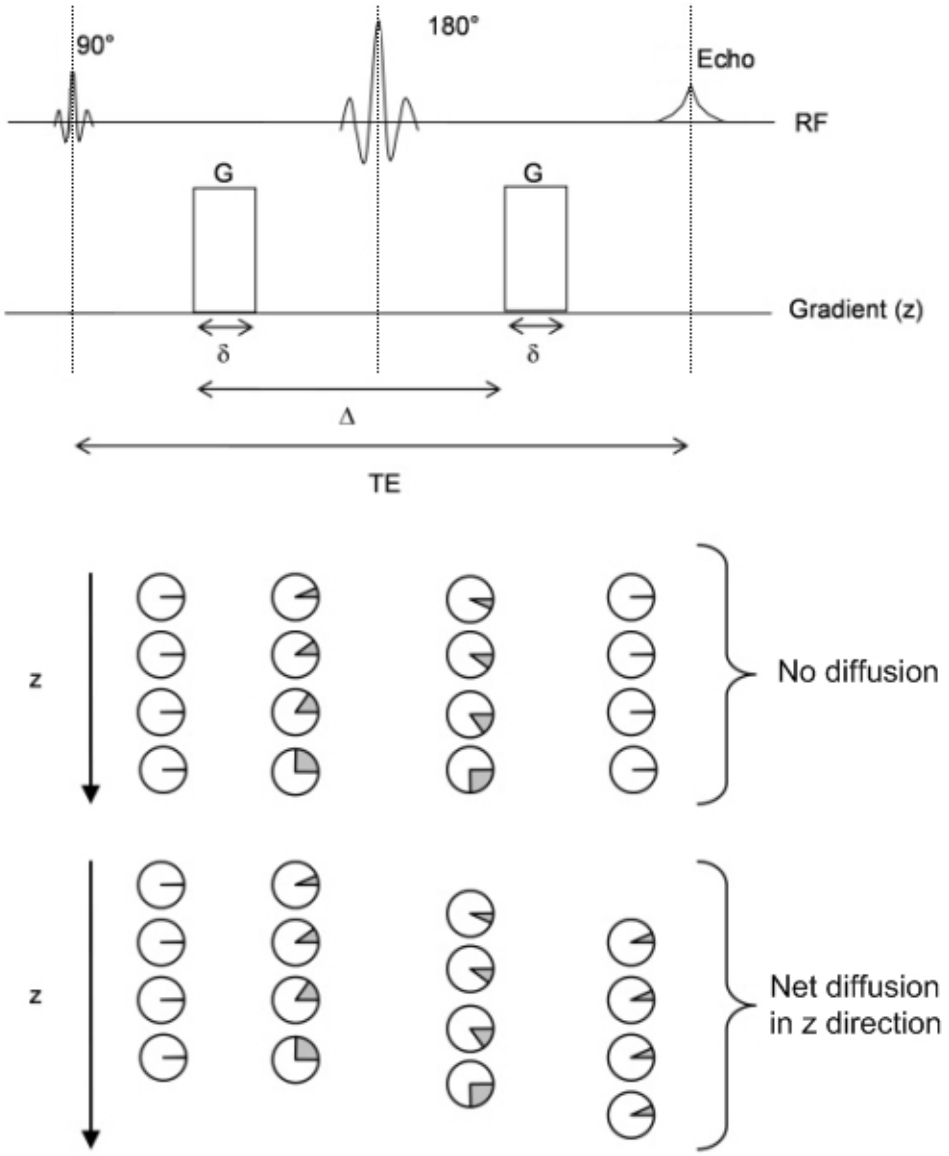

Figure 2.1: The pulse sequence diagram for a PGSE experiment (*Top*) and schematics demonstrating the effects of the sequence on spins that do not diffuse (*middle*) and spins that do diffuse (*bottom*) during the diffusion encoding time Δ. The spins initially have no phase, then the first diffusion sensitizing gradient (G) applies a location-dependent phase to each spin. The spins are allowed to diffuse, and a 180° RF pulse is applied, reversing the phase of each spin. The spins diffuse for a total time period Δ, when a second diffusion sensitizing gradient (G) is applied. If the spins have not moved from their original locations (*middle*), they have no net phase at the time of the signal readout. If the spins have moved (*bottom*), they will have a net phase change that is related to the net distance they have moved along the direction of the diffusion sensitizing gradients.

Equations (2.1) and Eq. (2.2) assume that the sample being imaged is homogeneous, allowing unrestricted, isotropic diffusion; therefore, the diffusion encoding only needs to be applied in one direction to accurately estimate the value of D. However, this is not the case when imaging complicated samples, such as living tissue. Microstructures, such as cell walls, organelles, and microtubules, hinder the diffusion of water, reducing the value of the observed or apparent diffusion coefficient (ADC) depending upon the organization of the microstructures and the direction of the applied diffusion gradient.

The dependence of the measured ADC on the direction of the applied gradient can be taken advantage of to reveal information related to the structure of highly organized tissue, such as muscle fibers and white matter tracts in the brain. If diffusion gradients are applied along a minimum of six non-collinear directions not all in the same plane, the ADC can now be represented as a tensor matrix $\mathbf{D}$ [6]. Equation (2.1) now takes the form

$$\frac{S(TE)}{S_0} = \exp(-\sum_{i=1}^{3}\sum_{j=1}^{3} b_{ij}D_{ij}), \tag{2.3}$$

where $\mathbf{b}$ is a matrix composed of the individual b-values for each diffusion-weighted direction and D_{ij} is the corresponding ADC value. $\mathbf{D}$ is a symmetric matrix:

$$\mathbf{D} = \begin{bmatrix} D_{xx} & D_{xy} & D_{xz} \\ D_{yx} & D_{yy} & D_{yz} \\ D_{zx} & D_{zy} & D_{zz} \end{bmatrix}, \tag{2.4}$$

where

$$D_{xy} = D_{yx}, \tag{2.5}$$

$$D_{xz} = D_{zx}, \text{and} \tag{2.6}$$

$$D_{yz} = D_{zy}, \tag{2.7}$$

leaving six independent elements, which can be solved for using multivariate linear regression [6]. Each tensor can then be diagonalized to obtain the eigenvectors ($\vec{e}_1, \vec{e}_2,$ and $\vec{e}_3$) and eigenvalues ($\lambda_1, \lambda_2,$ and λ_3), which characterize the direction and magnitude, respectively, of the three-dimensional diffusion displacement distribution within that voxel. The displacement distribution is often represented as an ellipsoid with axes defined by the eigenvectors, and the lengths of the axes are defined by the eigenvalues or effective diffusivities. The shape of the ellipsoid provides information about the diffusion within that voxel (Fig. 2.2). If diffusion is isotropic ($\lambda_1 = \lambda_2 = \lambda_3$) the ellipsoid

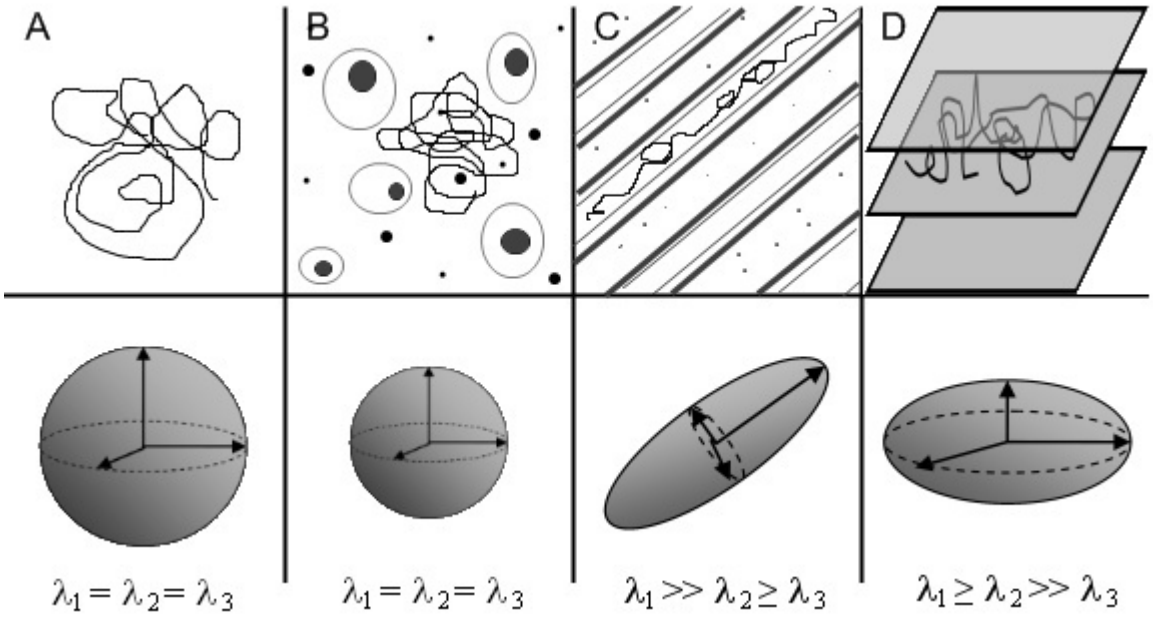

Figure 2.2: Effects of tissue microstructure on the diffusion tensor. The diffusion displacement distribution for each voxel can be visualized as an ellipsoid, and its size and shape are affected by the local tissue microstructure: (A) CSF, (B) grey matter, (C) highly organized tissue such as bundles of myelinated WM axons, and (D) tissue organized in sheets or in regions where two sets of WM axons cross.

will be a sphere. If diffusion is restricted to primarily one direction ($\lambda_1 \gg \lambda_2 \geq \lambda_3$), the shape of the ellipsoid will be prolate. If diffusion is restricted to a plane ($\lambda_1 \geq \lambda_2 \gg \lambda_3$), the shape of the ellipsoid will be oblate. The shape of the tensor can be used to infer information about the organization of the

structures within the tissue being imaged. For example, a bundle of tightly packed myelinated axons running in parallel will hinder the diffusion of both intracellular and extracellular water molecules in the directions perpendicular to the axis of the bundle. Assuming axonal properties are isotropic in the plane, diffusion will be greatest in one direction and the resulting tensor will have a prolate shape.

Diffusion parameters

Information about the underlying structure of the tissue can also be revealed by several rotationally invariant scalar values derived from the tensor. The most commonly used values are the trace of the diffusion tensor [6], the mean diffusivity, and fractional anisotropy [1]. Example images

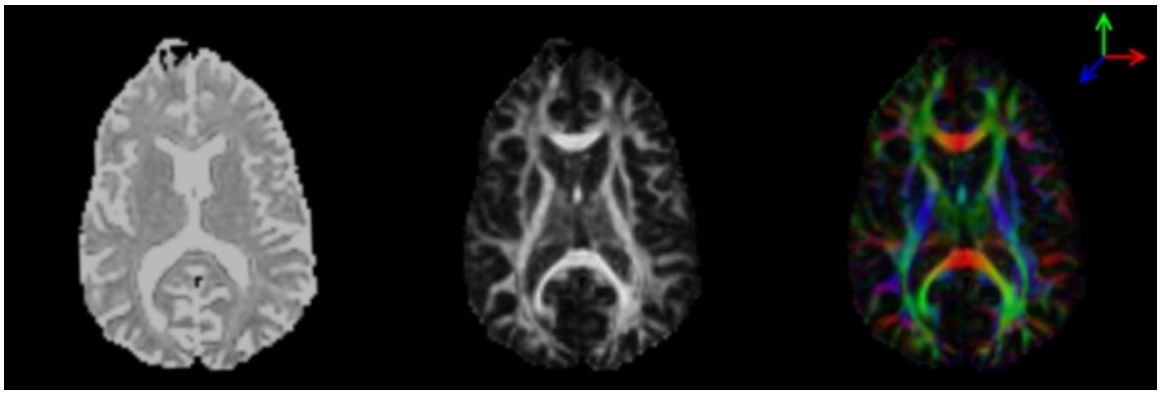

Figure 2.3: Diffusion parameter maps. From left to right, $Tr(\mathbf{D})$, FA, and color-coded FA maps are shown.

of these parameters are shown in Figure 2.3. The trace of $\mathbf{D}$, $Tr(\mathbf{D})$, is the sum of the eigenvalues, giving a measure of the total diffusivity:

$$Tr(\mathbf{D}) = \lambda_1 + \lambda_2 + \lambda_3. \tag{2.8}$$

The mean diffusivity (MD) is just the average of the effective diffusivities ($\overline{\lambda}$):

$$\overline{\lambda} = \frac{Tr(\mathbf{D})}{3} \tag{2.9}$$

Fractional anisotropy (FA) is an index of the variation of diffusion over measurement directions. It is defined as

$$FA = \frac{\sqrt{3}}{\sqrt{2}} \frac{\sqrt{(\lambda_1 - \overline{\lambda})^2 + (\lambda_2 - \overline{\lambda})^2 + (\lambda_3 - \overline{\lambda})^2}}{\sqrt{\lambda_1^2 + \lambda_2^2 + \lambda_3^2}}, \tag{2.10}$$

and it ranges from 0 for isotropic diffusion to 1 for completely anisotropic diffusion restricted to one direction. Color-coded FA maps provide contrast within highly anisotropic tissue based upon the principal diffusion direction, where red represents greatest diffusion in the right/left direction, green represents anterior/posterior, and blue represents inferior/superior.

These indices are sensitive to pathological changes in the underlying tissue structure, such as demyelination/remyelination [7–9], axonal degeneration [9, 10], and edema [11–13]. MD and anisotropy measures are also sensitive to differences in the organization of healthy tissue. For example, within healthy white matter tissue, FA is high in regions where the axon bundles are traveling in the same direction and low in regions where different white matter tracts are crossing paths.

The eigenvalues themselves may also be useful in determining what is happening in the underlying tissue. Axial diffusivity ($\lambda_{\|}$) is the diffusivity associated with the principal eigenvector:

$$\lambda_{\|} = \lambda_1. \tag{2.11}$$

It describes the diffusivity parallel to the major orientation of the underlying tissue. Radial diffusivity ($\lambda_{\perp}$) is the average of the second and third eigenvalues:

$$\lambda_{\perp} = \frac{\lambda_2 + \lambda_3}{2}. \tag{2.12}$$

It describes the diffusivity perpendicular to the major orientation of the underlying tissue. Song *et al.* [7, 10] have shown in animal models that $\lambda_{\parallel}$ and $\lambda_{\perp}$ are sensitive to specific types of changes to white matter microstructure. They reported that $\lambda_{\perp}$ is sensitive to changes in the myelination of axons but $\lambda_{\parallel}$ is not [7] and that $\lambda_{\parallel}$ is sensitive to axonal degeneration, while $\lambda_{\perp}$ is not [10].

Fiber Tractography

Fiber tractography (or fiber tracking) makes use of the orientation information inherent in the eigenvectors of the diffusion tensor to track WM bundles in DT images. The first fiber tracking algorithms were based upon the principal diffusion direction (PDD) method, a deterministic tracking method which uses line propagation along the direction of the principal eigenvectors [14, 15]. A popular PDD tracking algorithm is fiber assignment by continuous tracking (FACT) [15]. This method begins tracking from a seed point in the image, and propagates along the direction of the major eigenvector of that voxel by a specified step size. When the fiber enters a new voxel, the propagation direction of the fiber is adjusted to match the major eigenvector of that voxel, and so on until a threshold criterion, such as a minimum FA value or a maximum angle between consecutive PDDs, is violated.

Streamline approaches, such as FACT and other PDD methods, have several limitations. They are susceptible to noise in the principal eigenvector and may terminate tracking prematurely in regions of low anisotropy due to crossing fibers pathways. There is not enough information in a single tensor model for these algorithms to know which path to follow. Probabilistic approaches have been developed which create maps of the probability of the connectivity between brain regions [16–18], based upon the uncertainty in the measurement of the principle eigenvector. These methods attempt to allow for the branching of fiber pathways. A major criticism of many probabilistic methods is that they make assumptions regarding the source of the noise in the tensor estimation, leaving out the potential impact of physiological noise and image artifacts. Nonparametric bootstrap methods, such as [18], do not make assumptions regarding the source of the uncertainty. However, they require large data sets, which greatly increase imaging and processing time.

Clinical applications

As mentioned previously, the diffusion tensor and the parameters derived from it are sensitive to changes in the integrity and organization of tissue microstructure, particularly in highly organized tissue, such as muscle and WM. Early on, the usefulness of this imaging modality was recognized in the study of normal WM development [19] and aging [20], as well as diseases affecting myelination, such as multiple sclerosis [21] and Krabbe disease [22]. Eventually, DTI became a popular tool for the investigation of involvement of changes in WM structure and organization in diseases and disorders where demyelination was not the primary manifestation. The work in this dissertation focuses on two such disorders: schizophrenia and Williams syndrome.

Schizophrenia

Schizophrenia is a debilitating, chronic mental disease that affects approximately 1% of the population world-wide and over two million Americans [23]. The symptoms vary from patient to patient, but generally fall into one of three categories: positive (hallucinations and delusions), negative (apathy, lack of emotion, and poor social functioning), and disorganization of thought, speech, or behavior. Schizophrenia was distinguished from other forms of psychosis at the end of the 19th century [24], and several regions of the brain, including the frontal lobe, temporal lobe, cerebellum, and structures of the limbic system, are thought to be involved in the disease. However, the underlying mechanisms producing the disease's diverse symptoms are still poorly understood.

Post-mortem study of the brains of schizophrenic patients was the first method used to investigate the effects this disease might have on anatomy. However, these studies were only able to reveal gross changes in anatomy. More recently, computed tomography and magnetic resonance imaging (MRI) techniques have been used to study gross changes in WM volume of schizophrenics in vivo. However, the results of these studies range from negative [25, 26] to regional [27–29] to global [30, 31] differences.

Recently, disconnection theories [32, 33] have been introduced, which suggest that the integration of information across complex networks between functional areas of the brain is compromised

in schizophrenia. While Friston & Frith [32] originally proposed that the abnormality was functional and not anatomical in nature, it was certainly appealing to think of this 'disconnection' as arising from abnormalities in the physical connections of the brain. Indeed, histological evidence has revealed differences in dendritic arborization [34, 35], decreased number of dendritic spines [36, 37], increased neuronal density, which suggests a decrease in interneuronal neuropil [38, 39], decreased oligodendrocyte density [40] and myelin-related protein expression [41], and impaired myelination of axons [42, 43] in schizophrenic brains. Dendrites, oligodendrocytes and other glial cells in the neuropil, and myelin all contribute to the transmission of signals between neurons. Evidence of their involvement in schizophrenia, along with the development of disconnection theories, has initiated considerable interest in studying WM tracts *in vivo*. Particular interest has developed around the tracts that connect regions of the brain previously implicated in schizophrenia. These include the cingulum, which is part of the limbic system, the uncinate fasciculus, which connects the frontal and temporal lobes, the arcuate fasciculus, which connects the language regions in the frontal and temporal lobes and is part of the superior longitudinal fasciculus, as well as others.

DTI has become a popular tool in recent studies of schizophrenia, with well over 100 studies published in the past 10 years. (See Figure 2.4 for the number of publications per year.) The majority of the studies examined differences in MD and/or FA between patient groups and normal controls and found a variety of regions in major WM tracts where these parameters differed between the groups. It has been shown that at least 20 diffusion directions are necessary for accurate estimation of anisotropy measurements [44]. Therefore, the following review will focus on results from studies performed with at least 20 diffusion encoding directions.

Association pathways have been investigated extensively in DTI studies of schizophrenia. In chronic schizophrenic patients, mean diffusivity was found to be increased [45] and mean FA decreased [46, 47] in the bilateral anterior portion of the cingulum. Decreased FA was reported in the left cingulum only in chronic schizophrenic patients [48] and in patients with early onset schizophrenia [49]. No significant changes were found in either the right or left cingulum in several studies [50–55]. The superior longitudinal fasciculus (SLF) contains the arcuate fasciculus, which

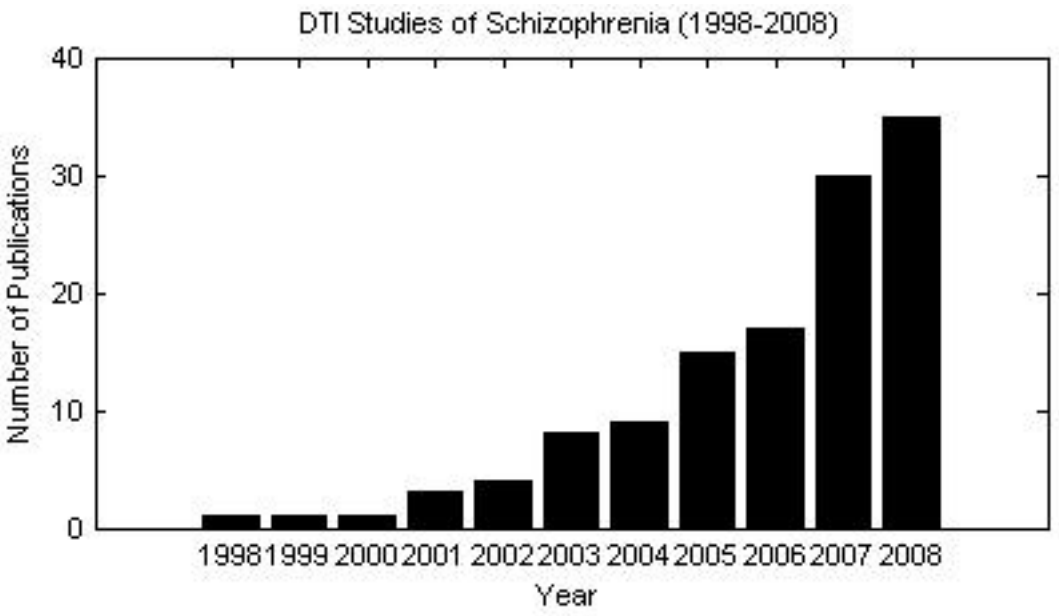

Figure 2.4: DTI studies of schizophrenia by year.

has been suggested to be involved in auditory hallucinations [56]. Studies have reported that patients have reduced FA in the left SLF only [48, 51, 52, 54, 55], right SLF only [45, 53], and both right and left SLF [54, 57]. Four whole-brain studies did not report changes in either SLF tract [45, 49, 50, 58]. Decreased FA in the bilateral uncinate fasciculi has been reported in studies of recent onset schizophrenics [55] and typical schizophrenic populations [57, 59]. Jones *et al.* and Price *et al.* [51, 60] reported no significant differences in FA in the uncinate fasciculi of typical schizophrenics, and several other whole-brain studies did not report any significant differences in the uncinate [45, 48–50, 52–54, 58]. In the inferior fronto-occipital (IFO) fasciculi, decreased FA was reported in the left tract [55, 58] and bilaterally [57]. No differences in FA or MD were found in either tract in several studies [45, 48–54, 59]. Only two studies found any significant differences in FA in the inferior longitudinal fasciculus (ILF). Cheung *et al.* reported reduced FA in the left ILF of first-episode, never-medicated schizophrenics [58], and Shergill *et al.* reported reduced FA in the bilateral ILF [54].

In addition to these association tracts, decreased FA has been reported in projection pathways involved in motor and sensorimotor function [48, 52, 53, 58]. Also, changes in the major WM

tract connecting the two hemispheres of the brain have been reported. In a group of early-onset schizophrenics, Douaud *et al.* [52] found decreased FA in the corpus callosum ranging from the genu to the splenium. Three studies found reduced FA in the genu [54, 61, 62]. However, Kanaan *et al.* [61] reported conflicting results between two analysis methods, where one method found the difference to be significant and the other did not, and two other studies found no significant differences in FA in the genu [46, 58]. Two whole-brain comparison studies found decreased FA in the splenium of the corpus callosum [50, 58], yet two studies focusing on the splenium found no significant differences [46, 62].

Williams syndrome

Williams syndrome (WS) is a disorder caused by a 1.5Mb hemizygous deletion on chromosome 7 (7q11.23) [63]. This deletion results in a unique set of characteristic physical, cognitive, and behavioral symptoms. These include characteristic facial features, such as a wide mouth with full lips and protrusive ears[64], and cardiovascular abnormalities [64, 65]. Individuals with WS typically exhibit mild mental retardation along with a unique combination of relative cognitive strengths and weaknesses, such as excellent verbal short-term memory and poor visuospatial construction [66]. These individuals also typically demonstrate excessive friendliness and empathy [67, 68], non-social anxiety [69], and sensitivity to loud noises [70]. Genetic evidence along with structural and functional differences in WS patients compared to normal controls suggest that the physical connections between certain functional areas in the brain may be disrupted in WS.

The typical WS deletion includes several genes that are potentially involved in neural development and function, including LIM kinase 1 (LIMK1), cytoplasmic linker 2 (CYLN2), frizzled 9 (FZD9), and syntaxin 1A (STX1A). The LIMK1 gene encodes a protein that is involved in growth cone motility and morphology and consequently, neurite extension [71, 72]. Growth cones are processes located at the tips of developing axons, and they are sensitive to environmental cues, which they use to guide the axons to their proper destinations. Disruption of the normal signaling pathway involving

LIMK1, may result in improper axonal guidance, potentially leading to neural and cognitive dysfunction. An LIMK1 knockout mouse model demonstrated altered growth cone morphology, altered fear responses, and impaired spatial learning [73]. The CYLN2 gene encodes for CLIP-115 [74] which is involved in the regulation of the dynamics between microtubules and specific neuronal organelles important to neuronal function [75]. Disruption of this gene in mouse models resulted in abnormalities including increased ventricular volume, decreased volume of the corpus callosum, impairment of motor coordination, and hippocampal dysfunction [76]. The FZD9 gene encodes for a protein that acts as a receptor for Wnt signaling proteins [77], which regulate the development of neural structures, including the hippocampus [78]. A study investigating the effects of deletion of the FZD9 gene on the hippocampus revealed increased apoptotic cell death in the developing dentate gyrus and deficits in visuospatial learning and memory [79]. STX1A plays an important role in neurotransmitter release [80] and upregulation of the protein has been shown to be involved in hippocampal learning processes [81]. While it is tempting to look for one-to-one correlations between genes and specific cognitive functions, it is likely that there exists a complex interaction between genes and between these genes and the environment.

Structural MRI studies of the WS brains have revealed several differences compared to normal brains, including reduced grey matter volume [82–85], reduced white matter volume [82, 86], increased gyrification [86–88], reduced sulcal depth in the intraparietal sulcus [89, 90], and a reduction in the extent of the central sulcus [91, 92].

Jackowski *et al.* pointed out that the studies published to date do not reveal whether these abnormalities are due to WS or general mental retardation [93]. However, a study comparing high-functioning WS participants with IQ-matched controls found bilateral grey matter reductions in the intraparietal sulcus and the orbitofrontal cortex, as well as around the third ventricle [83]; and it has been reported that both high-functioning WS participants [89] and WS participants with mental retardation [90] exhibit reduced sulcal depth in the intraparietal sulcus. These studies suggest that at least some of the cognitive dysfunction in WS is unique to the disorder and not a result of general mental retardation.

Functional MRI studies demonstrate disruption of several functional circuits potentially related to the cognitive symptoms demonstrated in WS. Normal activation of the ventral processing stream during face processing has been reported [83, 94, 95], which is in agreement with behavioral data suggesting that face processing is relatively preserved in WS [96]. However, regions that may be involved in higher-level object recognition and face processing have been shown to function abnormally [94, 95], suggesting that compensatory processing methods may be invoked, providing relatively persevered face and object recognition. Studies targeting abnormal social cognition in WS, such as decreased inhibition responses, increased non-social anxiety, and hypersociability, have shown abnormal functioning in WS subjects in cortical and subcortical regions in frontostriatal circuits involved in response inhibition [97] and in the amygdala, orbitofrontal cortex, dorso-lateral prefrontal cortex, and medial prefrontal cortex during the presentation of fearful faces and scenes [98]. Meyer-Lindenberg *et al.* studied high-functioning WS subjects and reported dysfunction of the dorsal stream processing in visuospatial construction [83] and a lack of normal activation in the anterior hippocampal formation, which is an area involved in spatial navigation and potentially visuospatial construction [99].

All of this evidence has led to an interest in investigating the involvement of WM in the disorder. Two DTI studies of WS have been published to date. Marenco *et al.* [100] studied 5 high-functioning WS subjects recruited from the group used in previous fMRI studies [83, 99] and 5 normal controls matched for age, gender, and IQ. The orientation of the principal eigenvector ($\vec{e}_1$) averaged over bilateral regions of WM surrounding the orbito-frontal cortex, collateral sulcus, intraparietal sulcus, and ventral cingulum was found to be directed more in the anterior-posterior direction than the right-left direction in the WS group compared to controls. Anisotropy, measured by the lattice index [101], was found to be decreased in the cortico-spinal tracts (CST) and increased in the inferior-longitudinal fasciculi (ILF) and the inferior fronto-occipital fasciculi (IFO) in WS compared to controls. The shape of the diffusion distribution profile, measured by skewness of the tensor [102], was found to be increased in the CST and decreased in the ILF, IFO, and ventral cingulum. No differences

in anisotropy or skewness were found in the anterior thalamic radiations, dorsal cingulum, uncinate fasciculi, or genu and splenium of the corpus callosum.

Hoeft *et al.* [103] used a voxel-wise analysis and two types of region of interest analysis to investigate differences in WM between 10 WS, 10 developmentally delayed controls and 11 typically developing controls. All three analyses revealed that the WS group had higher FA in the right SLF when compared to both control groups. FA in the right SLF of 20 WS subjects was found to be negatively correlated with measures of visuospatial construction abilities. In addition, the voxel-wise analysis revealed increased FA in the WS group in bilateral regions containing the posterior limb of the internal capsules, cortico-pontine tracts, cotrico-spinal tracts, and/or superior thalamic radiations. Increased FA was found in right superior fronto-occipital tract, bilateral SLF (right more than left), bilateral regions containing the uncinate fasciculus, external capsule, and inferior fronto-occipital tracts, bilateral regions containing the inferior longitudinal fasciculi and the inferior fronto-occipital fasciculi, and bilateral forceps major.

Review of inter-subject data analysis methods

In medical imaging, the two most commonly used data analysis methods for investigating differences between populations are region of interest (ROI) analysis and voxel-based analysis (VBA). These methods have been used in a wide variety of applications, including DTI. Although these methods are popular, they are not without their limitations and often do not make full use of information provided in the diffusion tensor. In an effort to take advantage of the structural information inherent in DTI data, tract-based methods of analyzing diffusion parameters along WM tracts isolated by fiber tracking have been proposed [104, 105]. The merits and limitations of each of these three analysis techniques are described below.

Region of interest analysis

ROI analysis is a hypothesis-driven method. *A priori* knowledge of the location and extent of the affected tissue is used to guide the selection of the voxels within the image which represent

this tissue. Then the image intensity or scalar parameters derived from the images at those voxel locations are compared across subjects. While this method is straightforward and does not require any form of image normalization or registration, it is not without its limitations.

First, this method is extremely time consuming and is susceptible to intra- and inter-rater error. Each ROI in each data set must be defined manually, and inter-subject variability in anatomy makes identifying exactly the same location within the same structure across many different subjects extremely difficult. Reliability scores for raters can be calculated, but are not always reported in the literature.

Second, the size and shape of the ROI can affect results. Large ROIs are less sensitive to noise and image artifacts. However, they may introduce partial volume averaging if they include voxels not in the structure of interest. ROIs that do not fit the exact shape of the structure of interest may also introduce partial volume averaging effects. Also, the importance of knowledge of the extent of the disease within the tract should not be overlooked when defining ROIs. If it is the entire structure that is involved, a two-dimensional ROI defined in only one image plane that contains a small portion of the structure could result in a decrease in statistical power when comparing groups. On the other hand, if a three-dimensional ROI is defined to cover the entire structure when only a specific portion of the structure is involved, partial volume averaging may mask significant differences.

Another limitation is that the inconsistency of ROI placement across studies makes it difficult to compare results. For example, DTI studies of schizophrenia that have used ROI analysis placed their ROIs in a variety of locations, including the hippocampus [45, 46], the corpus callosum [47-49], the uncinate fasciculus [50], the cingulum [48, 51, 52], the cerebellar peduncles [53, 54], and various other WM regions in the frontal, temporal, parietal, and occipital lobes [48, 55-57]. There was even variability within studies that examined the same structure. For example, in the three studies that placed ROIs specifically within the cingulum, each used a different size ROI defined in a different location. The first study segmented the cingulum bundles from the 8 coronal slices which also contained the body of the corpus callosum and found decreased FA in both bundles in schizophrenics [51]. Another study placed ROIs of 49 pixels (172 mm^2) only in the anterior cingulum

and found decreased FA values in schizophrenics [48]. The third study used ROIs of 42 pixels in size (148 mm^2) placed in the anterior and posterior cingulum located in the three transverse slices just inferior to the slices containing the medial portion of the cingulum. This study reported decreased FA in the anterior portion but not the posterior portion of the cingulum [52].

Voxel-based analysis

VB analysis is the statistical comparison of two data sets on a voxel-by-voxel basis. In order to accomplish this, each data set must all be aligned (or co-registered) so that the same structures appear in the same image locations across all subjects. This method has several advantages over ROI analysis: no prior knowledge of the location or extent of the diseased tissue is necessary and user interaction is minimized making it less time-consuming and reducing rater bias. Unfortunately, this method has its limitations, as well. The assumption is often made that the image registration results are ideal and each image is aligned perfectly to the other. However, inter-subject variability in anatomy and limitations in current image registration software prevent this from being the case. Also, image normalization is generally performed on scalar images with registration algorithms that attempt to minimize (or maximize) a cost function, which quantifies how well the images are matched. While cost functions, such as mutual information, may perform extremely well and result in excellent matching of scalar images, they are based upon intensity alone and cannot determine whether smaller tracts within a large WM bundle are aligned properly. For example, the uncinate fasciculus and the inferior fronto-occipital fasciculus pass through the external capsule together. The top row of Fig. 2.5 shows an example of a point in the left external capsule, where the uncinate and inferior fronto-occipital (IFO) tracts travel together. If registration results based upon scalar FA images appear to be perfect, there is still no way to know what proportion of the WM bundle in this region is occupied by the unciate and what proportion is occupied by the IFO. Images E and F in Fig. 2.5 demonstrate the case where a single point in the common image space may actually refer to different WM tracts in different subjects, yet the VBA assumes that because the FA maps are aligned well, parameters from the same tracts are being compared in the analysis.

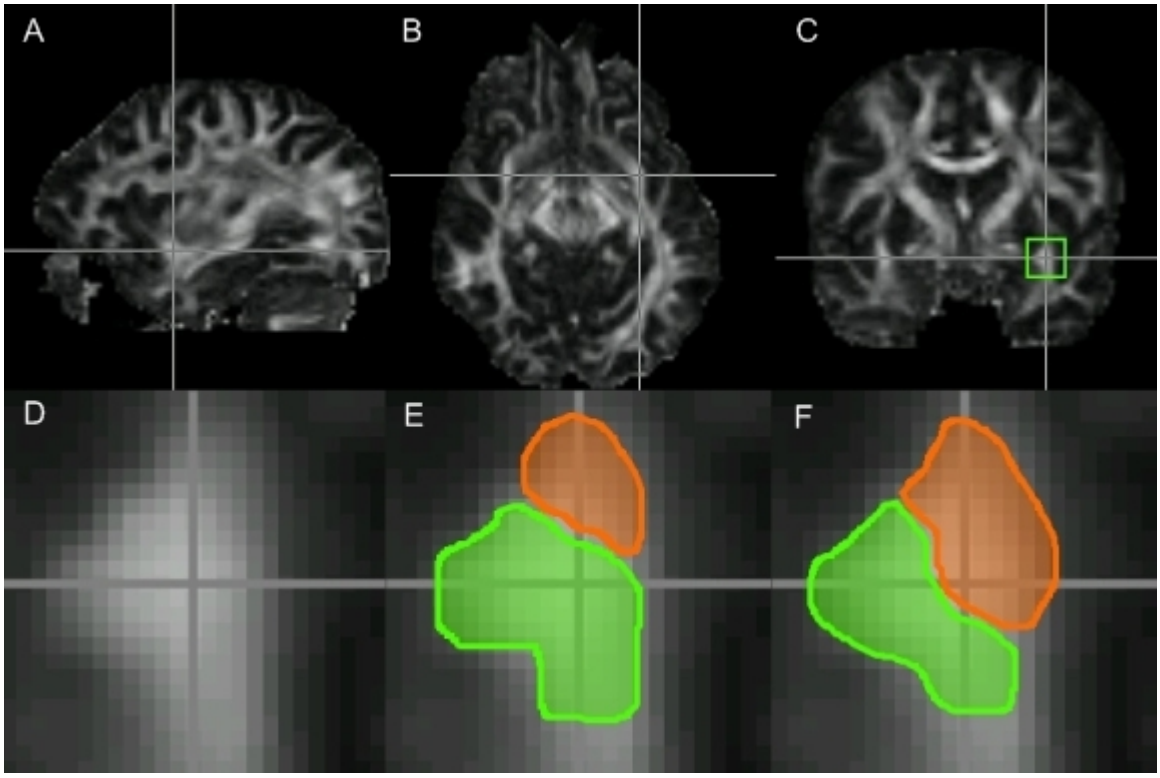

Figure 2.5: Example of the limitations of VBA. The relative proportions of space that the inferior longitudinal fasciculus (orange) and the uncinate fasciculus (green) occupy within the external capsule may vary between subjects(E and F), resulting in comparison of different tracts at the point marked by the crosshairs in a VBA style analysis.

Another problem with VBA is that the registered data are often smoothed in order to minimize this inter-subject variability and increase the signal to noise ratio. However, the size of the smoothing kernels used can introduce bias into the results. Jones *et al.* [106] investigated the effect of kernel size and found that it makes a significant difference in results, suggesting that *a priori* knowledge of the size of the affected area is still important in VB methods and that the results of different VB studies must be compared with caution.

Tract-based analysis

As the field of DTI has developed, the limitations of traditional analysis methods have become more apparent and there has been increasing interest in taking advantage of fiber tracking to improve specificity and sensitivity in DTI analysis. With a few exceptions, analysis methods that utilize fiber tracking generally fall into one of two categories: tract-based analysis and tract-based ROI analysis.

Fillard *et al.* [105] and Mori *et al.* [104] first introduced the concept of tract-based analysis: the statistical comparison of diffusion parameters at corresponding locations along specific WM tracts isolated by fiber tracking. This method is appealing because it should ideally minimize the error in location compared to ROI studies, yet allow for statistical analysis of points along the entire tract, similar to VBA methods. However, a major challenge in utilizing this method is determining correspondence between points along fiber tracts in different subjects.

The first studies to implement tract-based analysis methods studied a single tract-of-interest and used means of defining point correspondence across subjects that were specific to that tract [107–110]. Unfortunately, these methods relied on specific anatomical reference points and could not be easily translated to other WM pathways. Another drawback to these methods was that they still required manual definition of seed points for tracking in each subject.

In an attempt to incorporate tracking information without having to deal with the definition of point correspondence across subjects, tract-based ROI methods have become increasingly popular. In this method, fiber tracking is used to identify the segment specific WM tracts-of-interest, then the tracking results are treated as a single large ROI. One of the first studies to implement this type of analysis method was published by Jones *et al.* [51]. While this method is relatively easy to implement, just as a typical ROI analysis is, many studies still rely upon manual selection of seed points in each data set, which is time consuming and susceptible to user-introduced error. Another problem is that it is unclear whehter the diffusion parameters should be averaged over the entire length of the tractography results or not. The accuracy of fiber tracking results decreases as the distance from the seed points increases, and regions near the ends of the fibers typically have low

FA. Also, it is known that diffusion parameters, particularly FA, often vary along the length of a WM tract as its structure and relationship with other tracts varies. (For example, see [104, 107, 109].) Averaging the parameters over such a large region reduces the sensitivity to localized changes within the tract.

An additional analysis method that has become popular since its introduction is referred to as tract-based spatial statistics (TBSS) [111]. This method attempts to minimize the effects of poor registration while keeping a voxel-wise analysis. The name is misleading, as no fiber tracking is involved. Images are normalized and the FA is skeletonized to define the centers of the major WM bundles in the image. These WM skeletons are mapped onto a template and a voxel-wise analysis is performed within the skeletons only. This method provides a global comparison with no *a priori* knowledge of the locations of the differences necessary. However, with the exception of the core of the corpus callosum, there is generally more than one pathway passing through a given region of WM, and there is no way to distinguish which tract may be causing any detected differences.

A new approach to TBA is presented in Chapter 4. This method is designed to avoid key limitations in the previous techniques. It is evaluated in studies of WM changes in schizophrenia and Williams syndrome described in Chapters 4 and 5.

References

[1] Basser, P. J. and Pierpaoli, C. Microstructural and physiological features of tissues elucidated by quantitative-diffusion-tensor MRI. *Journal of Magnetic Resonance. Series B*, 111(3):209–19, June 1996.

[2] Hahn, E. L. Spin Echoes. *Physical Review*, 80(4):580, 1950.

[3] Carr, H. Y. and Purcell, E. M. Effects of Diffusion on Free Precession in Nuclear Magnetic Resonance Experiments. *Physical Review*, 94(3):630, 1954.

[4] Stejskal, E. O. and Tanner, J. E. Spin Diffusion Measurements - Spin Echoes in Presence of a Time-Dependent Field Gradient. *Journal of Chemical Physics*, 42(1):288–&, 1965.

[5] Bihan, D. L. et al. MR imaging of intravoxel incoherent motions: application to diffusion and perfusion in neurologic disorders. *Radiology*, 161(2):401–7, November 1986.

[6] Basser, P. J., Mattiello, J., and LeBihan, D. Estimation of the effective self-diffusion tensor from the NMR spin echo. *Journal of Magnetic Resonance. Series B.*, 103(3):247–54, 1994.

[7] Song, S. K. et al. Dysmyelination revealed through MRI as increased radial (but unchanged axial) diffusion of water. *Neuroimage*, 17(3):1429–1436, 2002.

[8] Song, S. K. et al. Demyelination increases radial diffusivity in corpus callosum of mouse brain. *Neuroimage*, 26(1):132–40, 2005.

[9] Sun, S. et al. Noninvasive detection of cuprizone induced axonal damage and demyelination in the mouse corpus callosum. *Magnetic Resonance in Medicine*, 55(2):302–8, February 2006.

[10] Song, S. K. et al. Diffusion tensor imaging detects and differentiates axon and myelin degeneration in mouse optic nerve after retinal ischemia. *Neuroimage*, 20(3):1714–1722, 2003.

[11] Schwartz, R. B., Mulkern, R. V., Gudbjartsson, H., and Jolesz, F. Diffusion-weighted MR imaging in hypertensive encephalopathy: clues to pathogenesis. *American Journal of Neuroradiology*, 19(5):859–62, May 1998.

[12] Yang, Q. et al. Serial study of apparent diffusion coefficient and anisotropy in patients with acute stroke. *Stroke*, 30(11):2382–90, November 1999.

[13] Mukherjee, P. and McKinstry, R. C. Reversible posterior leukoencephalopathy syndrome: evaluation with diffusion-tensor MR imaging. *Radiology*, 219(3):756–65, June 2001.

[14] Conturo, T. E. et al. Tracking neuronal fiber pathways in the living human brain. *Proceedings of the National Academy of Sciences of the United States of America*, 96(18):10422–7, 1999.

[15] Mori, S., Crain, B. J., Chacko, V. P., and van Zijl, P. C. Three-dimensional tracking of axonal projections in the brain by magnetic resonance imaging. *Annals of Neurology*, 45(2):265–9, 1999.

[16] Behrens, T. et al. Characterization and propagation of uncertainty in diffusion-weighted MR imaging. *Magnetic Resonance in Medicine*, 50(5):1077–1088, 2003.

[17] Parker, G. J., Haroon, H. A., and Wheeler-Kingshott, C. A. A framework for a streamline-based probabilistic index of connectivity (PICo) using a structural interpretation of MRI diffusion measurements. *Journal of Magnetic Resonance Imaging*, 18(2):242–254, 2003.

[18] Lazar, M. and Alexander, A. L. Bootstrap white matter tractography (BOOT-TRAC). *Neuroimage*, 24(2):524–32, 2005.

[19] Baratti, C., Barnett, A. S., and Pierpaoli, C. Comparative MR Imaging Study of Brain Maturation in Kittens with T1, T2, and the Trace of the Diffusion Tensor. *Radiology*, 210(1):133–142, 1999.

[20] Pfefferbaum, A. et al. Age-related decline in brain white matter anisotropy measured with spatially corrected echo-planar diffusion tensor imaging. *Magnetic Resonance in Medicine*, 44(2):259–68, 2000.

[21] Werring, D. J., Clark, C. A., Barker, G. J., Thompson, A. J., and Miller, D. H. Diffusion tensor imaging of lesions and normal-appearing white matter in multiple sclerosis. *Neurology*, 52(8):1626, May 1999.

[22] Guo, A. C., Petrella, J. R., Kurtzberg, J., and Provenzale, J. M. Evaluation of White Matter Anisotropy in Krabbe Disease with Diffusion Tensor MR Imaging: Initial Experience. *Radiology*, 218(3):809–815, March 2001.

[23] NIMH. Schizophrenia. (NIH Report Number 3517), 1999.

[24] Kraepelin, E. *Demetia Praecox and Paraphrenia*. R. E. Krieger Pub. Co., 1971, Huntington, NY, 1919.

[25] Suddath, R. L., Christison, G. W., Torrey, E. F., Casanova, M. F., and Weinberger, D. R. Anatomical abnormalities in the brains of monozygotic twins discordant for schizophrenia. *N Engl J Med*, 322(12):789–94, 1990.

[26] Wible, C. G. et al. Prefrontal cortex and schizophrenia. A quantitative magnetic resonance imaging study. *Archives of General Psychiatry*, 52(4):279–88, 1995.

[27] Breier, A. et al. Brain morphology and schizophrenia. A magnetic resonance imaging study of limbic, prefrontal cortex, and caudate structures. *Archives of General Psychiatry*, 49(12):921–6, 1992.

[28] Buchanan, R. W., Vladar, K., Barta, P. E., and Pearlson, G. D. Structural evaluation of the prefrontal cortex in schizophrenia. *The American Journal of Psychiatry*, 155(8):1049–55, 1998.

[29] Sigmundsson, T. et al. Structural abnormalities in frontal, temporal, and limbic regions and interconnecting white matter tracts in schizophrenic patients with prominent negative symptoms. *The American Journal of Psychiatry*, 158(2):234–43, 2001.

[30] Cannon, T. D. et al. Regional gray matter, white matter, and cerebrospinal fluid distributions in schizophrenic patients, their siblings, and controls. *Archives of General Psychiatry*, 55(12):1084–91, 1998.

[31] Wright, I. C. et al. Meta-analysis of regional brain volumes in schizophrenia. *The American Journal of Psychiatry*, 157(1):16–25, 2000.

[32] Friston, K. J. and Frith, C. D. Schizophrenia: a disconnection syndrome? *Clinical Neuroscience*, 3(2):89–97, 1995.

[33] Andreasen, N. C., Paradiso, S., and O'Leary, D. S. "Cognitive dysmetria" as an integrative theory of schizophrenia: a dysfunction in cortical-subcortical-cerebellar circuitry? *Schizophrenia Bulletin*, 24(2):203–18, 1998.

[34] Akbarian, S. et al. Maldistribution of interstitial neurons in prefrontal white matter of the brains of schizophrenic patients. *Archives of General Psychiatry*, 53(5):425–36, May 1996.

[35] Rajkowska, G., Selemon, L. D., and Goldman-Rakic, P. S. Neuronal and glial somal size in the prefrontal cortex: a postmortem morphometric study of schizophrenia and Huntington disease. *Archives of General Psychiatry*, 55(3):215–24, 1998.

[36] Roberts, R. C., Conley, R., Kung, L., Peretti, F. J., and Chute, D. J. Reduced striatal spine size in schizophrenia: a postmortem ultrastructural study. *Neuroreport*, 7(6):1214–8, 1996.

[37] Glantz, L. A. and Lewis, D. A. Decreased dendritic spine density on prefrontal cortical pyramidal neurons in schizophrenia. *Archives of General Psychiatry*, 57(1):65–73, 2000.

[38] Selemon, L. D., Rajkowska, G., and Goldman-Rakic, P. S. Elevated neuronal density in prefrontal area 46 in brains from schizophrenic patients: application of a three-dimensional, stereologic counting method. *J Comp Neurol*, 392(3):402–12, 1998.

[39] Selemon, L. D. Increased cortical neuronal density in schizophrenia. *The American Journal of Psychiatry*, 161(9):1564, 2004.

[40] Hof, P. R., Haroutunian, V., Copland, C., Davis, K. L., and Buxbaum, J. D. Molecular and cellular evidence for an oligodendrocyte abnormality in schizophrenia. *Neurochemical Research*, 27(10):1193–200, 2002.

[41] Hakak, Y. et al. Genome-wide expression analysis reveals dysregulation of myelination-related genes in chronic schizophrenia. *Proceedings of the National Academy of Sciences of the United States of America*, 98(8):4746–51, 2001.

[42] Flynn, S. W. et al. Abnormalities of myelination in schizophrenia detected in vivo with MRI, and post-mortem with analysis of oligodendrocyte proteins. *Molecular Psychiatry*, 8(9):811–20, 2003.

[43] Bartzokis, G. et al. Dysregulated brain development in adult men with schizophrenia: a magnetic resonance imaging study. *Biological Psychiatry*, 53(5):412–21, 2003.

[44] Jones, D. K. The effect of gradient sampling schemes on measures derived from diffusion tensor MRI: a Monte Carlo study. *Magnetic Resonance in Medicine*, 51(4):807–15, April 2004.

[45] Rose, S. E. et al. Evidence of altered prefrontal-thalamic circuitry in schizophrenia: An optimized diffusion MRI study. *NeuroImage*, 32(1):16–22, 2006.

[46] Sun, Z. et al. Abnormal anterior cingulum in patients with schizophrenia: a diffusion tensor imaging study. *Neuroreport*, 14(14):1833–6, October 2003.

[47] Wang, F. et al. Anterior cingulum abnormalities in male patients with schizophrenia determined through diffusion tensor imaging. *The American Journal of Psychiatry*, 161(3):573–5, 2004.

[48] Seok, J. et al. White matter abnormalities associated with auditory hallucinations in schizophrenia: A combined study of voxel-based analyses of diffusion tensor imaging and structural magnetic resonance imaging. *Psychiatry Research: Neuroimaging*, 156(2):93–104, 2007.

[49] Kumra, S. et al. White matter abnormalities in early-onset schizophrenia: a voxel-based diffusion tensor imaging study. *Journal of the American Academy of Child and Adolescent Psychiatry*, 44(9):934–41, September 2005.

[50] Agartz, I., Andersson, J. L., and Skare, S. Abnormal brain white matter in schizophrenia: a diffusion tensor imaging study. *Neuroreport*, 12(10):2251–4, 2001.

[51] Jones, D. K. et al. Age effects on diffusion tensor magnetic resonance imaging tractography measures of frontal cortex connections in schizophrenia. *Human Brain Mapping*, 27(3):230–8, March 2006.

[52] Douaud, G. et al. Anatomically related grey and white matter abnormalities in adolescent-onset schizophrenia. *Brain*, 130(9):2375–2386, 2007.

[53] Kyriakopoulos, M., Vyas, N. S., Barker, G. J., Chitnis, X. A., and Frangou, S. A Diffusion Tensor Imaging Study of White Matter in Early-Onset Schizophrenia. *Biological Psychiatry*, In Press, Corrected Proof, 2007.

[54] Shergill, S. S. et al. A Diffusion Tensor Imaging Study of Fasciculi in Schizophrenia. *The American Journal of Psychiatry*, 164(3):467–473, 2007.

[55] Szeszko, P. R. et al. Clinical and Neuropsychological Correlates of White Matter Abnormalities in Recent Onset Schizophrenia. *Neuropsychopharmacology*, 2007.

[56] Hubl, D. et al. Pathways that make voices: white matter changes in auditory hallucinations. *Archives of General Psychiatry*, 61(7):658–68, July 2004.

[57] Seal, M. L. et al. Abnormal white matter microstructure in schizophrenia: a voxelwise analysis of axial and radial diffusivity. *Schizophrenia Research*, 101(1-3):106–10, April 2008.

[58] Cheung, V. et al. A diffusion tensor imaging study of structural dysconnectivity in never-medicated, first-episode schizophrenia. *Psychological Medicine*, 38(6):877–85, June 2008.

[59] McIntosh, A. M. et al. White Matter Tractography in Bipolar Disorder and Schizophrenia. *Biological Psychiatry*, September 2008.

[60] Price, G. et al. White matter tracts in first-episode psychosis: A DTI tractography study of the uncinate fasciculus. *NeuroImage*, In Press, Corrected Proof, 2007.

[61] Kanaan, R. A. et al. Tract-specific anisotropy measurements in diffusion tensor imaging. *Psychiatry Research*, 146(1):73–82, 2006.

[62] Price, G. et al. Abnormal brain connectivity in first-episode psychosis: A diffusion MRI tractography study of the corpus callosum. *NeuroImage*, 35(2):458–466, 2007.

[63] Peoples, R. et al. A physical map, including a BAC/PAC clone contig, of the Williams-Beuren syndrome–deletion region at 7q11.23. *American Journal of Human Genetics*, 66(1):47–68, 2000.

[64] Beuren, A. J., Apitz, J., and Harmjanz, D. Supravalvular aortic stenosis in association with mental retardation and a certain facial appearance. *Circulation*, 26:1235–40, December 1962.

[65] Williams, J. C., Barratt-Boyes, B. G., and Lowe, J. B. Supravalvular aortic stenosis. *Circulation*, 24:1311–8, December 1961.

[66] Mervis, C. B. et al. The Williams syndrome cognitive profile. *Brain and Cognition*, 44(3):604–28, December 2000.

[67] Bellugi, U., Adolphs, R., Cassady, C., and Chiles, M. Towards the neural basis for hypersociability in a genetic syndrome. *Neuroreport*, 10(8):1653–7, June 1999.

[68] Klein-Tasman, B. P. and Mervis, C. B. Distinctive personality characteristics of 8-, 9-, and 10-year-olds with Williams syndrome. *Developmental Neuropsychology*, 23(1-2):269–90, 2003.

[69] Dykens, E. M. Anxiety, fears, and phobias in persons with Williams syndrome. *Developmental Neuropsychology*, 23(1-2):291–316, 2003.

[70] Klein, A. J., Armstrong, B. L., Greer, M. K., and Brown, F. R. Hyperacusis and otitis media in individuals with Williams syndrome. *The Journal of Speech and Hearing Disorders*, 55(2):339–44, May 1990.

[71] Aizawa, H. et al. Phosphorylation of cofilin by LIM-kinase is necessary for semaphorin 3A-induced growth cone collapse. *Nature Neuroscience*, 4(4):367–373, April 2001.

[72] Endo, M. et al. Control of Growth Cone Motility and Morphology by LIM Kinase and Slingshot via Phosphorylation and Dephosphorylation of Cofilin. *J. Neurosci.*, 23(7):2527–2537, April 2003.

[73] Meng, Y. et al. Abnormal spine morphology and enhanced LTP in LIMK-1 knockout mice. *Neuron*, 35(1):121–33, July 2002.

[74] Hoogenraad, C. C. et al. The murine CYLN2 gene: genomic organization, chromosome localization, and comparison to the human gene that is located within the 7q11.23 Williams syndrome critical region. *Genomics*, 53(3):348–58, November 1998.

[75] Zeeuw, C. I. D. et al. CLIP-115, a novel brain-specific cytoplasmic linker protein, mediates the localization of dendritic lamellar bodies. *Neuron*, 19(6):1187–99, December 1997.

[76] Hoogenraad, C. C. et al. Targeted mutation of Cyln2 in the Williams syndrome critical region links CLIP-115 haploinsufficiency to neurodevelopmental abnormalities in mice. *Nature Genetics*, 32(1):116–27, September 2002.

[77] Karasawa, T., Yokokura, H., Kitajewski, J., and Lombroso, P. J. Frizzled-9 Is Activated by Wnt-2 and Functions in Wnt/beta -Catenin Signaling. *Journal of Biological Chemistry*, 277(40):37479–37486, September 2002.

[78] Muroyama, Y., Fujihara, M., Ikeya, M., Kondoh, H., and Takada, S. Wnt signaling plays an essential role in neuronal specification of the dorsal spinal cord. *Genes and Development*, 16(5):548–553, March 2002.

[79] Zhao, C. et al. Hippocampal and visuospatial learning defects in mice with a deletion of frizzled 9, a gene in the Williams syndrome deletion interval. *Development (Cambridge, England)*, 132(12):2917–27, June 2005.

[80] de Zhang, R., Maksymowych, A. B., and Simpson, L. L. Cloning and sequence analysis of a cDNA encoding human syntaxin 1A, a polypeptide essential for exocytosis. *Gene*, 159(2):293–294, 1995.

[81] Igaz, L. M., Bekinschtein, P., Izquierdo, I., and Medina, J. H. One-trial aversive learning induces late changes in hippocampal CaMKII[alpha], Homer 1a, Syntaxin 1a and ERK2 protein levels. *Molecular Brain Research*, 132(1):1–12, December 2004.

[82] Reiss, A. L. et al. An experiment of nature: brain anatomy parallels cognition and behavior in Williams syndrome. *The Journal of Neuroscience*, 24(21):5009–15, May 2004.

[83] Meyer-Lindenberg, A. et al. Neural basis of genetically determined visuospatial construction deficit in Williams syndrome. *Neuron*, 43(5):623–31, September 2004.

[84] Eckert, M. A. et al. Evidence for superior parietal impairment in Williams syndrome. *Neurology*, 64(1):152–3, 2005.

[85] Meyer-Lindenberg, A., Mervis, C. B., and Berman, K. F. Neural mechanisms in Williams syndrome: a unique window to genetic influences on cognition and behaviour. *Nature Reviews. Neuroscience*, 7(5):380–93, May 2006.

[86] Thompson, P. M. et al. Abnormal cortical complexity and thickness profiles mapped in Williams syndrome. *The Journal of Neuroscience*, 25(16):4146–58, April 2005.

[87] Schmitt, J. E. et al. Increased gyrification in Williams syndrome: evidence using 3D MRI methods. *Developmental Medicine and Child Neurology*, 44(5):292–5, May 2002.

[88] Gaser, C. et al. Increased local gyrification mapped in Williams syndrome. *NeuroImage*, 33(1):46–54, October 2006.

[89] Kippenhan, J. S. et al. Genetic contributions to human gyrification: sulcal morphometry in Williams syndrome. *The Journal of Neuroscience*, 25(34):7840–6, August 2005.

[90] Essen, D. C. V. et al. Symmetry of cortical folding abnormalities in Williams syndrome revealed by surface-based analyses. *The Journal of Neuroscience*, 26(20):5470–83, May 2006.

[91] Galaburda, A. M. et al. Dorsal forebrain anomaly in Williams syndrome. *Archives of Neurology*, 58(11):1865–9, November 2001.

[92] Jackowski, A. P. and Schultz, R. T. Foreshortened dorsal extension of the central sulcus in Williams syndrome. *Cortex*, 41(3):282–90, June 2005.

[93] Jackowski, A. P. et al. Brain abnormalities in Williams syndrome: A review of structural and functional magnetic resonance imaging findings. *European Journal of Paediatric Neurology: EJPN: Official Journal of the European Paediatric Neurology Society*, August 2008.

[94] Mobbs, D. et al. Anomalous brain activation during face and gaze processing in Williams syndrome. *Neurology*, 62(11):2070–6, June 2004.

[95] Sarpal, D. et al. A genetic model for understanding higher order visual processing: functional interactions of the ventral visual stream in williams syndrome. *Cerebral Cortex*, 18(10):2402–9, October 2008.

[96] Landau, B., Hoffman, J. E., and Kurz, N. Object recognition with severe spatial deficits in Williams syndrome: sparing and breakdown. *Cognition*, 100(3):483–510, July 2006.

[97] Mobbs, D. et al. Frontostriatal dysfunction during response inhibition in Williams syndrome. *Biological Psychiatry*, 62(3):256–61, August 2007.

[98] Meyer-Lindenberg, A. et al. Neural correlates of genetically abnormal social cognition in Williams syndrome. *Nature Neuroscience*, 8(8):991–993, 2005.

[99] Meyer-Lindenberg, A. et al. Functional, structural, and metabolic abnormalities of the hippocampal formation in Williams syndrome. *The Journal of Clinical Investigation*, 115(7):1888–95, July 2005.

[100] Marenco, S. et al. Genetic contributions to white matter architecture revealed by diffusion tensor imaging in Williams syndrome. *Proceedings of the National Academy of Sciences of the United States of America*, 104(38):15117–22, September 2007.

[101] Pierpaoli, C. and Basser, P. J. Toward a quantitative assessment of diffusion anisotropy. *Magnetic Resonance in Medicine*, 36(6):893–906, 1996.

[102] Conturo, T. E., McKinstry, R. C., Akbudak, E., and Robinson, B. H. Encoding of anisotropic diffusion with tetrahedral gradients: a general mathematical diffusion formalism and experimental results. *Magnetic Resonance in Medicine: Official Journal of the Society of Magnetic Resonance in Medicine / Society of Magnetic Resonance in Medicine*, 35(3):399–412, March 1996.

[103] Hoeft, F. et al. More is not always better: increased fractional anisotropy of superior longitudinal fasciculus associated with poor visuospatial abilities in Williams syndrome. *The Journal of Neuroscience*, 27(44):11960–5, October 2007.

[104] Mori, S. et al. Imaging cortical association tracts in the human brain using diffusion-tensor-based axonal tracking. *Magnetic Resonance in Medicine*, 47(2):215–23, 2002.

[105] Fillard, P., Gilmore, J., Piven, J., Lin, W., and Gerig, G. *Quantitative Analysis of White Matter Fiber Properties along Geodesic Paths*. Medical Image Computing and Computer-Assisted Intervention. 2003.

[106] Jones, D. K., Symms, M. R., Cercignani, M., and Howard, R. J. The effect of filter size on VBM analyses of DT-MRI data. *Neuroimage*, 26(2):546–54, 2005.

[107] Gong, G. et al. Asymmetry analysis of cingulum based on scale-invariant parameterization by diffusion tensor imaging. *Human Brain Mapping*, 24(2):92–8, 2005.

[108] Gong, G. et al. Side and handedness effects on the cingulum from diffusion tensor imaging. *Neuroreport*, 16(15):1701–5, 2005.

[109] Partridge, S. C. et al. Tractography-based quantitation of diffusion tensor imaging parameters in white matter tracts of preterm newborns. *Journal of Magnetic Resonance Imaging*, 22(4):467–74, 2005.

[110] Xie, S. et al. Evaluation of bilateral cingulum with tractography in patients with Alzheimer's disease. *Neuroreport*, 16(12):1275–8, 2005.

[111] Smith, S. M. et al. Tract-based spatial statistics: voxelwise analysis of multi-subject diffusion data. *Neuroimage*, 31(4):1487–505, 2006.

CHAPTER III

ALTERED DIFFUSION PROPERTIES IN WHITE MATTER IN WILLIAMS SYNDROME

Introduction

Williams syndrome (WS) is a disorder caused by a 1.5Mb hemizygous deletion on chromosome 7 (7q11.23) [1]. This deletion results in a unique set of characteristic physical, cognitive, and behavioral symptoms. Characteristic physical traits include unique facial features, such as a wide mouth with full lips and protrusive ears [2] and cardiovascular abnormalities [2, 3]. Individuals with WS typically exhibit mild mental retardation along with a unique combination of relative cognitive strengths and weaknesses, such as excellent verbal short-term memory and poor visuospatial construction [4]. These individuals also typically demonstrate excessive friendliness and empathy [5, 6], non-social anxiety [7], and sensitivity to loud noises [8].

The diversity of symptoms exhibited in this syndrome suggests that multiple functional networks within the brain may be affected in different ways. This, along with evidence that several genes included in the typical WS deletion are involved in normal neural development and function [9–13] has led to increasing interest in studying the neural mechanisms involved in the disorder. Magnetic resonance imaging (MRI) studies have revealed structural abnormalities, such as increased gyrification [14–16], reduced sulcal depth in the intraparietal and orbitofrontal sulci [17, 18], and a reduction in the extent of the central sulcus [19, 20]. Functional MRI (fMRI) studies have revealed differences in neural activation during tasks involving response inhibition [21], processing of fearful stimuli [22], and visuospatial construction [23, 24] in WS subjects compared to normal controls. Recently, diffusion tensor imaging (DTI) has been used to investigate white matter (WM) involvement in WS [25, 26], revealing not only regions of reduced anisotropy, but also regions of increased anisotropy. These studies used region of interest analysis methods [25, 26] and tract-based spatial statistics (TBSS) [25]. In the study described here, differences in fractional anisotropy (FA) were examined with a voxel-based comparison of young adults with WS and normal young adults.

Methods

Subjects

Williams syndrome subjects were recruited from the annual music camp for young adults with Williams syndrome and other developmental disorders hosted by the Vanderbilt Kennedy Center for Research on Human Development, the Blair School of Music, and the National Williams Syndrome Association. Normal controls (NC) were recruited from the general population. Functional, structural, and diffusion tensor imaging scans were acquired for each subject during a single imaging session. Informed consent was obtained from each subject according to the requirements of the Institutional Review Board. DTI data sets from a total of 16 WS subjects and 16 normal controls were compared. Structural images from an additional NC who did not have DTI data were used as the initial target for creation of a study-specific template used in the image co-registration process. The WS group consisted of 6 females and 10 males; all but 3 subjects were right handed; and their mean age was 24 years (range = 16 to 33 years). The NC group consisted of 8 females and 8 males; 12 NCs were right-handed, 3 were left-handed and one was ambidextrous; and their mean age was 23 years (range = 16 to 32 years). The target subject was a 19 year-old male who was right handed. A summary of the subject demographics is shown in Table 3.1. There was no significant difference in the mean age of the two groups ($p = 0.255$), and handedness was determined by the Edinburgh handedness inventory [27].

Image Acquisition

All images were acquired using a Philips Intera Achieva 3T MRI scanner with high-performance gradient coils (80 mT/m gradient strength and 100 mT/m/ms slew-rate) and an 8 channel SENSE (sensitivity encoding) head coil. Diffusion weighted images (DWIs) were acquired with 32 diffusion-encoding directions (tr(b) = 1000 s/mm^2) and one non-diffusion-weighted image volume (tr(b) = 0 s/mm^2). Single-shot EPI and sensitivity encoding (SENSE) were used to decrease total scan time. The imaging parameters used were TE = 60 ms, TR = 10,000 ms, SENSE factor = 2,

Table 3.1: Subject demographics

Group		N	Age (years)			Handedness		
			Range	Mean	Std. Dev.	Right	Left	Ambidextrous
Controls		16	16 - 32	23	4	12	3	1
	Male	8	18 - 32	23	5	5	2	1
	Female	8	16 - 26	22	4	7	1	0
Williams Syndrome		16	16 - 33	24	6	13	3	0
	Male	10	16 - 33	24	5	7	3	0
	Female	6	16 - 30	24	5	6	0	0

FOV = 256 x 256 mm^2, matrix size of 128 x 128, and 2 mm slice thickness. Whole-brain coverage was obtained with 60 axial slices in 6 minutes. A high-resolution, T1-weighted 3D anatomical volume was acquired using a multi-shot gradient echo sequence with TE = 4.6 ms, TR = 8.9 ms, SENSE factor = 2, FOV = 256 x 256 mm^2, and matrix size of 256 x 256. The volume consisted of 170 sagittal slices with an isotropic voxel size of 1 mm^3, and total scan time was 4 minutes and 24 seconds.

Image Processing

Tensor Calculation

Eddy current distortion and in-plane bulk subject motion were corrected within the original DWIs with the Philips Research Imaging Development Environment (PRIDE) Diffusion Registration tool (release 0.5). This tool performs an affine registration of each DWI to its corresponding non-diffusion-weighted image (b0) [28]. The distortion and motion-corrected DWIs were then used to calculate the diffusion tensor and FA maps, as well as extract the b0 image volume, with a modified version of the PRIDE Fiber Tracking tool (Version 6.0a1). The in-house modifications to the tool

included the addition of a routine to automatically reject from the tensor calculation voxels corrupted by bulk and physiological motion. (See Appendix A for more details.)

Image Registration

Normalization of the FA maps was performed in two major steps. First, a study-specific FA template was created by normalizing each subject's FA map (FA_i) to the target T1-weighted image space ($T1_{targ}$) and then averaging the resulting images (FA_{temp}). Normalization of the FA maps was performed by combining the transformations from an intra-subject registration ($b0_i$ to $T1_i$) and an inter-subject registration ($T1_i$ to $T1_{targ}$) to define the total transformation between the b0 image space of each subject ($b0_i$), which is inherently co-registered to FA_i, and the target T1-weighted image space ($T1_{targ}$). The resulting total transformation for each subject was then applied to FA_i, and the transformed FA maps were averaged to create the template. second, the original FA maps (FA_i) were co-registered directly to the template (FA_{temp}) to reduce potential bias introduced from the selection of a single normal control as the initial target.

All intermediate image registration steps were performed using linear [29, 30] and non-linear [31] registration software provided by the Medical Image Processing Laboratory in the Department of Electrical Engineering and Computer Science. Intra-subject registration steps included a rigid registration to account for subject motion between the diffusion-weighed scan and the T1-weighted scan and a then a nonlinear registration step to reduce the effects of image distortion. Inter-subject registration included a rigid registration with scaling to account for differences in head size and orientation between each subject and the target, as well as a nonlinear registration step to account for anatomical differences.

Voxel-based analysis

The normalized FA maps for the NC and WS groups were compared on a voxel-wise basis with a two-sample t-test. No smoothing was applied to the maps prior to analysis. The resulting significance maps were thresholded at the $p < 0.05$ level and masked so that only voxels with an

average FA value of 0.3 or greater in the FA_{temp} remained. Permutation testing was performed with the same significance level and masking to determine the minimum significant cluster size (in 3 dimensions) according to the methods described by Bullmore *et al.* [32]. Only clusters with a volume greater than 90 voxels (90 mm^3) were considered to be significant ($p < 0.05$). The average FA template and map of significant clusters were transformed to the Talairach space for visualization.

Results

On visual inspection, image normalization appeared to perform well in the larger WM structures, with reliability decreasing for smaller WM tracts and tracts branching off to cortical areas, particularly in the parietal and occipital lobes. Significant differences in FA between the two groups were found in several regions where image normalization performed well. Figure 3.1 shows the overlay of the significance map on the average FA template. The mean FA of the WS subjects compared to NCs was decreased in the splenium of the corpus callosum, bilateral corona radiata, external capsules (EC), cortico-spinal/cortico-cerebellar tracts extending from the pons through the posterior limb of the external capsules (PLIC), uncinate fasciculi (UF)/inferior front-occipital fasciculus (IFO), and superior longitudinal fasciculi (SLF). An increase in mean FA in WS was found in the left IFO/inferior longitudinal fasciculus (ILF), bilateral SLF (right $>$ left), and bilateral UF. (See Table 3.2 for a list of representative Talairach coordinates for these regions.) Note that a given anatomical structure can have positive and negative changes at different positions along the tract. Significant clusters were also found in regions of poor registration: bilateral forceps major, anterior commissure, prefrontal WM, ventral cingulum, fornix, cerebellar peduncles, and WM underlying the intraparietal sulci.

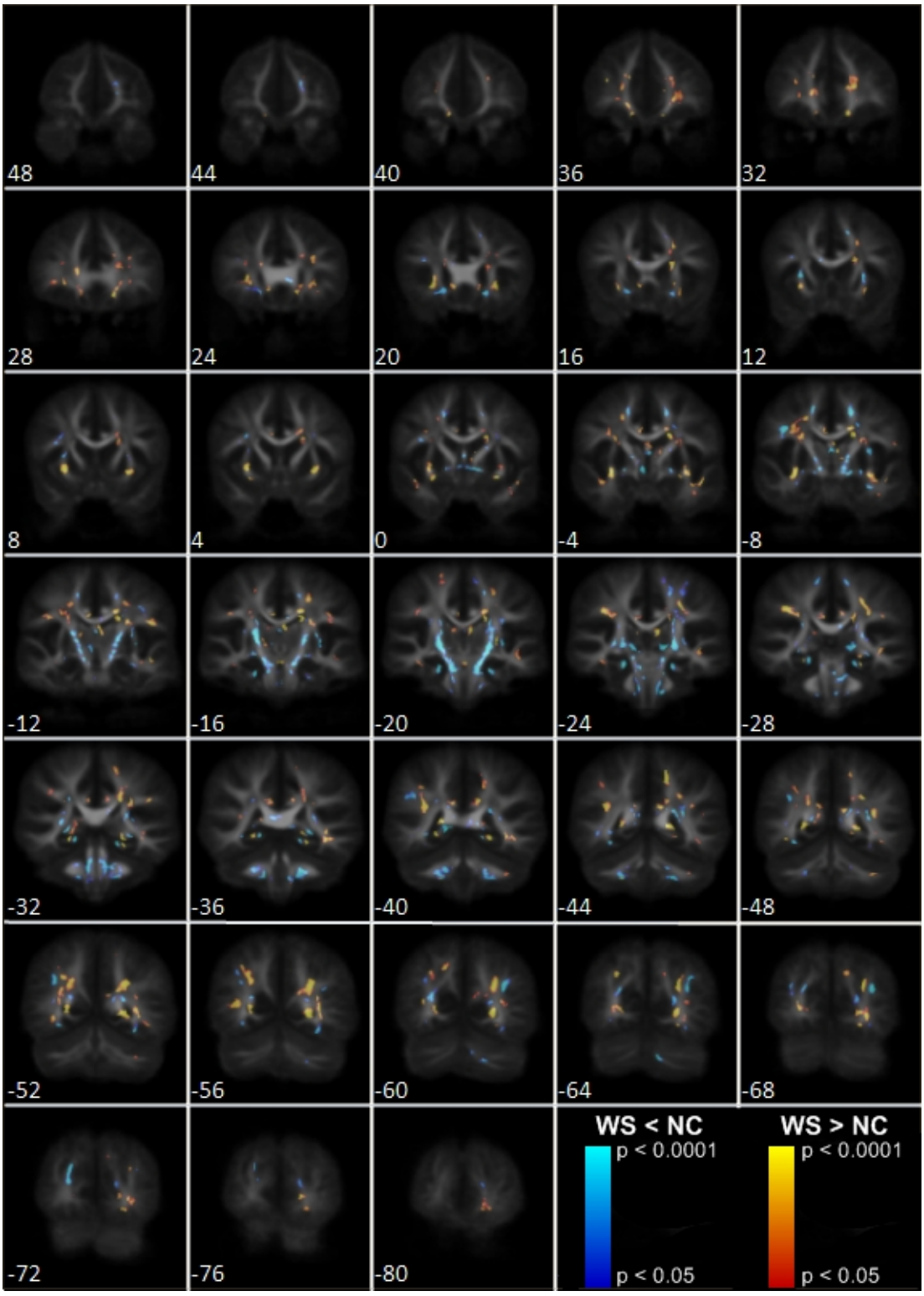

Figure 3.1: Significant differences in FA in WS. Overlay of regions of significantly increased (warm colors) and reduced (cool colors) FA in WS compared to controls on coronal slices of the average FA template in Talairach space. (Images displayed in radiological convention.)

Table 3.2: Voxel-based anaylsis results

WM Region	Talairach Coordinates		
	X	Y	Z
Decreased FA			
Corona radiata (L)	-15	-6	45
Corona radiata (R)	17	-6	44
External capsule (L)	-26	9	8
External capsule (R)	27	9	8
PLIC (L)	-20	-18	5
PLIC (R)	21	-18	5
Splenium	1	-36	12
SLF (L)	-39	-11	31
SLF (R)	41	-8	28
Uncinate/IFO (L)	-17	19	-9
Uncinate/IFO (R)	17	19	-9
Increased FA			
External capsule (L)	-29	5	-5
External capsule (R)	27	8	-3
ILF/IFO (L)	-38	-37	-4
SLF (L)	-42	-30	26
SLF (R)	37	-25	32
SLF (L)	-37	-44	21
SLF (R)	33	-42	21

Discussion

We performed a voxel-based comparison of FA between young adults with Williams syndrome and normal controls and found several regions of WM with increased FA, as well as several regions with decreased FA, in the WS subjects. These results are generally consistent with previously reported differences in WM diffusion parameters between subjects with WS and normal controls [25, 26].

Decreased FA in the splenium of the corpus callosum is consistent with the findings of Hoeft *et al.* [25], as well as reports of altered shape and reduced volume in the posterior portion of the corpus callosum in WS[33–35]. Changes in this portion of the corpus callosum, which contains fibers connecting the right and left parietal and occipital lobes, may be related to the visuospatial

deficits associated with the disorder. It should be noted that if the volume of the splenium was significantly reduced in the WS subjects compared to the normal control used as the initial target in the image registration process, then the observed reduction in FA in that region could be the result of an interpolation artifact introduced during image co-registration and not the result of a change in the diffusion properties of the underlying axons.

Another major WM tract with changes in FA that is potentially involved in visuospatial deficits is the SLF, which contains connections between the frontal, parietal, and temporal lobes. Hoeft *et al.* reported increased FA in both the right and left SLF (right $>$ left) and a negative correlation of FA in the right SLF with scores from the WAIS-III Object Assembly subtest. We also found regions of increased FA in both the left and right SLF, with larger cluster size in the right SLF. We also found small regions of reduced FA in both the left and right SLF, just anterior to the regions of increased FA.

Results in the WM regions containing the ILF and IFO vary between this study and the studies published by Hoeft *et al.* and Marenco *et al.* [26]. We found increased FA in the left ILF/IFO only, Hoeft *et al.* reported significantly increased FA in the right ILF only, and Marenco *et al.* found increased anisotropy in tract-based ROIs averaged over both hemispheres. This region of WM contains fiber pathways associated with face and object recognition, and it has been proposed that while face processing abilities seem to be relatively intact in WS, higher-level object recognition and face processing may actually be functioning abnormally [36, 37].

We found that the bilateral EC also contained regions of both increased and decreased FA, while Hoeft *et al.* reported only increased FA. An additional region of WM in the UF/IFO, slightly anterior to the EC, showed reduced FA in bilaterally. Changes in the EC and frontal WM may potentially be related to the social aspects of the disorder. The UF and IFO, two major association pathways with connections to the frontal lobes, pass through this region, as well as several smaller tracts, which include connections between the frontal lobe and the basal ganglia and amygdala. Functional connections between the cortical regions connected by pathways passing through the EC have been shown to be disrupted in WS. Mobbs *et al.* [21] reported abnormal activity in the striatum,

dorsolateral prefrontal, and dorsal cingulate cortices in an fMRI study of response inhibition, and an fMRI study designed to invoke activation in the amygdala from threatening visual stimuli by Meyer-Lindenberg *et al.* [22] suggested that functional connections between different regions of frontal cortices and the amygdala may be disrupted.

Our finding of decreased FA in the bilateral PLIC is consistent with the Hoeft and Marenco studies, which also reported bilateral reductions of anisotropy in these regions, and the extent of the regions of reduced FA we observed was quite remarkable. Both regions extended from the level of the pons to the level of the superior portion of the thalamus and include several WM pathways important in motor and sensory function, such as the corticobulbar (cranial motor function), corticospinal (motor function in the body), corticorubral (motor coordination), thalamocortical (sensory and motor function), and corticopontine (relay between motor cortex and cerebellum) tracts. While mild motor symptoms have been noted in the literature [38, 39], it has not been until recently that quantitative studies of motor signs and symptoms in WS have been published. Gagliardi *et al.* [40]reported the existence of cerebellar, pyramidal, and extrapyramidal signs that varied in distribution according to age. Hocking *et al.* [41] studied abnormal gait characteristics in adults with WS and suggested that basal ganglia dysfunction and visuomotor deficits may be involved. Quantitative measures of

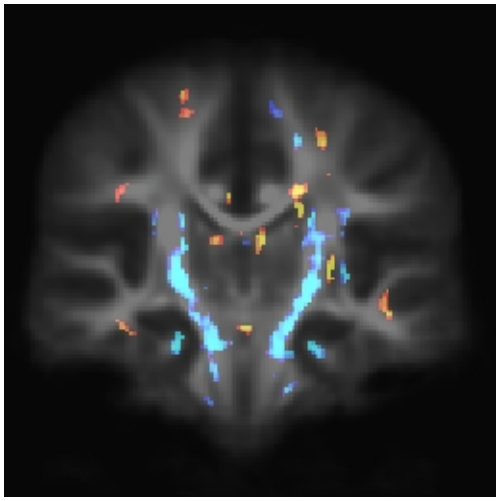

Figure 3.2: Large regions of significantly reduced FA in the bilateral PLIC. (Coronal slice Y $=$ -20 from Figure 3.1.)

neurological signs or symptoms in the WS cohort in this study were not obtained because, prior to the studies by Gagliardi *et al.* and Hocking *et al.*, little attention had been paid to them in clinical studies. However, camp organizers did report the existence of abnormal gait and muscle weakness in several of the WS subjects in this study (T. Thornton-Wells, personal communication, November 14, 2008).

It is difficult to interpret the underlying cause of the differences in FA between the WS and NC groups observed in this study because the diffusion tensor is sensitive to changes in local tissue microstructure, such as cell density, edema, and demyelination, as well as differences in structural organization. Marenco *et al.* hypothesized that changes they found in the principal orientation of WM tissue in several association tracts indicated that WM fibers that normally developed in the right-left orientation either changed course during development or failed to develop. However , as Hoeft *et al.* pointed out, it is also possible that the orientational differences Marenco *et al.* observed and the increases in FA observed in this study and the study by Hoeft *et al.* indicates a decrease in normal branching of these tracts to cortical regions along their paths. Decreased branching might lead to a decrease in the normal amount of fiber crossing, resulting in an increase in FA. This hypothesis is consistent with evidence that the LIMK1 and CYLN2 genes included in the typical WS deletion are involved in normal neuronal migration and development [10, 42, 43]. LIMK1 is required for proper functioning of an axonal guidance protein called *semaphorin 3A* in neural migration [42]. This same protein has also been shown to be involved in normal pruning of axonal branches in hippocampal neurons [44]. In early development, axons send out many branches to different functional areas, which are selectively pruned later in development as the brain refines itself. Perhaps, while some regions experience a decrease in branching causing an increase in FA, other regions may initially develop normal branching that is never properly pruned, causing a decrease in FA.

An additional consideration that should be made in the interpretation of the results reported here is the fact that there were methodological differences between this study and the studies by Hoeft *et al.* and Marenco *et al.*. Both of the previous studies had 10 or fewer subjects per group and acquired multiple sets of 6 diffusion directions. We compared 16 WS subjects with 16 controls

and acquired a single set of 32 diffusion directions, which has been shown to provide a better estimation of anisotropy than multiple acquistions of fewer than 20 directions [45]. We performed a voxel-based comparison, which allowed us to explore the entire brain for changes without restriction to *a priori* knowledge of regions or tracts of interest. However, a major limitation of this analysis technique is that it is reliant upon accurate image co-registration. While the registration algorithms we used are sophisticated and great care was taken to ensure the best possible co-registration, anatomical variability between subjects makes it impossible for the algorithms to produce a perfect result. Registration results are generally best in large WM structures near the center of the brain, such as the internal capsule and corpus callosum, and the quality decreases as the structures get smaller in size and closer to the cortex, where differences in gyrification can be particularly problematic. An example of false positive results that arise from registration errors in small WM

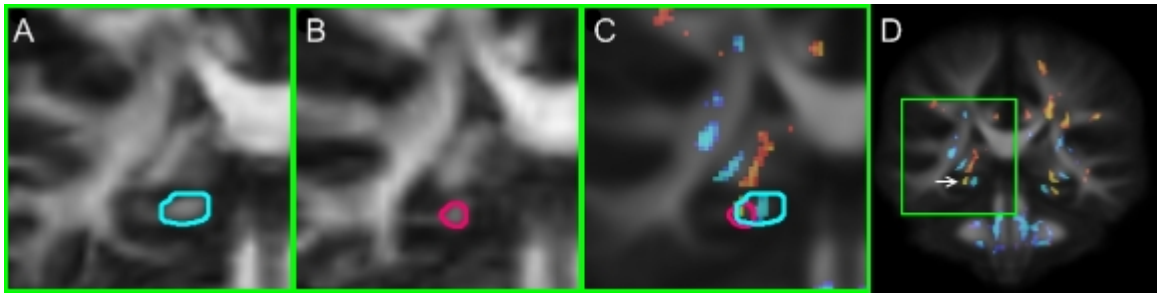

Figure 3.3: Example of Type I error due to poor registration of small WM tracts. The ventral portion of the right cingulum bundle is outlined in the normalized FA maps (Y = -32) of a control (A) and WS subject (B). An overlay of the two regions on FA_{temp} map reveals that they do not overlap (C), resulting in false positive results around the tract (arrow, D).

tracts is shown in Figure 3.3. Even within well-registered large WM structures, the registration algorithms typically used have no way of determining whether smaller WM tracts within the larger structure are properly aligned across subjects. This creates ambiguity in regions of WM that contain multiple WM tracts. An example from this study, is the external capsule. There is no way of knowing whether changes in the uncinate fasciculi, inferior fronto-occipital fasciculi, or both are the cause

of the significant differences in FA that we observed. Hoeft *et al.* faced a similar dilemna in their findings in the inferior longitudinal fasciculus (ILF) in both an ROI-style and a tract-base spatial statistics (TBSS) analysis [46], where neither method could distinguish between the ILF and IFO. Marenco *et al.* averaged diffusion parameters over pairs of entire WM tracts segmented by fiber tractography, which reduces sensitivity to localized changes, particularly since diffusion parameters can vary greatly along fiber tracts.

Although there are limitations in the analysis and interpretation of diffusion parameter changes in DTI studies, the evidence from this study and previous DTI studies of WS is consistent with structural differences, functional, and behavioral differences found in the disorder and warrant further study to improve our understanding of the role of white matter changes.

References

[1] Peoples, R. et al. A physical map, including a BAC/PAC clone contig, of the Williams-Beuren syndrome–deletion region at 7q11.23. *American Journal of Human Genetics*, 66(1):47–68, 2000.

[2] Beuren, A. J., Apitz, J., and Harmjanz, D. Supravalvular aortic stenosis in association with mental retardation and a certain facial appearance. *Circulation*, 26:1235–40, December 1962.

[3] Williams, J. C., Barratt-Boyes, B. G., and Lowe, J. B. Supravalvular aortic stenosis. *Circulation*, 24:1311–8, December 1961.

[4] Mervis, C. B. et al. The Williams syndrome cognitive profile. *Brain and Cognition*, 44(3):604–28, December 2000.

[5] Bellugi, U., Adolphs, R., Cassady, C., and Chiles, M. Towards the neural basis for hypersociability in a genetic syndrome. *Neuroreport*, 10(8):1653–7, June 1999.

[6] Klein-Tasman, B. P. and Mervis, C. B. Distinctive personality characteristics of 8-, 9-, and 10-year-olds with Williams syndrome. *Developmental Neuropsychology*, 23(1-2):269–90, 2003.

[7] Dykens, E. M. Anxiety, fears, and phobias in persons with Williams syndrome. *Developmental Neuropsychology*, 23(1-2):291–316, 2003.

[8] Klein, A. J., Armstrong, B. L., Greer, M. K., and Brown, F. R. Hyperacusis and otitis media in individuals with Williams syndrome. *The Journal of Speech and Hearing Disorders*, 55(2):339–44, May 1990.

[9] Meng, Y. et al. Abnormal spine morphology and enhanced LTP in LIMK-1 knockout mice. *Neuron*, 35(1):121–33, July 2002.

[10] Zeeuw, C. I. D. et al. CLIP-115, a novel brain-specific cytoplasmic linker protein, mediates the localization of dendritic lamellar bodies. *Neuron*, 19(6):1187–99, December 1997.

[11] Hoogenraad, C. C. et al. Targeted mutation of Cyln2 in the Williams syndrome critical region links CLIP-115 haploinsufficiency to neurodevelopmental abnormalities in mice. *Nature Genetics*, 32(1):116–27, September 2002.

[12] Zhao, C. et al. Hippocampal and visuospatial learning defects in mice with a deletion of frizzled 9, a gene in the Williams syndrome deletion interval. *Development (Cambridge, England)*, 132(12):2917–27, June 2005.

[13] Igaz, L. M., Bekinschtein, P., Izquierdo, I., and Medina, J. H. One-trial aversive learning induces late changes in hippocampal CaMKII[alpha], Homer 1a, Syntaxin 1a and ERK2 protein levels. *Molecular Brain Research*, 132(1):1–12, December 2004.

[14] Schmitt, J. E. et al. Increased gyrification in Williams syndrome: evidence using 3D MRI methods. *Developmental Medicine and Child Neurology*, 44(5):292–5, May 2002.

[15] Thompson, P. M. et al. Abnormal cortical complexity and thickness profiles mapped in Williams syndrome. *The Journal of Neuroscience*, 25(16):4146–58, April 2005.

[16] Gaser, C. et al. Increased local gyrification mapped in Williams syndrome. *NeuroImage*, 33(1):46–54, October 2006.

[17] Kippenhan, J. S. et al. Genetic contributions to human gyrification: sulcal morphometry in Williams syndrome. *The Journal of Neuroscience*, 25(34):7840–6, August 2005.

[18] Essen, D. C. V. et al. Symmetry of cortical folding abnormalities in Williams syndrome revealed by surface-based analyses. *The Journal of Neuroscience*, 26(20):5470–83, May 2006.

[19] Galaburda, A. M. et al. Dorsal forebrain anomaly in Williams syndrome. *Archives of Neurology*, 58(11):1865–9, November 2001.

[20] Jackowski, A. P. and Schultz, R. T. Foreshortened dorsal extension of the central sulcus in Williams syndrome. *Cortex*, 41(3):282–90, June 2005.

[21] Mobbs, D. et al. Frontostriatal dysfunction during response inhibition in Williams syndrome. *Biological Psychiatry*, 62(3):256–61, August 2007.

[22] Meyer-Lindenberg, A. et al. Neural correlates of genetically abnormal social cognition in Williams syndrome. *Nature Neuroscience*, 8(8):991–993, 2005.

[23] Meyer-Lindenberg, A. et al. Neural basis of genetically determined visuospatial construction deficit in Williams syndrome. *Neuron*, 43(5):623–31, September 2004.

[24] Meyer-Lindenberg, A. et al. Functional, structural, and metabolic abnormalities of the hippocampal formation in Williams syndrome. *The Journal of Clinical Investigation*, 115(7):1888–95, July 2005.

[25] Hoeft, F. et al. More is not always better: increased fractional anisotropy of superior longitudinal fasciculus associated with poor visuospatial abilities in Williams syndrome. *The Journal of Neuroscience*, 27(44):11960–5, October 2007.

[26] Marenco, S. et al. Genetic contributions to white matter architecture revealed by diffusion tensor imaging in Williams syndrome. *Proceedings of the National Academy of Sciences of the United States of America*, 104(38):15117–22, September 2007.

[27] Oldfield, R. C. The assessment and analysis of handedness: the Edinburgh inventory. *Neuropsychologia*, 9(1):97–113, March 1971.

[28] Netsch, T. and van Muiswinkel, A. Quantitative evaluation of image-based distortion correction in diffusion tensor imaging. *IEEE Transactions on Medical Imaging*, 23(7):789–798, 2004.

[29] Maes, F., Collignon, A., Vandermeulen, D., Marchal, G., and Suetens, P. Multimodality image registration by maximization of mutual information. *IEEE Transactions on Medical Imaging*, 16(2):187–98, 1997.

[30] Li, R. *Automatic placement of regions of interest in medical images using image registration*. M.S. Thesis in Electrical Engineering and Computer Science, Vanderbilt University, 2001.

[31] Rohde, G. K., Aldroubi, A., and Dawant, B. M. The adaptive bases algorithm for intensity-based nonrigid image registration. *IEEE Transactions on Medical Imaging*, 22(11):1470–9, 2003.

[32] Bullmore, E. T. et al. Global, voxel, and cluster tests, by theory and permutation, for a difference between two groups of structural MR images of the brain. *IEEE Transactions on Medical Imaging*, 18(1):32–42, 1999.

[33] Schmitt, J. E., Eliez, S., Warsofsky, I. S., Bellugi, U., and Reiss, A. L. Corpus callosum morphology of Williams syndrome: relation to genetics and behavior. *Developmental Medicine and Child Neurology*, 43(3):155–9, March 2001.

[34] Tomaiuolo, F. et al. Morphology and morphometry of the corpus callosum in Williams syndrome: a T1-weighted MRI study. *Neuroreport*, 13(17):2281–4, December 2002.

[35] Luders, E. et al. Callosal morphology in Williams syndrome: a new evaluation of shape and thickness. *Neuroreport*, 18(3):203–7, February 2007.

[36] Mobbs, D. et al. Anomalous brain activation during face and gaze processing in Williams syndrome. *Neurology*, 62(11):2070–6, June 2004.

[37] Sarpal, D. et al. A genetic model for understanding higher order visual processing: functional interactions of the ventral visual stream in williams syndrome. *Cerebral Cortex*, 18(10):2402–9, October 2008.

[38] Trauner, D. A., Bellugi, U., and Chase, C. Neurologic features of Williams and Down syndromes. *Pediatric Neurology*, 5(3):166–8, 1989.

[39] Chapman, C. A., du Plessis, A., and Pober, B. R. Neurologic findings in children and adults with Williams syndrome. *Journal of Child Neurology*, 11(1):63–5, 1996.

[40] Gagliardi, C., Martelli, S., Burt, M. D., and Borgatti, R. Evolution of neurologic features in Williams syndrome. *Pediatric Neurology*, 36(5):301–6, May 2007.

[41] Hocking, D., Rinehart, N., McGinley, J., and Bradshaw, J. Gait function in adults with Williams syndrome. *Experimental Brain Research*, 2008.

[42] Aizawa, H. et al. Phosphorylation of cofilin by LIM-kinase is necessary for semaphorin 3A-induced growth cone collapse. *Nature Neuroscience*, 4(4):367–373, April 2001.

[43] Endo, M. et al. Control of Growth Cone Motility and Morphology by LIM Kinase and Slingshot via Phosphorylation and Dephosphorylation of Cofilin. *J. Neurosci.*, 23(7):2527–2537, April 2003.

[44] Bagri, A., Cheng, H., Yaron, A., Pleasure, S. J., and Tessier-Lavigne, M. Stereotyped Pruning of Long Hippocampal Axon Branches Triggered by Retraction Inducers of the Semaphorin Family. *Cell*, 113(3):285–299, May 2003.

[45] Jones, D. K. The effect of gradient sampling schemes on measures derived from diffusion tensor MRI: a Monte Carlo study. *Magnetic Resonance in Medicine*, 51(4):807–15, April 2004.

[46] Smith, S. M. et al. Tract-based spatial statistics: voxelwise analysis of multi-subject diffusion data. *Neuroimage*, 31(4):1487–505, 2006.

CHAPTER IV

SEMI-AUTOMATED, TRACT-BASED ANALYSIS OF DIFFUSION TENSOR IMAGING STUDIES

Introduction

As the use of diffusion tensor imaging (DTI) has increased in the field of neuroimaging, greater attention is being paid to the limitations of traditional data analysis tools and the need for more accurate analysis methods for performing group comparisons of the data. Region of interest (ROI) methods require *a priori* knowledge of the location of the affected tissue and are time consuming, susceptible to intra- and inter-rater error, and susceptible to partial volume averaging effects if the ROI size and shape do not match the structure of interest well. Voxel-based analysis (VBA) methods are much more advantageous in that they allow an exploratory comparison without prior knowledge of the locations of affected tissue. However, VBA methods require accurate image normalization which is difficult to achieve due to anatomical differences between individuals. Registration results are generally good in large white matter (WM) structures, such as the corpus callosum and internal capsule. However, even with the use of sophisticated nonlinear registration algorithms, reliability in the registration results decreases in small white matter structures. Typically, image normalization is performed using scalar images derived from the diffusion tensor data, such as the non-diffusion weighted images or the fractional anisotropy (FA) maps, which raises another issue. Even when registration results appear to be good across subjects in large white matter structures, they may consist of a set of smaller fiber pathways, and the algorithm has no way of determining whether those smaller pathways are aligned or not, resulting in comparison of different tracts between subjects. This is particularly an issue if different WM tracts are affected by the disease or disorder in unique ways.

Methods that incorporate additional information from the diffusion tensor have been proposed as alternatives to the traditional analysis methods in an attempt to avoid their associated limitations. Tract-based methods where statistical comparisons are performed at corresponding locations along

a tract of interest were first proposed by Mori *et al.* [1] and Fillard *et al.* [2]. Early attempts at these methods were limited in their usefulness because the methods used to define point correspondence across subjects were based upon a single tract of interest and used anatomical landmarks that could not be easily translated to other WM pathways [3–6]. The challenges in defining accurate point correspondence in multiple tracts of interest led to the introduction of alternative methods: tract-based ROI [7] and tract-based spatial statistics (TBSS) [8]. Tract-based ROI methods utilize fiber tracking to segment specific WM tracts-of-interest and then treat the tracking results as a single large ROI, averaging the diffusion parameters over the entire volume of the tract. While this method is relatively easy to implement, just as a typical ROI analysis is, many studies still rely upon manual selection of seed points in each data set, which is time consuming and susceptible to user-introduced error. Another problem is that it is unclear whether the diffusion parameters should be averaged over the entire length of the tractography results or not. The accuracy of fiber tracking results decreases as the distance from the seed points increases, and regions near the ends of the fibers typically have low FA. Also, it is known that diffusion parameters, particularly FA, often vary along the length of a WM tract as its structure and relationship with other tracts varies. (For example, see [1, 3, 5].) Averaging the parameters over such a large region reduces the sensitivity to localized changes within the tract. Alternatively, the TBSS method attempts to minimize the effects of poor registration while keeping a voxel-wise analysis. The name is misleading, as no fiber tracking is involved. Images are normalized and the FA is skeletonized to define the centers of the major WM bundles in the image. These WM skeletons are mapped onto a template and a voxel-wise analysis is performed within the skeletons only. This method provides a global comparison with no *a priori* knowledge of the locations of the differences necessary. However, with the exception of the core of the corpus callosum, there is generally more than one pathway passing through a given region of WM, and there is no way to distinguish which tract may be causing any detected differences.

Proposed here is a semi-automated, tract-based analysis method for DTI studies, which is performed in conjunction with a tradition voxel-based analysis. There are four major steps, and the algorithms used to perform each step are user-defined:

1. *Image normalization* to allow for an exploratory, voxel-based analysis for comparison and assist in automating the tract-based analysis.

2. *Tract segmentation* to isolate the white matter tracts of interest.

3. *Tract parameterization* to simplify the definition of point correspondence.

4. *Definition of point correspondence* to perform statistical comparisons of diffusion parameters along the tracts of interest between subject groups.

We describe in detail the methods we used for each step in the process. We then describe the application of our tract-based analysis to a study of schizophrenia, comparing diffusion parameters along four sets of major association pathways in the brain: the bilateral arcuate, cingulum, inferior fronto-occipital, and uncinate fasciculi. We also performed a standard voxel-based analysis and compare results between the two methods.

Methods

Subjects

Data from 22 normal controls (NC) and 33 schizophrenia (SZ) outpatients were analyzed. The NC group consisted of 10 females and 12 males; all were right-handed except for one female; and their mean age was 36 years (range = 22 to 53 years). The SZ group consisted of 15 females and 18 males; 5 were left-handed and three were ambidextrous; their mean age was 40 years (range = 23 to 54 years); and all 33 were on medication to control symptoms of the disease at the time of the investigation. The images from an additional NC were used as the initial target for the purpose of image co-registration. The target subject was a 36 year-old, right handed, female. Handedness was determined by the Edinburgh handedness inventory [9]. Informed consent was obtained for each subject and all imaging was done in accordance with Institutional Review Board requirements.

Table 4.1: Subject demographics

Group		N	Age (years) Range	Mean	Std. Dev.	Handedness Right	Left	Ambidextrous
NC		22	22 - 53	36	9	21	1	0
	Female	10	26 - 53	36	8	11	1	0
	Male	12	22 - 51	35	10	10	0	0
SZ		33	23 - 54	40	10	25	5	3
	Female	15	23 - 54	45	9	12	2	1
	Male	18	23 - 52	35	9	13	3	2

Image Acquisition

All images were acquired using a Philips Intera Achieva 3T MRI scanner with high-performance gradient coils (80 mT/m gradient strength and 100 mT/m/ms slew-rate) and an 8 channel SENSE (sensitivity encoding) head coil. High angular resolution diffusion weighted images (DWIs) were acquired with 92 diffusion-encoding directions. Single-shot EPI and SENSE were used to decrease total scan time. The imaging parameters used were TE = 48 ms, TR = 10,000 ms, SENSE factor = 3, tr(b) = 1000 s/mm^2, FOV = 240 x 240 mm^2, and a matrix size of 96 x 96. Whole-brain coverage was obtained with 55 axial slices in 17 minutes and 20 seconds. A high-resolution T2-weighted anatomical data set, slice-matched to the DWIs, and a high-resolution 3D T1-weighted anatomical volume were also acquired for use in the image co-registration process. The T2-weighted anatomical images were obtained with a turbo spin echo sequence. The slice number, thickness, and location were exactly the same as the DWIs, but with higher in-plane resolution resulting in a voxel size of 0.45 x 0.45 x 2.5 mm^3. The imaging parameters used were TE = 80 ms, TR = 6000 ms, FOV = 230 x 230 mm^2, and an reconstructed matrix size of 512 x 512, resulting in a total scan time of 3 minutes and 36 seconds. The T1-weighted 3D anatomical volume was acquired using a multi-shot gradient echo sequence with TE = 4.6 ms, TR = 8.9 ms, SENSE factor = 2, FOV = 256 x 256 mm^2. The

volume consisted of 176 sagittal slices with an isotropic voxel size of 1 mm^3, and total scan time was 4 minutes and 37 seconds.

Image Pre-processing

Eddy current distortion and bulk subject motion were corrected within the original DWIs with the Philips Research Imaging Development Environment (PRIDE) Diffusion Registration tool (release 0.5). This tool performs an affine registration of each DWI to its corresponding non-diffusion-weighted (b0) image [10]. Occasional artifacts from spike noise and incomplete fat saturation were observed in some of the images. However, with 92 diffusion-encoding directions, we were able to remove the corrupted images and still have a sufficient number of images for proper estimation of the tensor. Individual images affected by spike noise were automatically detected and removed from the data set prior to tensor calculation. Also, the voxels corrupted by fat signal shifted into the brain were detected and excluded from statistical analysis. (See Appendix A for more details.) The distortion-, artifact-, and motion-corrected DWIs were then used to calculate the diffusion tensor maps and FA maps, as well as extract the b0 image volume, with a modified version of the PRIDE Fiber Tracking tool (Version 6.0a1). The in-house modifications rejected diffusion-weighted voxels corrupted by bulk and physiological motion. (See Appendix A for more details.)

Image Registration

Individual FA maps were normalized using a two-step process. First, a study-specific, average FA template was created by co-registering the individual FA maps to the high-resolution T1-weighted anatomical image of the target control and averaging the resulting normalized FA maps. second, the original FA maps were co-registered to the average FA template, to minimize bias that might have been introduced by selection of a single control as the initial template. Mutual information based linear [11, 12] and nonlinear [13] registration programs were provided by the Medial Image Processing group in the Department of Electrical Engineering and Computer Science. Each non-linear registration step was initialized a linear registration step, and trilinear interpolation was used

when applying the transformations. When multiple registration steps were required (e.g. combining intra- and inter-subject registrations) the transformations resulting from each intermediate step were combined to create a single transformation, which was then applied to the reference image to minimize interpolation effects. A detailed description of the process is presented below.

Creation of the study-specific, average FA template required multiple intermediate steps involving both intra- and inter-subject coregistration for each subject *i*. The registration was performed using the b0 images in place of the FA maps, since they are inherently co-registered and they have T2-weighted contrast, providing better results when normalizing to anatomical images. A graphical representation of this process is displayed in Figure 4.1. The b0 images of each subject ($b0_i$) were co-registered to the T1-weighted images of the target subject ($T1_{\mathrm{TARG}}$). The T1-weighted volume was chosen as the temporary common image space because it had isotropic voxel size and could be used to overlay results. First, to reduce distortion due to susceptibility artifacts, the non-diffusion-weighted image ($b0_i$) was registered to its own high-resolution T2-weighted volume ($T2_i$) with a nonlinear registration, which was initialized by the results of a rigid registration. This resulted in two transformations: $\Psi_{1,i}$ and $\Psi_{2,i}$ for the rigid and nonlinear steps, respectively. Next, the $T2_i$ image, as well as the the $T2_{\mathrm{TARG}}$ image, was stripped of extra-cranial tissue using an in-house program implemented in IDL (Interactive Data Language) . Then the skull-stripped $T2_i$ image was registered to the $T2_{\mathrm{TARG}}$ image with a nonlinear registration, initialized by the results of a rigid registration that included scaling. This resulted in two additional transformations: $\Psi_{3,i}$ and $\Psi_{4,i}$ for the rigid and nonlinear steps, respectively. Next, the $T2_{\mathrm{TARG}}$ image was rigidly registered to the $T1_{\mathrm{TARG}}$ image, resulting in transformation Ψ_5. The five transformations ($\Psi_{1,i}$, $\Psi_{2,i}$, $\Psi_{3,i}$, $\Psi_{4,i}$, Ψ_5) were combined for each subject to create a single transformation $\Psi_{\mathrm{TOTAL1},i}$, which was then applied to the subject's FA map, (FA_i). The transformed FA maps were then averaged to create the template ($FA^{\mathrm{AVG}}_{\mathrm{TARG}}$). Then, each subject's original FA map (FA_i) was co-registered to the study-specific template ($FA^{\mathrm{AVG}}_{\mathrm{TARG}}$) with a nonlinear registration, initialized by a rigid registration with scaling, producing two new transformations: ($\Psi_{6,i}$, $\Psi_{7,i}$) for the rigid and nonlinear registrations, respectively.

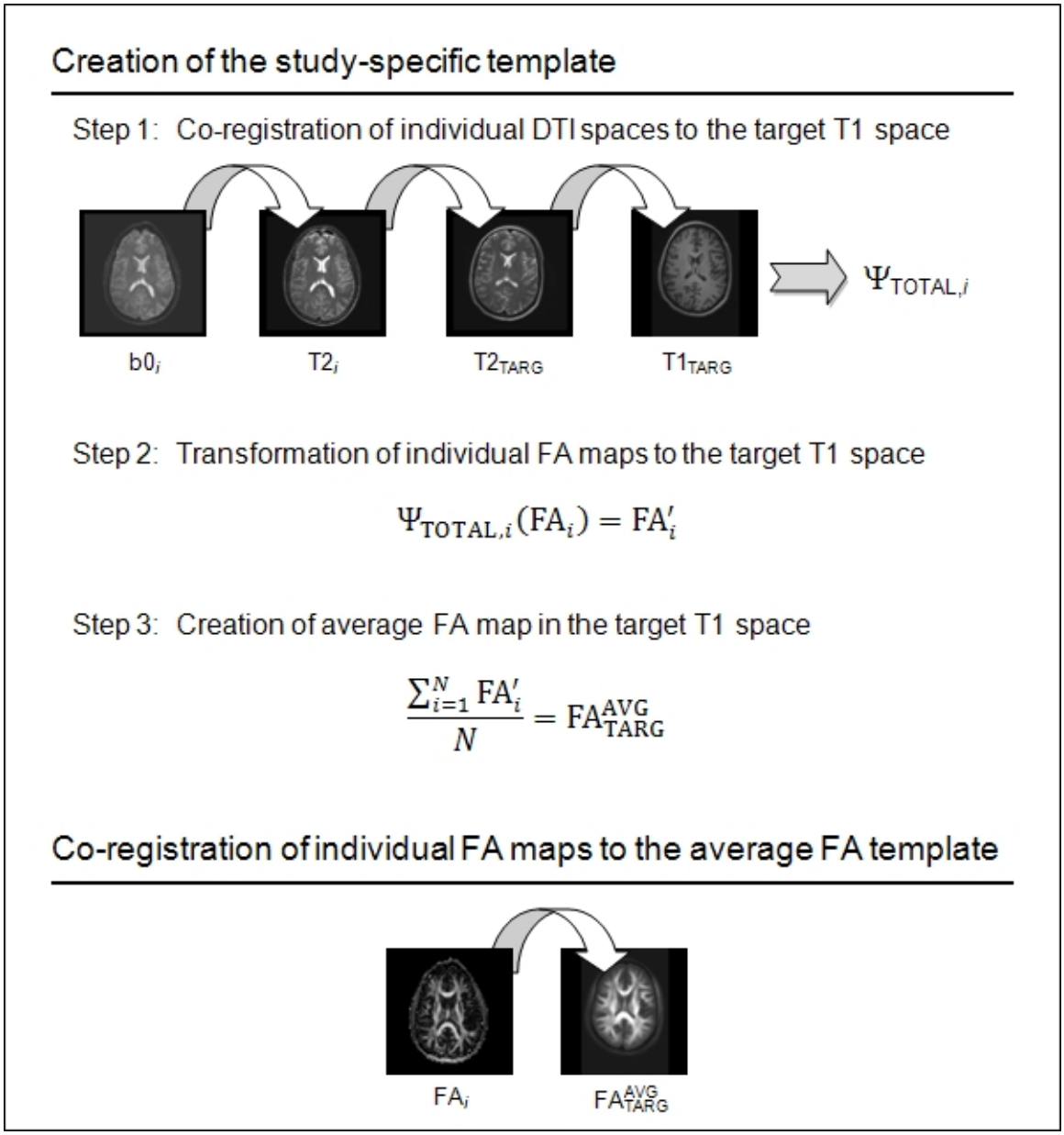

Figure 4.1: Image co-registration process.

These two transformations were combined to produce $\Psi_{\mathrm{TOTAL2},i}$, which was then applied to FA_i to produce $\mathrm{FA}_i^{\mathrm{AVG}}$, the normalized FA map used in the statistical analysis.

Semi-automated WM Tract Isolation

Fiber tracking was performed in the native image space of each subject to isolate the left and right tracts of 4 major association pathways possibly affected in schizophrenia: the cingulum, uncinate, arcuate, and inferior fronto-occipital fasciculi. The seed point selection process was semi-automated to minimize user interaction and processing time, and a multi-ROI approach [14] was used to minimize the chance of tracking fibers within other WM pathways located near the tracts of interest.

Seed Selection

Two seed coordinates in the core of the most coherent portions of each tract of interest were defined manually in the average FA template. These coordinates were then transformed to the native image space of each subject via the total transformation defined in the normalization of the individual FA maps to the template FA map. Once in the native image space, spherical seed volumes surrounding each original seed point were created. The points in the volume were spaced evenly at 0.7 voxels on a Cartesian grid, extending from the original seed point with a predefined radius. The radii were generously sized in order to compensate for possible registration errors and inter-subject anatomic variability. The default radius length was chosen to be 5 voxels, as a compromise between maximizing the number of fibers tracked within the tract of interest and minimizing the number of extraneous fibers, and the radii were scaled to account for global scaling differences between the individual subjects and the template brain, if necessary. The seed spacing of 0.7 voxels provided consistent tracking results, while minimizing redundancy in the tracking results that would lead to unnecessarily increased processing time in later stages of the process.

Fiber tracking and editing

The PRIDE Fiber Tracking Tool was used to perform deterministic, multi-ROI fiber tracking with the predefined seed regions. The PRIDE tool is an implenatation of the FACT algorithm [15] and was chosen because of its advanced visualization features and the ease of making modifications to the program in IDL. The tracking parameters used were a step size of 0.5 voxels, minimum FA threshold of 0.2, and a maximum deflection angle of 27°. The coordinates defining the resulting fibers for each subject were saved in text files for further processing. The tracking results for all subjects in the study were loaded into an in-house program implemented in IDL which allows the user to view the results from all subjects in the study in the common image space and manually select which fibers will be considered in further analysis steps. This serves two main functions. First, it allows the user to remove extraneous fibers outside the tract of interest from the analysis process. second, it also allows the user to identify and separate subsets of fibers within a particular tract, such as the arcuate fasciculus, which contains fibers traveling from the frontal lobe to the superior temporal gyrus, the middle temporal gyrus, and Geschwind's territory in the parietal lobe. First, in order to simplify the fiber editing computation, the native-space fibers of the tract of interest for each subject are clustered using methods described by Corouge *et al*.[16] with a distance metric described by Zhang *et al.* [17]. Then the medial axis of each fiber cluster is defined with methods described by Ding *et al.* [18]. The mean cluster axes for each subject are then transformed to the common image space and displayed in an interactive viewer which allows the user to select/deselect clusters for further processing. When the user is satisfied with the results, the program automatically removes the individual fibers associated with any clusters that have been removed from the data set and saves the 'edited' version of the fiber tracts. Even after this editing process, there may still be differences in the branching of the tracts between subjects. In order to ensure that the same portion of the tract is being compared across all subjects, a "trimming" process was performed. A statistical map of the proportion of subjects whose edited fibers passed through a given voxel was created and masked, so that only voxels that contained fiber contributions from a minimum of a

user-selected percentage of subjects were included. This mask was then used to remove (or trim) the portions of the individual fibers that lay outside the mask.

Definition of point correspondence between tracts

The definition of point correspondence across subjects along a given tract-of-interest was performed in multiple steps. First, the mean axis of the remaining fibers was calculated for each subject in the same manner as the mean axes of the fiber clusters mentioned above. Next, the axes were reparameterized using cubic b-splines in a manner similar to the method described by Corouge *et al.* [19]. Parameterization was initiated in a plane located at the centroid of the axes and oriented perpendicular to the mean direction of the axes passing through it, and the axes were sampled such that the resulting spacing between sample points along each axis was roughly equivalent to 2.5 mm, the voxel spacing in the native DTI space. Points with the same arc length away from and position relative to the initial plane on each axis were then considered to correspond to the same portion of the tract across all subjects.

Statistical Analysis

Voxel-based Analysis

The normalized FA maps for the NC and SZ groups were compared on a voxel-wise basis with a two-sample t-test. No smoothing was applied to the maps prior to analysis. The resulting significance maps were thresholded at the $p < 0.05$ level and masked so that only voxels with an average FA value of 0.2 or greater in the FA_{temp} remained. Permutation testing was performed with the same significance level and masking to determine the minimum significant cluster size (in 3 dimension) according to the methods described by Bullmore *et al.* [20]. Only clusters with a volume greater than 93 voxels (93 mm^3) were considered to be significant. The average FA template and map of significant clusters were transformed to the Talairach space for visualization.

Tract-based Analysis

The coordinates of each subject's "corresponding" points were transformed to the native image space, and the FA values corresponding to those coordinates were interpolated using trilinear interpolation. Then the FA values of the two group's fiber bundles were compared performing a two-sample t-test at each of the corresponding points along the medial axes. Differences were considered to be significant for $p < 0.05$ (uncorrected).

Comparison of analysis methods

Variance in the FA values within the control group was compared between the two methods. A DTI data set was also acquired for the subject used as the initial target for the image normalization process. This subject was included in the automated fiber tracking process but not in subsequent group statistical comparisons. The coordinates along the reparameterized axes in the target's fiber tracts were considered to be corresponding locations between the VBA and TBA. The variance in the FA values of the NC group were calculated at these locations and compared between the methods with the Levene's test for equality in variance [21].

Results

Fiber tracking

The semi-automated tracking process was able to extract the eight tracts-of-interest in all subjects, except for a few cases: one SZ subject for the left arcuate, 3 SZ subjects for the right arcuate, two SZ subjects for the left IFO, and 3 SZ subjects and 1 NC for the right IFO. There were no significant differences in the number of fibers per tract between groups (AL: p = 0.68, AR: p = 0.77, CL: p = 0.65, CR: p = 0.64, IFOL: p = 0.18, IFOR: p = 0.51, UL: p = 0.37, UR: p = 0.92). Typical results from a single subject are shown in Figure 4.2. The tracking results for the left arcuate fasciculus revealed three subsets of fibers with connections between the frontal lobe and the superior temporal gyrus (STG) , the middle temporal gyrus (MTG) , and occasionally Geschwind's Territory. The

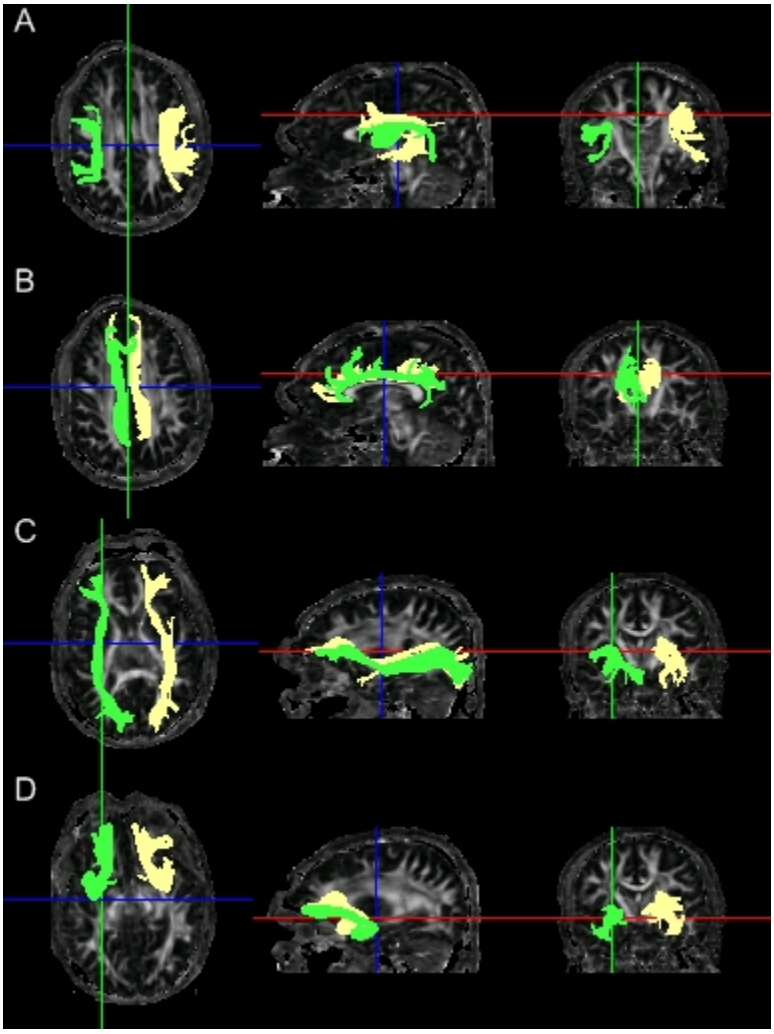

Figure 4.2: Fiber tracking results from a single subject. From left to right: axial, sagittal, and coronal, projections of typical fiber tracking results (prior to fiber editing) for the right (green) and left (yellow) arcuate (A), cingulum (B), inferior fronto-occipital (C), and uncinate (D) fasciculi.

right arcuate generally contained connections to the superior and middle temporal gyri. The uncinate fasciculus also appeared to contain two subsets of fibers, one connecting the temporal lobe with the prefrontal (PF) area and another subset connecting the temporal lobe with the dorso-lateral prefrontal cortex (DLPFC). These sub-tracts were all extracted during the fiber editing process and analyzed individually in subsequent statistical comparisons, with the exception of the portion of the left arcuate traveling to Geschwind's territory, which was not found in all subjects.

TBA

In the tract-based comparison, 5 of the 12 tracts-of-interest contained localized regions of significantly reduced FA in the SZ group: AL (MTG), AR (MTG), IFOL, UL (PF), and UR (PF). Plots of the mean FA for each group and the locations of the significant reductions are shown in Figures 4.3 and 4.4. Representative Talairach coordinates for each significant region are listed in Table 4.2.

VBA

The voxel-based analysis revealed several clusters of significantly reduced FA in the schizophrenics compared to the controls, including regions near the association tracts-of-interest in this study. Table 4.2 lists the locations of these regions in Talairach space. There were several other regions of reduced FA, including the bilateral posterior limb of the internal capsule, bilateral corona radiata in the posterior portion of the frontal lobe, the genu, rostral body, posterior middle body, and isthmus of the corpus callosum, and bilateral regions of frontal WM at the crossing of the the corpus callosum and the corona radiata. There were also five small clusters of increased FA located in the left and right cerebellar WM, right occipital WM, and right and left frontal WM.

Comparison of VBA and TBA

Plots of the within-group (NC) variance in FA as a function of position along the tract for the VBA and TBA methods are shown in Figures 4.5 and 4.6. The within-group variance of points defined by the TBA was significantly lower in only the posterior portion of the IFOR and IFOL tracts. The

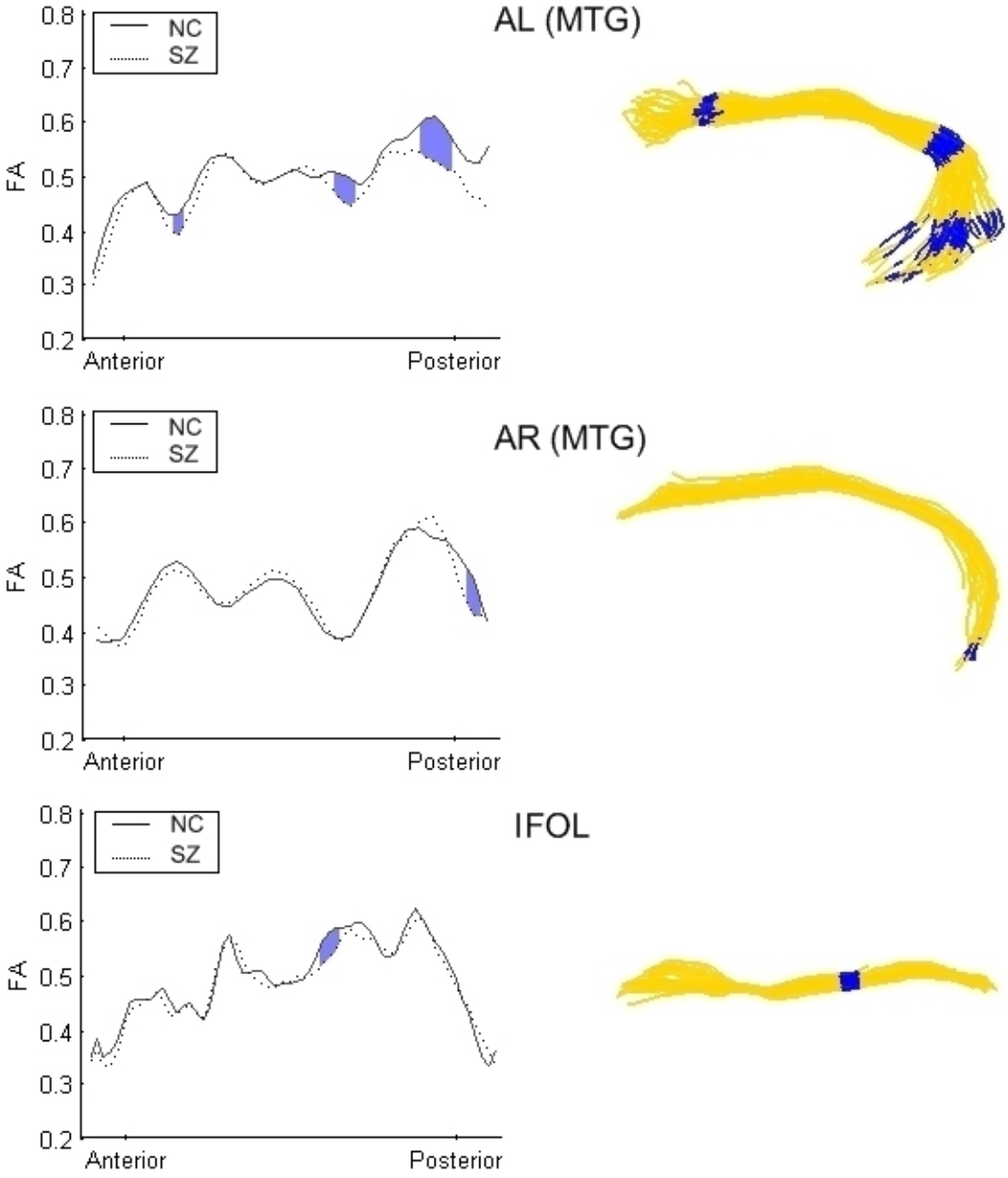

Figure 4.3: Tract-based analysis results for AL (MTG), AR (MTG), and IFOL. Plots of the mean FA as a function of position along the tract (left) and projections of the subjects' medial axes for each tract (right), with the locations of significantly reduced FA in SZ compared to NC marked (blue).

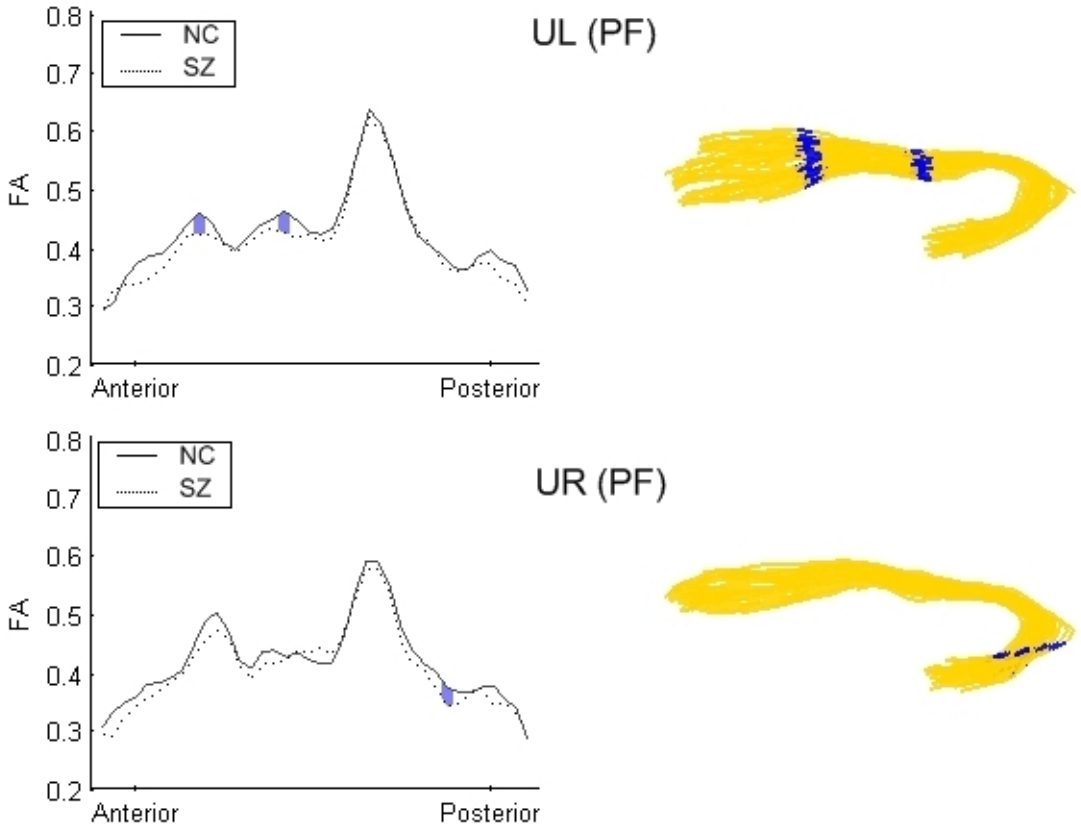

Figure 4.4: Tract-based analysis results for UL (PF) and UR (PF). Plots of the mean FA as a function of position along the tract (left) and projections of the subjects' medial axes for each tract (right), with the locations of significantly reduced FA in SZ compared to NC marked (blue).

Table 4.2: Regions of reduced FA in or near the tracts-of-interest.

WM Region	VBA Talairach Coordinates			TBA Talairach Coordinates		
	X	Y	Z	X	Y	Z
AL	-	-	-	-49	-35	-7
	-	-	-	-36	-4	26
	-	-	-	-36	-38	20
	-	-	-	-42	-40	2
	-45	-17	29	-	-	-
	-43	-43	22	-	-	-
AR	-	-	-	47	-46	1
	48	-16	24	-	-	-
	39	-23	35	-	-	-
	38	-6	37	-	-	-
	39	-3	27	-	-	-
	43	-51	21	-	-	-
UL/FOL	-19	17	-10	-20	18	-8
	-	-	-	-17	35	-7
UR/FOR	26	-5	-11	-	-	-
FOL	-40	-33	-4	-39	-32	-4
FOR	37	-39	-3	-	-	-
UR	-	-	-	35	1	-20

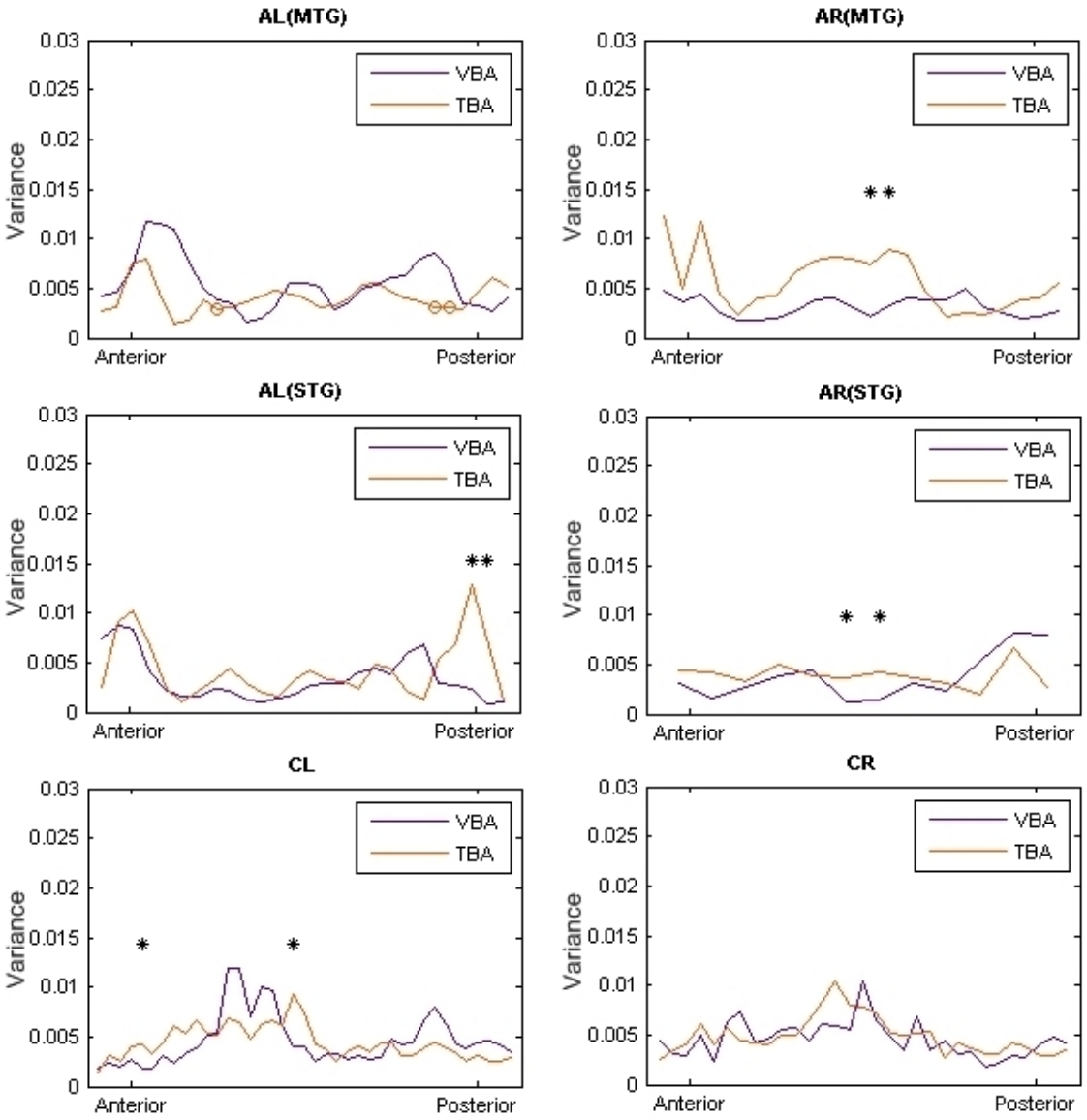

Figure 4.5: Comparison of within-group variance in TBA and VBA: Arcuate & cingulum. Within-group variance for the NC group is plotted as a function of position along the tract for the VBA (purple) and TBA (orange) methods. Circles indicate locations of significant between-group differences in mean FA.

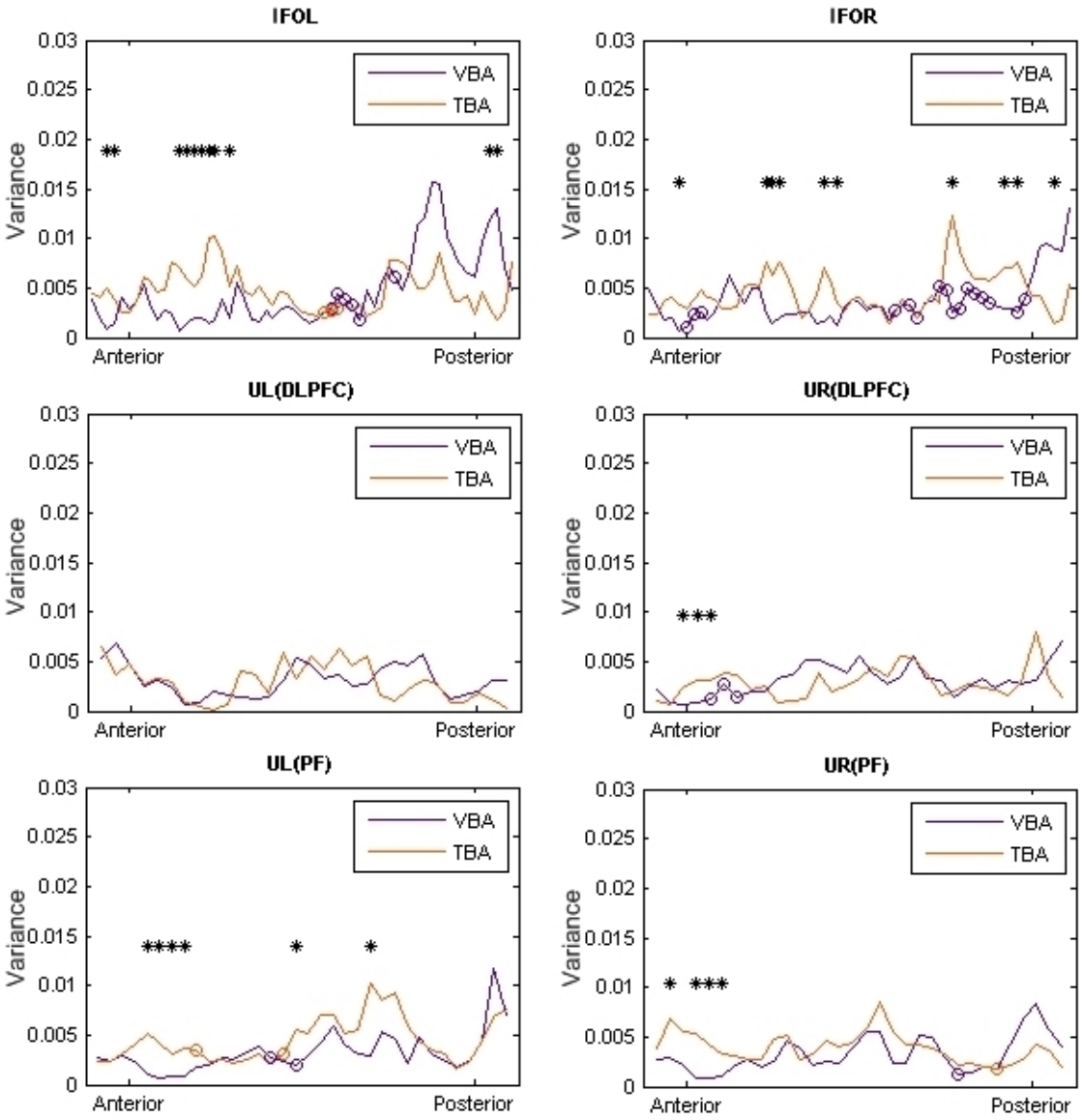

Figure 4.6: Comparison of within-group variance in TBA and VBA: IFO and uncinate. Within-group variance for the NC group is plotted as a function of position along the tract for the VBA (purple) and TBA (orange) methods. Circles indicate locations of significant between-group differences in mean FA.

variance was significantly higher in the TBA in portions of the AR (MTG), AL (STG), AR (STG), CL, UL (PF), UR (PF), and UR (DLPFC).

Discussion

In this study, we have proposed a framework for performing tract-based comparisons of diffusion parameters between groups, applied it to a study of schizophrenia, and compared the results with a traditional voxel-based analysis. Both analysis methods showed reduced FA in regions consistent with recent DTI studies of schizophrenia [7, 22–30]: the right and left arcuate fasciculi, the left IFO, and the left uncinate/IFO. The tract-based analysis showed an additional small region of reduced FA in the temporal portion of the right uncinate that was not seen in the voxel-based analysis, and the voxel-based analysis showed regions of reduced FA in the IFOR and UR/IFOR that were not found in the tract-based analysis. Some differences in the locations of the regions of significant differences are to be expected, as the tract-based analysis only compared FA values within the cores of specific tracts of interest, while the voxel-based analysis examined all WM.

The semi-automated fiber tracking scheme performed well in most cases. In 6 of the 10 cases where no fiber tracts were identified by multi-ROI tracking, inspection of the data revealed that artifacts from incomplete fat saturation disrupted the fiber tracking. Inspection of the image data for the remaining 4 cases revealed no obvious image artifacts that would have affected the tracking results, so fiber tracking was performed with manual placement of seed ROIs to investigate. In one of the SZ data sets with a missing right arcuate, there appeared to be no connections between the frontal and temporal lobes via the superior longitudinal fasciculus (or SLF). In the NC with no right IFO, there were fibers that connected the frontal and occipital lobes. However, the fibers terminated in the dorsolateral prefrontal cortex just after passing through the external capsule and did not extend toward the frontal lobe as the IFO fibers in the left hemisphere of this subject did. The SZ subject with missing left and right IFO tracking results did have connections between the frontal and occipital lobes. However, the occipital extensions of the tracts went around the automatically

generated occipital ROIs. Perhaps this was due to either misregistration errors large enough to prevent the ROIs from catching the fibers or to alterations in the pathways.

It is difficult to accurately compare the two analysis methods without a ground-truth data set. One would generally assume that the method that minimized within-group variance would be more sensitive to between-group differences, so the variance of FA values within the control group at corresponding locations in the voxel-based and tract-based data were compared. The results revealed that the tract-based method generally did not produce significantly lower variance within the control group. Closer inspection of the data reveals interesting results. First, a region where the within-group variance and the statistical comparison between the SZ and NC groups were the same in both methods, such as the middle portion of the FOL, was inspected (Figure 4.7). Normalization results in this location were excellent, and it is a region where the WM tracts are highly coherent with very little branching to nearby cortical regions. Next, a region of the left arcuate where the tract-based analysis provided lower within-group variance and found a significant between-group difference, while the voxel-based analysis did not was examined (Figure 4.8). In this case, image normalization was poor, resulting in that particular voxel falling inside the tract in some subjects and outside the WM altogehter in other subjects in the voxel-based analysis. It appears that the precautions taken in the fiber tracking methods to minimize the effects of poor image co-registration allowed the tract-based analysis method to provide a more accurate comparison of FA in this portion of the tract. Finally, a region in the right IFO was examined, where the voxel-based analysis provided significantly lower within-group variance and found a significant between-group difference, while the voxel-based analysis did not (Figure 4.9). Inspection of the normalized FA maps and individual color-coded FA maps revealed a case where the image co-registration, which was based solely upon the scalar FA images, performed relatively well but failed to align smaller fiber tracts within larger WM structures. The co-registration process may have artificially (and erroneously) reduced the within-group variance in this region.

While voxel-based analysis relies heavily upon accuracy in image co-registration, tract-based

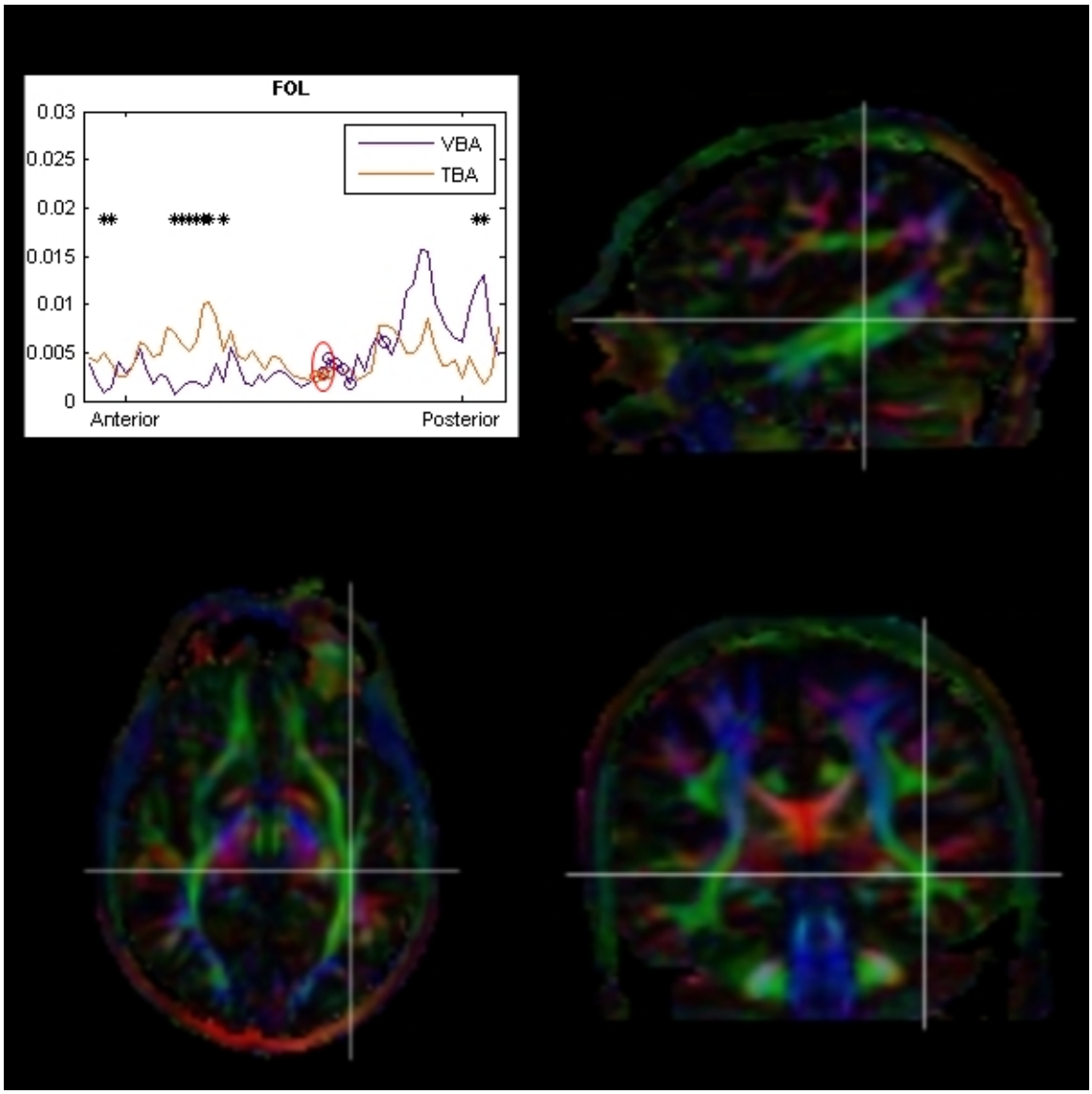

Figure 4.7: Example of similar results in both TBA and VBA methods. Significantly reduced FA was found in the temporal portion of the left IFO of the SZ group by both methods. The red circle in the plot of within-group variance (top left) indicates the position along the tract that corresponds to the cross-hairs in the sagittal (top right), axial (bottom left) and coronal views of the color coded FA map for a single subject.

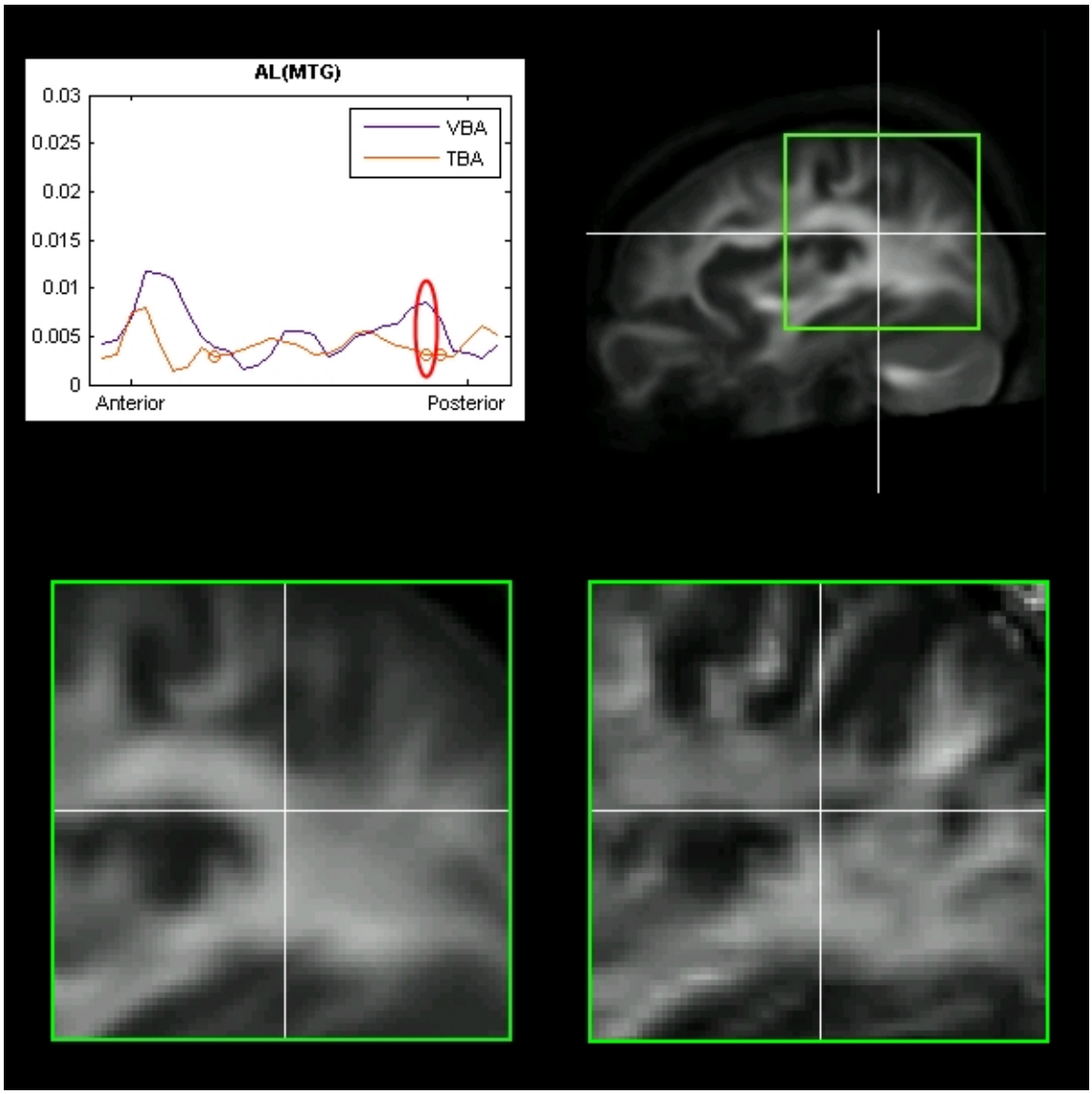

Figure 4.8: Example of different results in TBA and VBA due to registration errors. Significantly reduced FA in the SZ group was found in the temporo-parietal region of the AL (MTG) by the TBA method and not by the VBA method in this portion of the tract. The red circle in the plot of within-group variance (top left) indicates the position along the tract that corresponds to the cross-hairs in the sagittal (top right). In some subjects, such as the one shown on the bottom left, this point fell within WM. In others, such as the one shown on the bottom, this point fell outside of the WM.

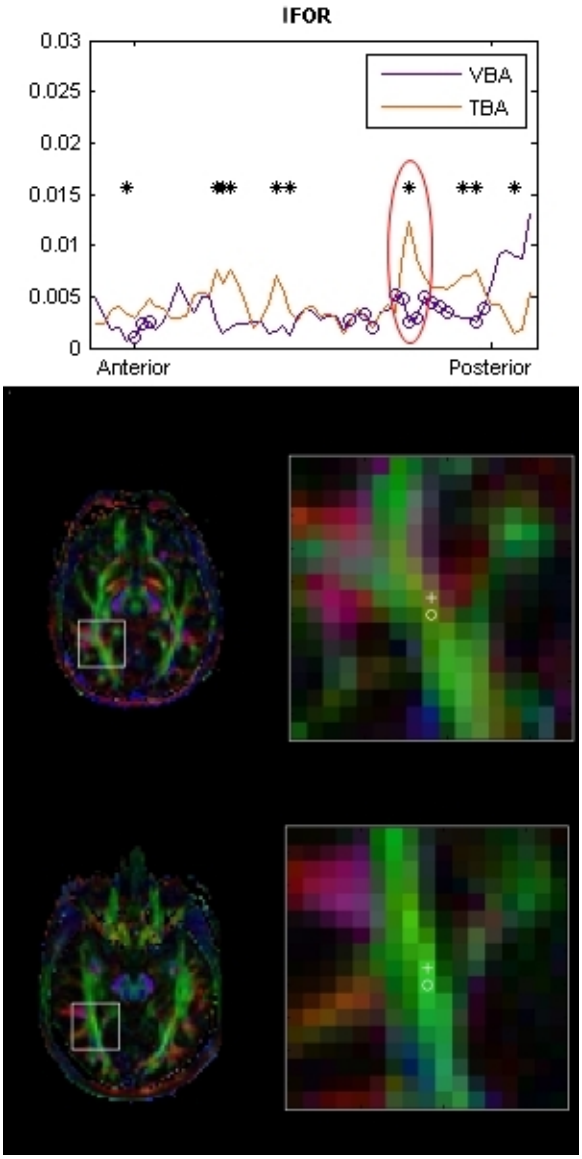

Figure 4.9: Example of different results in TBA and VBA due to misaligned tracts within larger WM structures. A region of significantly reduced FA in the SZ group was found in the right IFO by the VBA method only. The red ellipse in the plot of within-group variance (top) indicates the position along the tract that was investigated more closely. Color-coded FA maps of a SZ subject (middle) and a NC (bottom) are shown for reference. Point correspondence defined by the image normalization process in the VBA is indicated by the crosses, and point correspondence defined by the TBA method is indicated by the white circles. The VBA appears to be comparing two slightly differenct tracts at that point.

analysis relies on the accuracy of the algorithms for both fiber tracking and definition of point correspondence across subjects. However, the results of the semi-automated fiber tracking scheme implemented here suggest that consistent results across subjects can be obtained in several different WM pathways of interest, and the similarities in the shape of the plots of mean FA along the tracts between groups (Fig. 4.3 and 4.4) suggest that even the relatively simplistic methods used here to define point correspondence across subjects worked fairly well, particularly in the central portions of the tracts. The results become more questionable at the ends of the axes, where there is more variation in the tracjectories of the axes between subjects. For example, see the results at the temporal ends of the tracts for the AL (MTG) in Fig. 4.3 and the UL (PF) in Fig. 4.4. There is quite a bit of variation in the location of the temporal ends of the axes (posterior), yet points with similar arc lengths from the initial parameterization plane are considered to be corresponding. The variability between subjects could be driven by several factors, including poor image registration and poor tract parameterization. We chose to parameterize the tracts by their medial axes because the cores of several major WM tracts have a roughly cylindrical shape, which could easily be characterized by a streamline. However, as the WM tracts branch and fan out toward their cortical destinations, the assumption we have made about the tract shape is violated. We attempted to address this issue by trimming the fiber results to remove the portions of fibers that branch significantly. However, this relied on the image co-registration results, and subtle registration errors could have resulted in trimming too much or not enough off of fibers in different subjects, potentially altering the definition of the medial axis.

Another major limitation of the tract-based analysis method is that diffusion parameters can only be compared within the central core of relatively large WM pathways that can be easily tracked. While this does greatly reduce the amount of WM tissue that can be investigated compared to a voxel-wise analysis, it should be noted that the fiber branches extending to the cortex are much more prone to co-registration error and results in these regions should be interpreted with caution. Also, as Smith *et al.* [8] point out in their paper describing the tract-based spatial statistics (TBSS)

method, resolution limits in DTI studies lead to partial volume averaging along the edges of the WM tracts, reducing the accuracy of the diffusion parameters at these locations.

Recently, Van Hecke *et al.* introduced an image registration algorithm that takes the diffusion tensor components into account [31] during inter-subject normalization. This registration method is currently quite computationally costly and the methods for transforming the tensors could use improvement. However, it provides promise for being able to incorporate the benefits of voxel-based analysis and fiber tracking in a more unified approach than the tract-based approach we describe here. Not only are co-registration results within WM tracts improved over scalar-based registration methods, but the tensors are also transformed to the common image space, allowing fiber tracking to be performed directly in the common space.

The results of our study suggest that the tract-based analysis may provide a means of dealing with some of the shortcomings of a traditional voxel-based analysis, which relies heavily upon the assumption that the images are perfectly co-registered. It may be particularly useful in interpreting results from voxel-based analyses in regions where multiple major WM pathways travel near each other and are indistinguishable in the scalar images often used for image co-registration or in major WM pathways where image co-registration may produce unreliable results across subjects.

References

[1] Mori, S. et al. Imaging cortical association tracts in the human brain using diffusion-tensor-based axonal tracking. *Magnetic Resonance in Medicine*, 47(2):215–23, 2002.

[2] Fillard, P., Gilmore, J., Piven, J., Lin, W., and Gerig, G. *Quantitative Analysis of White Matter Fiber Properties along Geodesic Paths*. Medical Image Computing and Computer-Assisted Intervention. 2003.

[3] Gong, G. et al. Asymmetry analysis of cingulum based on scale-invariant parameterization by diffusion tensor imaging. *Human Brain Mapping*, 24(2):92–8, 2005.

[4] Gong, G. et al. Side and handedness effects on the cingulum from diffusion tensor imaging. *Neuroreport*, 16(15):1701–5, 2005.

[5] Partridge, S. C. et al. Tractography-based quantitation of diffusion tensor imaging parameters in white matter tracts of preterm newborns. *Journal of Magnetic Resonance Imaging*, 22(4):467–74, 2005.

[6] Xie, S. et al. Evaluation of bilateral cingulum with tractography in patients with Alzheimer's disease. *Neuroreport*, 16(12):1275–8, 2005.

[7] Jones, D. K. et al. Age effects on diffusion tensor magnetic resonance imaging tractography measures of frontal cortex connections in schizophrenia. *Human Brain Mapping*, 27(3):230–8, March 2006.

[8] Smith, S. M. et al. Tract-based spatial statistics: voxelwise analysis of multi-subject diffusion data. *Neuroimage*, 31(4):1487–505, 2006.

[9] Oldfield, R. C. The assessment and analysis of handedness: the Edinburgh inventory. *Neuropsychologia*, 9(1):97–113, March 1971.

[10] Netsch, T. and van Muiswinkel, A. Quantitative evaluation of image-based distortion correction in diffusion tensor imaging. *IEEE Transactions on Medical Imaging*, 23(7):789–798, 2004.

[11] Maes, F., Collignon, A., Vandermeulen, D., Marchal, G., and Suetens, P. Multimodality image registration by maximization of mutual information. *IEEE Transactions on Medical Imaging*, 16(2):187–98, 1997.

[12] Li, R. *Automatic placement of regions of interest in medical images using image registration*. M.S. Thesis in Electrical Engineering and Computer Science, Vanderbilt University, 2001.

[13] Rohde, G. K., Aldroubi, A., and Dawant, B. M. The adaptive bases algorithm for intensity-based nonrigid image registration. *IEEE Transactions on Medical Imaging*, 22(11):1470–9, 2003.

[14] Conturo, T. E. et al. Tracking neuronal fiber pathways in the living human brain. *Proceedings of the National Academy of Sciences of the United States of America*, 96(18):10422–7, 1999.

[15] Mori, S., Crain, B. J., Chacko, V. P., and van Zijl, P. C. Three-dimensional tracking of axonal projections in the brain by magnetic resonance imaging. *Annals of Neurology*, 45(2):265–9, 1999.

[16] Corouge, I., Gouttard, S., and Gerig, G. Towards a shape model of white matter fiber bundles using diffusion tensor MRI. In *IEEE International Symposium on Biomedical Imaging: Nano to Macro.*, pages 344–347 Vol. 1, 2004.

[17] Zhang, S., Correia, S., and Laidlaw, D. Identifying White-Matter Fiber Bundles in DTI Data Using an Automated Proximity-Based Fiber-Clustering Method. *IEEE Transactions on Visualization and Computer Graphics*, 14(5):1044–1053, 2008.

[18] Ding, Z., Gore, J. C., and Anderson, A. W. Classification and quantification of neuronal fiber pathways using diffusion tensor MRI. *Magnetic Resonance in Medicine*, 49(4):716–21, 2003.

[19] Corouge, I., Fletcher, P. T., Joshi, S., Gouttard, S., and Gerig, G. Fiber tract-oriented statistics for quantitative diffusion tensor MRI analysis. *Medical Image Analysis*, 10(5):786–98, 2006.

[20] Bullmore, E. T. et al. Global, voxel, and cluster tests, by theory and permutation, for a difference between two groups of structural MR images of the brain. *IEEE Transactions on Medical Imaging*, 18(1):32–42, 1999.

[21] Levene, H. Contributions to Probability and Statistics: Essays in Honor of Harold Hotelling. pages 278–292, Stanford, CA, 1960. Stanford University Press.

[22] Cheung, V. et al. A diffusion tensor imaging study of structural dysconnectivity in never-medicated, first-episode schizophrenia. *Psychological Medicine*, 38(6):877–85, June 2008.

[23] Douaud, G. et al. Anatomically related grey and white matter abnormalities in adolescent-onset schizophrenia. *Brain*, 130(9):2375–2386, 2007.

[24] Kyriakopoulos, M., Vyas, N. S., Barker, G. J., Chitnis, X. A., and Frangou, S. A Diffusion Tensor Imaging Study of White Matter in Early-Onset Schizophrenia. *Biological Psychiatry*, In Press, Corrected Proof, 2007.

[25] McIntosh, A. M. et al. White Matter Tractography in Bipolar Disorder and Schizophrenia. *Biological Psychiatry*, September 2008.

[26] Price, G. et al. White matter tracts in first-episode psychosis: a DTI tractography study of the uncinate fasciculus. *NeuroImage*, 39(3):949–55, February 2008.

[27] Seal, M. L. et al. Abnormal white matter microstructure in schizophrenia: a voxelwise analysis of axial and radial diffusivity. *Schizophrenia Research*, 101(1-3):106–10, April 2008.

[28] Seok, J. et al. White matter abnormalities associated with auditory hallucinations in schizophrenia: A combined study of voxel-based analyses of diffusion tensor imaging and structural magnetic resonance imaging. *Psychiatry Research: Neuroimaging*, 156(2):93–104, 2007.

[29] Shergill, S. S. et al. A Diffusion Tensor Imaging Study of Fasciculi in Schizophrenia. *The American Journal of Psychiatry*, 164(3):467–473, 2007.

[30] Szeszko, P. R. et al. Clinical and Neuropsychological Correlates of White Matter Abnormalities in Recent Onset Schizophrenia. *Neuropsychopharmacology*, 2007.

[31] Hecke, W. V. et al. Nonrigid coregistration of diffusion tensor images using a viscous fluid model and mutual information. *IEEE Transactions on Medical Imaging*, 26(11):1598–612, November 2007.

CHAPTER V

LATERALIZED DIFFERENCES IN WHITE MATTER TRACTS PASSING THROUGH THE EXTERNAL CAPSULE IN WILLIAMS SYNDROME

Introduction

We previously reported the discovery of several regions of both increased and decreased fractional anisotropy (FA) in white matter (WM) regions throughout the brain in a voxel-based analysis of diffusion tensor imaging (DTI) data in Williams syndrome (WS) [1]. WS is a disorder caused by a 1.5Mb hemizygous deletion on chromosome 7 (7q11.23), which results in a unique set of characteristic behavioral and cognitive dysfunctions. A major WM structure that contained clusters of both increased and decreased FA bilaterally was the external capsule (EC), which contains several WM pathways connecting to the frontal lobes. It is speculated that changes in diffusion properties of these tracts may be related to some of the behavioral and cognitive dysfunctions of the disorder, such as increased nonsocial anxiety, hypersociability, and ipaired visuospatial construction. However, one of the limitations of using a voxel-wise analysis is that it is difficult to interpret the involvement of distinct WM pathways in regions where several tracts travel together. In this study, we use a tract-based analysis method [2] to investigate the involvement of the two major white matter tracts that pass through the regions of significant differences found in the inferior portion of the external capsules: the uncinate and inferior fronto-occipital fasciculi.

Methods

Subjects

Informed consent was obtained from each subject according to the requirements of the Institutional Review Board. Artifact-free DTI data sets were collected from a total of 16 WS subjects and 16 normal controls. Structural images from an additional NC who did not have DTI data were

used as the initial target for creation of a study-specific template used in the image co-registration process. The WS group consisted of 6 females and 10 males; all but 3 subjects were right handed; their mean age was 24 years (range = 16 to 33 years). The NC group consisted of 8 females and 8 males; 12 NCs were right-handed, 3 were left-handed and one was ambidextrous; and their mean age was 23 years (range = 16 to 32 years). The target subject was a 19 year-old male who was right handed. A summary of the subject demographics is shown in Table 5.1. There was no significant difference in the mean age of the two groups (p = 0.255), and handedness was determined by the Edinburgh handedness inventory [3].

Table 5.1: Subject demographics

Group		N	Age (years)			Handedness		
			Range	Mean	Std. Dev.	Right	Left	Ambidextrous
Controls		16	16 - 32	23	4	12	3	1
	Male	8	18 - 32	23	5	5	2	1
	Female	8	16 - 26	22	4	7	1	0
Williams Syndrome		16	16 - 33	24	6	13	3	0
	Male	10	16 - 33	24	5	7	3	0
	Female	6	16 - 30	24	5	6	0	0

Image Acquisition

All images were acquired using a Philips Intera Achieva 3T MRI scanner with high-performance gradient coils (80 mT/m gradient strength and 100 mT/m/ms slew-rate) and an 8 channel SENSE (sensitivity encoding) head coil. Diffusion weighted images (DWIs) were acquired with 32 diffusion-encoding directions. Single-shot EPI and sensitivity encoding (SENSE) were used to decrease total

scan time. The imaging parameters used were TE = 60 ms, TR = 10,000 ms, SENSE factor = 2, tr(b) = 1000 s/mm^2, FOV = 256 x 256 mm^2, and a matrix size of 128 x 128. Whole-brain coverage was obtained with 60 axial slices in 6 minutes. A high-resolution, T1-weighted 3D anatomical volume was acquired using a multi-shot gradient echo sequence with TE = 4.6 ms, TR = 8.9 ms, SENSE factor = 2, FOV = 256 x 256 mm^2. The volume consisted of 170 sagittal slices with an isotropic voxel size of 1 mm^3, and total scan time was 4 minutes and 24 seconds.

Image Processing

Eddy current distortion and in-plane bulk subject motion were corrected prior to tensor calculation. Normalization of the FA maps was performed in two major steps. First, a study-specific FA template was created by normalizing each subject's FA map to the target T1-weighted image space and then averaging the resulting images. second, the original FA maps were co-registered directly to the template to reduce potential bias introduced from the selection of a single normal control as the initial target. See Arlinghaus *et al.* [1] for details.

Tract-based analysis

The left and right inferior fronto-occipital fasciculi and uncinate fasciculi were segmented, parameterized, and compared by methods described previously [2]. Briefly, fiber tracking was performed in the native image space of each subject to segment each tract-of-interest. The central axes of the resulting fiber tracts were defined for each subject in a way that also defined point correspondence across subjects. Finally, FA values were compared between groups at corresponding locations along each tract with a two-sample t-test and thresholded at a significance level of $p < 0.05$ (uncorrected).

Results

The right and left uncinate and the left inferior fronto-occipital tracts were successfully tracked in each subject. The right inferior fronto-occipital tract was successfully tracked in all NCs and all

but 2 WS subjects, where only a single fiber was found in this tract. Figure 5.1 shows the plots of mean FA as a function of position along the tracts, as well as projections of the mean axes for each subject (in the common image space) with regions of significant differences highlighted. The left uncinate contained two large regions of increased FA and a small region of decreased FA in the portion passing through the EC in the WS group compared to NCs. An additional small region of reduced FA was also found in the temporal portion of the tract. The right uncinate contained a region of reduced FA at the anterior extent of the portion passing through the EC, as well as a small region of reduced FA in the portion of the tract extending into frontal WM. The left IFO contained a single region of reduced FA in the portion passing through the EC, as well as an additional region of reduced FA in the temporal portion of the tract and two regions of increased FA in the posterior portion of the tract. The right IFO contained a large region of increased FA in the portion passing through the EC, as well as an additional region of increased FA in the temporal portion of the tract.

Discussion

We compared FA values between a group of young adults with WS and a group of normal controls along the uncinate and inferior fronto-occipital fasciculi, the two major WM pathways that pass through the inferior portion of the external capsules, and found regions significantly different FA in all four tracts. Our results were consistent with the findings from the same groups in a voxel-based study [1] and the two other previously published studies of WS with DTI [4, 5]. In a TBSS study of 10 WS subjects compared with 10 typically developing controls, Hoeft *et al.* reported regions of increased FA in the bilateral external capsule and bilateral regions of WM containing the inferior longitudinal fasciculi and the inferior fronto-occipital fasciculi. In a study of 5 high-functioning WS subjects compared to age-, gender-, and IQ-matched controls, Marenco *et al.* [5] reported increased anisotropy in the bilateral tract-based regions of interest in the IFO and no significant differences in the uncinate fasciculi. Discrepancies between these two studies and ours are most likely due to methodological differences between the studies. The analysis methods used by Hoeft

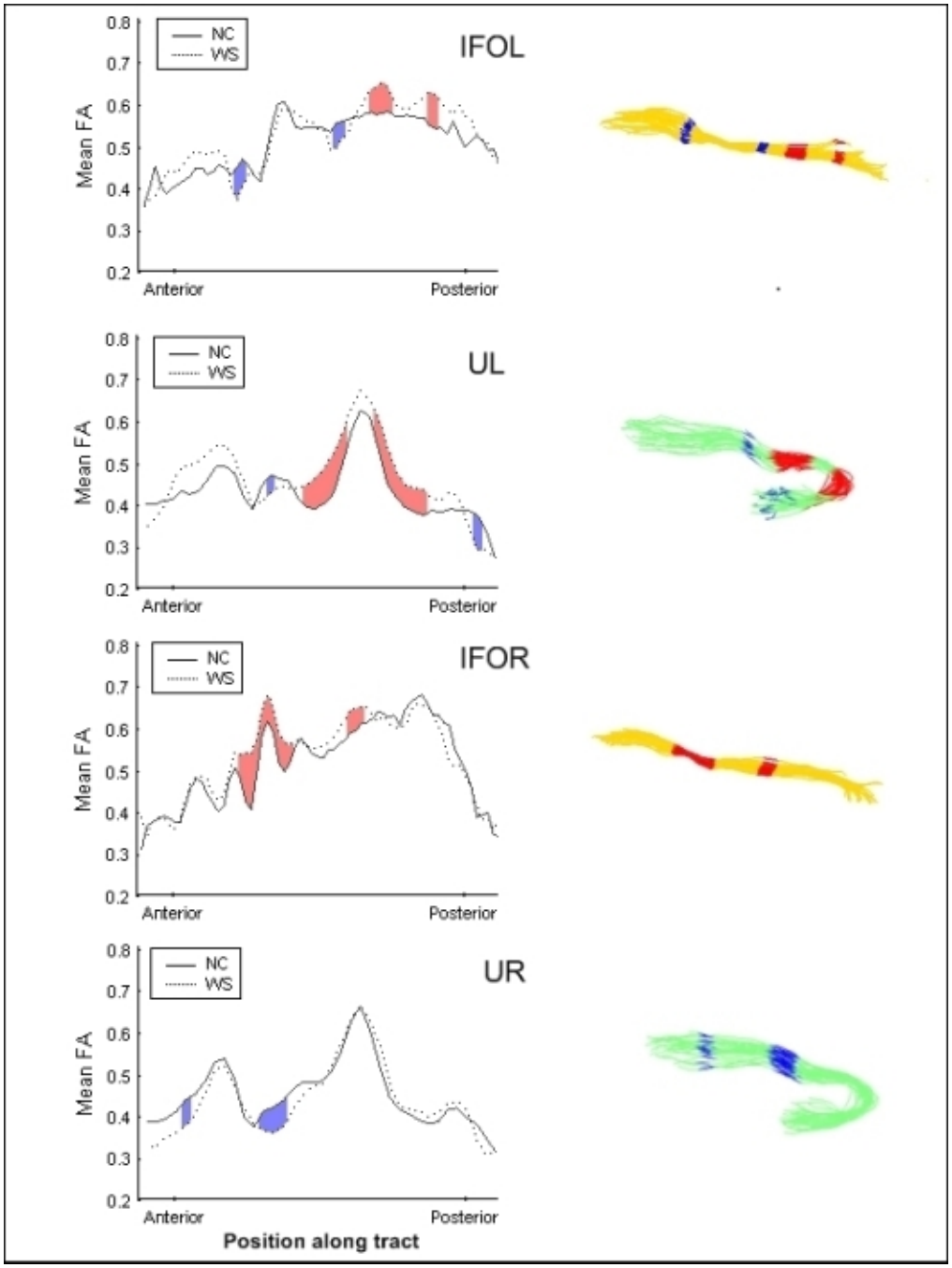

Figure 5.1: TBA results in the external capsule. On the left, the mean FA of each group is plotted as a function of position along the fiber tract. On the right, projections of the corresponding central axes for each subject are displayed in the common image space. Regions of significantly ($p < 0.05$) reduced and increased FA in the WS group compared to the NCs, are marked in blue and red, respectively.

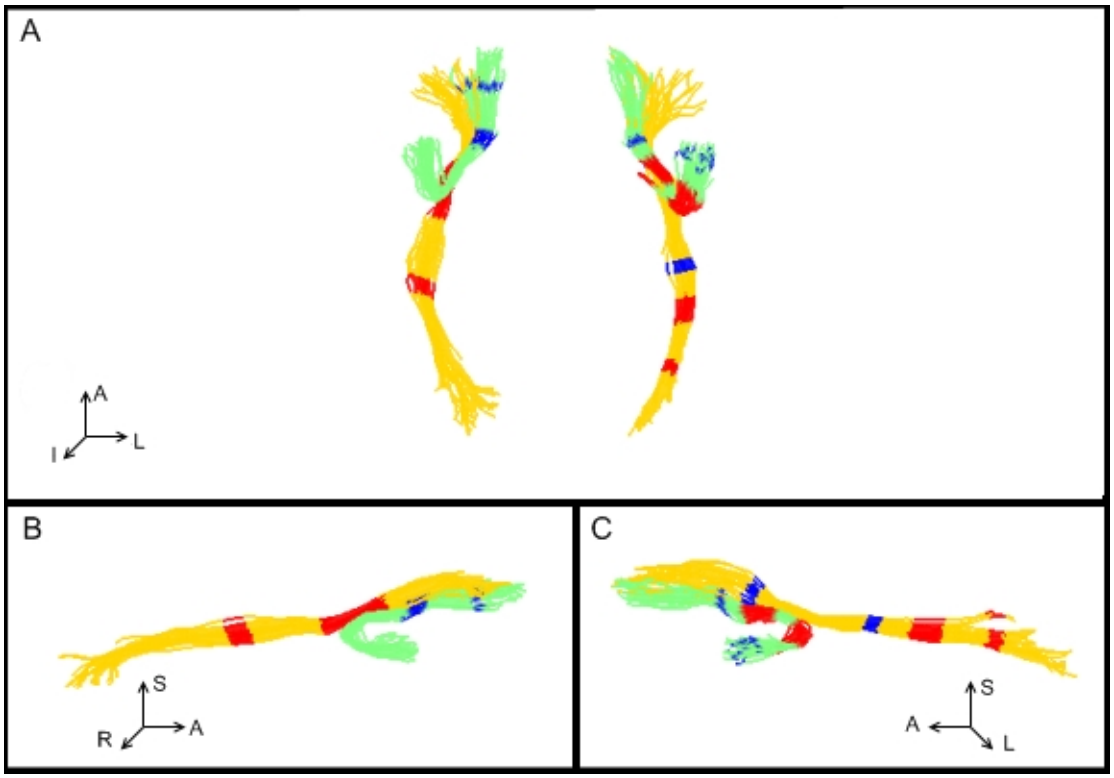

Figure 5.2: The spatial relationship of tract-specific changes in the external capsules. The mean axes of the right and left uncinate (green) and inferior fronto-occipital (yellow) fasciculi from each subject are displayed together with a view from below (A), from the right (B), and from the left (C). Regions of significantly reduced and increased FA are marked in blue and red, respectively. Orientation is marked as follows: anterior (A), left (L), right (R), superior (S), and inferior (I).

et al. and Marenco *et al.* cannot distinguish between neighboring fiber pathways in large WM regions through which multiple tracts pass, like the external capsule.

The semi-automated fiber tracking scheme utilized in this study performed well, except in the right IFO of two WS subjects. Fiber tracking with manually defined ROIs revealed that there were a few fibers connecting the frontal and occipital lobes in both cases. However, in the first subject, the frontal portion of the tract branched off laterally immediately after passing through the external capsule and did not contain any fibers that continued on to the prefrontal cortex as in the other subjects. In the other subject, the right IFO appeared to have connections with the prefrontal cortex, but very few with medial occipital cortex, as in the other subjects. Inspection of the DTI data for these two subjects revealed no obvious image artifacts that might have affected the fiber tracking.

The results from the voxel-based comparison of these data suggested that the FA differences in the EC were fairly homologous between hemispheres. However, the results of this tract-specific comparison indicate that the left and right uncinate fasciculi and IFO each contribute to changes in FA in the EC in different ways. This is not entirely surprising in the uncinate fasciculi, which connect regions in the frontal (mainly orbitofrontal) lobes with regions in the temporal lobes, including the amygdala [6, 7]. There is evidence of lateralization in the function of the amygdala [8], and an fMRI study of WS designed to invoke activation in the amygdala from threatening visual stimuli by Meyer-Lindenberg *et al.* [9] revealed reduced activation in the amygdalae of WS subjects compared to normal controls, with the difference much more pronounced in the right hemisphere. Further investigation of the functional network involved in this observed dysfunction suggested that normal functional connections between different regions of frontal cortices and the amygdala may be disrupted. While the path analyses implemented by Meyer-Lindenberg *et al.* are not meant to be interpreted as direct connections between anatomical locations, it is certainly possible that the reduced FA observed in the right uncinate is involved. In normal subjects, the left IFO tract possibly plays a role in semantic processing in language ability [10]. A review of studies investigating semantic ability in WS suggests that semantic fluency may not necessarily be impaired [11].

Although, Jarrold *et al.* [12] report high incidence of repeating words during semantic tasks, suggesting the possibility that higher-level inhibition processes in language may be dysfunctional. The right IFO is involved in normal face processing [13]. Normal activation of the ventral processing stream during face processing has been reported [14–16], which is in agreement with behavioral data suggesting that face processing is relatively preserved in WS [17]. However, regions that may be involved in higher-level object recognition and face processing have been shown to function abnormally [14, 16], suggesting that compensatory processing methods may be invoked, providing relatively persevered face and object recognition.

The methods used in the paper allowed us to investigate the role of specific white matter tracts in behavioral and cognitive dysfunction in Williams syndrome and demonstrate their usefulness. To the best of our knowledge, it is the first of its kind in the study of Williams syndrome. Previous DTI studies that included fiber tracking could not identify localized changes within the tracts or assign involvement to particular tracts in regions of WM where multiple fiber pathways traveled together. Hopefully, more precise knowledge of the specific WM tracts affected in WS will aid in the design of future functional, structural, and behavioral studies of the disorder.

References

[1] Arlinghaus, L. R., Thornton-Wells, T. A., Dykens, E. M., and Anderson, A. W. Altered diffusion properties in white matter in Williams Syndrome. In preparation.

[2] Arlinghaus, L. R., Dawant, B. M., Meltzer, H. Y., Park, S., and Anderson, A. W. Semi-automated, tract-based analysis of diffusion tensor imaging studies. In preparation.

[3] Oldfield, R. C. The assessment and analysis of handedness: the Edinburgh inventory. *Neuropsychologia*, 9(1):97–113, March 1971.

[4] Hoeft, F. et al. More is not always better: increased fractional anisotropy of superior longitudinal fasciculus associated with poor visuospatial abilities in Williams syndrome. *The Journal of Neuroscience*, 27(44):11960–5, October 2007.

[5] Marenco, S. et al. Genetic contributions to white matter architecture revealed by diffusion tensor imaging in Williams syndrome. *Proceedings of the National Academy of Sciences of the United States of America*, 104(38):15117–22, September 2007.

[6] Moran, M. A., Mufson, E. J., and Mesulam, M. Neural inputs into the temporopolar cortex of the rhesus monkey. *The Journal of Comparative Neurology*, 256(1):88–103, 1987.

[7] Ebeling, U. and von Cramon, D. Topography of the uncinate fascicle and adjacent temporal fiber tracts. *Acta Neurochir (Wien)*, 115(3-4):143–8, 1992.

[8] Baas, D., Aleman, A., and Kahn, R. S. Lateralization of amygdala activation: a systematic review of functional neuroimaging studies. *Brain Research Reviews*, 45(2):96–103, May 2004.

[9] Meyer-Lindenberg, A. et al. Neural correlates of genetically abnormal social cognition in Williams syndrome. *Nature Neuroscience*, 8(8):991–993, 2005.

[10] Duffau, H., Gatignol, S. T. P., Mandonnet, E., Capelle, L., and Taillandier, L. Intraoperative subcortical stimulation mapping of language pathways in a consecutive series of 115 patients with Grade II glioma in the left dominant hemisphere. *Journal of Neurosurgery*, 109(3):461–71, September 2008.

[11] Brock, J. Language Abilities in Williams Syndrome: A Critical Review. *Development and Psychopathology*, 19(01):97–127, 2007.

[12] Jarrold, C., Hartley, S. J., Phillips, C., and Baddeley, A. D. Word fluency in Williams syndrome: Evidence for unusual semantic organisation? *Cognitive Neuropsychiatry*, 5(4):293–319, 2000.

[13] Thomas, C. et al. Reduced structural connectivity in ventral visual cortex in congenital prosopagnosia. *Nature Neuroscience*, November 2008.

[14] Mobbs, D. et al. Anomalous brain activation during face and gaze processing in Williams syndrome. *Neurology*, 62(11):2070–6, June 2004.

[15] Meyer-Lindenberg, A. et al. Neural basis of genetically determined visuospatial construction deficit in Williams syndrome. *Neuron*, 43(5):623–31, September 2004.

[16] Sarpal, D. et al. A genetic model for understanding higher order visual processing: functional interactions of the ventral visual stream in williams syndrome. *Cerebral Cortex*, 18(10):2402–9, October 2008.

[17] Landau, B., Hoffman, J. E., and Kurz, N. Object recognition with severe spatial deficits in Williams syndrome: sparing and breakdown. *Cognition*, 100(3):483–510, July 2006.

CHAPTER VI

DISCUSSION

The application of diffusion tensor imaging (DTI) to the study of white matter (WM) tissue in the brain is rapidly increasing. The voxel-wise comparison of fractional anisotropy (FA) measurements in Williams syndrome (WS) presented in Chapter 3 provides an example of one of the newest clinical applications of DTI. The results of this study revealed several regions of both decreased and increased FA in WM regions that appear to correspond to anatomical, functional, and behavioral data previously reported; and genetic evidence suggests that these changes are most likely due to problems in the organization of the axons, not changes to the myelin content of the WM tissue. This study also demonstrated some of the advantages and limitations of a voxel-based comparison of DTI data. Voxel-based analyses (VBA) allow a whole-brain, exploratory approach, requiring no *a priori* knowledge of the location or extent of the changes in WM. However, Type I errors due to misregistration and changes detected in large regions of WM containing multiple fiber tracts make it difficult to interpret results found by VBA.

These limitations motivated the development of the tract-based analysis (TBA) method presented in Chapter 4. This new TBA method utilizes image co-registration to isolate WM tracts of interest in each subject in a semi-automated fashion and parameterize them in such a way that spatially localized statistical comparisons can be made between groups along the tracts. The image co-registration process provides the benefit of allowing a traditional VBA to be performed, as well. The TBA and VBA methods were compared in a study of schizophrenia, and the results suggested that the tract-based method may provide a more accurate comparison of a given tract of interest in two cases: (1) regions where large WM structures are misregistered and (2) regions where large WM structures may be well registered, but the individual WM pathways passing through the structures are not.

In Chapter 5, the new TBA method was applied to the data from the DTI study of WS described

in Chapter 3. The VBA performed in the previous study revealed regions of both decreased and increased FA in the WS subjects compared to the normal controls (NC) in the inferior portion of the bilateral external capsules. In this study, TBA was used to investigate the involvement of the two major pathways passing through this portion of the external capsule, and the results suggested that the changes detected in the inferior portion of the external capsule by the VBA were due to lateralized changes in both pathways - an observation that was not possible to make with previous analysis methods.

While the results of the application of this new method are promising, there are several limitations that should be discussed. First, the tract-based method relies upon the co-registration results from the voxel-based analysis. We attempted to minimize the effects of misregistration by performing multi-ROI fiber tracking with large seed ROIs in the native image space of each subject. We also investigated relatively large fiber tracts because they lie within regions of WM where image co-registration typically performs well and because current image resolution levels prevent the investigation of fiber tracts with diameters less than or nearly equal to the voxel width. The tracts we investigated also do not have major intersections with other large fiber tracts, which could result either in premature termination of the tracts because of low FA values or in misleading tracking results if the algorithm follows the wrong pathway.

The choice to parameterize each tract by a single streamline along its medial axes limited the extent of the tract that could be compared between subjects. However, WM structures are affected by partial volume averaging along their edges and as they spread out to their cortical destinations, and the extent of the effects within the tracts will vary between subjects. Therefore, it may be that it is best to only compare diffusion parameters along the central cores of WM structures to minimize the effects of partial volume averaging. The choice of a streamline may also not be appropriate for large WM structures, such as the corpus callosum and the cortico-spinal tracts, that might be more accurately parameterized as sheet-like surfaces at their cores instead. Although, more elaborate shapes would introduce more complexity to the definition of point correspondence between subjects, which is a challenge even with simple streamlines. We chose a relatively simple

approach [1] that based correspondence upon arc length and relative position from the plane used to initialize reparameterization of the axes. Perhaps more accurate results could be obtained by taking the curvature of the axes or even cross-sectional shape of the tract into account.

As mentioned above, we chose to perform fiber tracking in the native image space of each subject and transform the medial axes of the tracts to the common image space to assist in the definition of point correspondence. An alternate approach would be to co-register the tensor data and perform both the VBA and the fiber tracking (and TBA) in the common image space. The advantage of this approach is that fiber tracts from different subjects would be inherently co-registered. However, the major disadvantages are that the method is even more reliant upon the accuracy of co-registration of individual WM pathways results and that a robust algorithm for rotating the tensors is necessary. The feasibility of such an approach has increased with the recent development of registration algorithms optimized for normalization of DTIs [2, 3]. Van Hecke *et al.* recently used their multi-channel DTI registration algorithm [3] to create a population-based atlas that provides a more accurate result than normalization based upon a subject-specific template [4]. However, the method is still susceptible to small registration errors that can significantly affect the tensor rotation, which would affect subsequent statistical comparisons, and creation of a population-based atlas is computationally expensive.

Interest in developing analysis methods specific to DTI has been increasing as the field grows. A new tract-based analysis method for group comparison of DTI data was presented here. The method was applied to studies of schizophrenia and Williams syndrome, and results of these studies suggest that a combination of the exploratory benefits of a voxel-wise comparison and the specificity of a tract-based analysis may be able to provide more information than either method does in isolation.

References

[1] Corouge, I., Fletcher, P. T., Joshi, S., Gouttard, S., and Gerig, G. Fiber tract-oriented statistics for quantitative diffusion tensor MRI analysis. *Medical Image Analysis*, 10(5):786–98, 2006.

[2] Park, H.-J. et al. Spatial normalization of diffusion tensor MRI using multiple channels. *NeuroImage*, 20(4):1995–2009, December 2003.

[3] Hecke, W. V. et al. Nonrigid coregistration of diffusion tensor images using a viscous fluid model and mutual information. *IEEE Transactions on Medical Imaging*, 26(11):1598–612, November 2007.

[4] Hecke, W. V. et al. On the construction of an inter-subject diffusion tensor magnetic resonance atlas of the healthy human brain. *NeuroImage*, 43(1):69–80, October 2008.

APPENDIX A

IMAGE ARTIFACTS

Images acquired with an echo planar imaging (EPI) acquisition scheme, such as the diffusion tensor images (DTI) in the Williams syndrome and schizophrenia studies discussed in this dissertation, are inherently susceptible to several types of image artifacts. A common artifact in DTI that affected both studies is signal dropout due to motion. The DTI data in the schizophrenia study were affected in varying degrees by two additional types of artifacts caused by signal spikes in k-space and incomplete fat saturation. Descriptions of these three artifacts and the methods implemented to detect them are discussed below.

Artifact descriptions

Signal dropout due to motion

Severe subject motion results in rigid-body rotation and translations, and pulsatile flow of blood through large vessels and cerebrospinal fluid (CSF) through the ventricles results in nonlinear deformation of the surrounding brain tissue on the order of 1 mm [1]. Both types of motion can cause intravoxel dephasing of spins, decreasing the measured signal and resulting in what is referred to as *signal dropout* in the image. Examples are shown in Figure A.1.

Spike artifacts

The signal that is measured in a magnetic resonance imaging study is sampled at a predetermined range of spatial frequencies values which corresponds to the field of view of the image. This is referred to as *k-space*, and an image is obtained by applying the Fourier transform to the 2D or 3D k-space data. If an individual data point in k-space is corrupted by additional signal from sources such as static discharge in the subject's clothing or arcing from loose wires within the scanner, it will

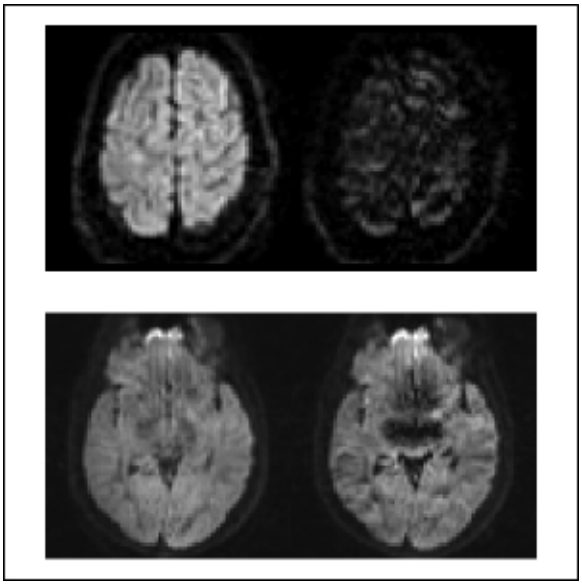

Figure A.1: Examples of signal dropout. Top: Axial slice from a diffusion-weighted image volume with normal signal (left) and with severe signal dropout due to subject motion (right). Bottom: Axial slice from a diffusion-weighted image volume with normal signal (left) and with signal dropout due to pulsatile motion of the brain (right).

appear as a spike in k-space. The reconstructed image will contain a periodic artifact at the corresponding spatial frequency. The orientation and period of the artifact are given by the orientation and distance, respectively, of the spike relative to the origin of k-space. For example, see Figure A.2.

Incomplete fat saturation

The protons in fat and water precess at different frequencies. Depending on the image acquisition scheme and parameters, this difference can lead to the signal from fat being spatially shifted relative to signal from water. EPI sequences are particularly susceptible to this *chemical shift* artifact in the phase encoding direction. Fat saturation techniques are typically employed to eliminate the signal from fat, preventing it from being shifted into voxels containing signal from other tissue types. However, several factors, including inhomogeneities in the RF field and local magnetic susceptibility differences, can result in incomplete fat suppression. Also, if chemical shift artifacts occur in images

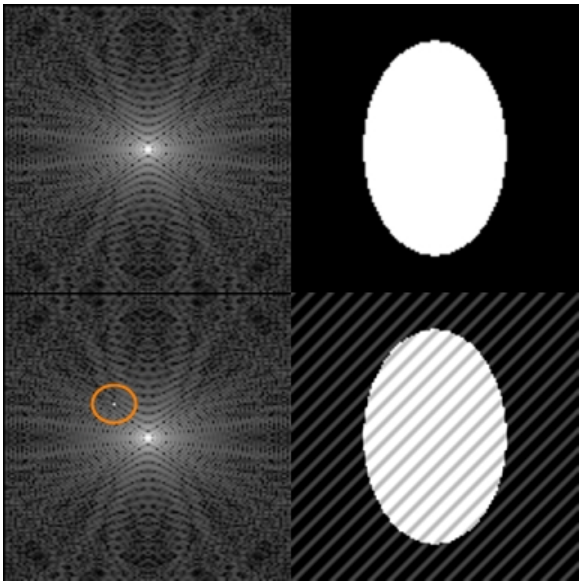

Figure A.2: The effects of spike artifacts. Top: The k-space data (left) for an example image (right). Bottom: The same k-space data with a single point contaminated by a spike in the signal (circle) results in a periodic artifact in the reconstructed image (right).

acquired with parallel imaging techniques, such as SENSE, reconstruction artifacts can cause the artifacts to become ghosted into the center of the image, contaminating even more voxels. See Figure A.3 for examples.

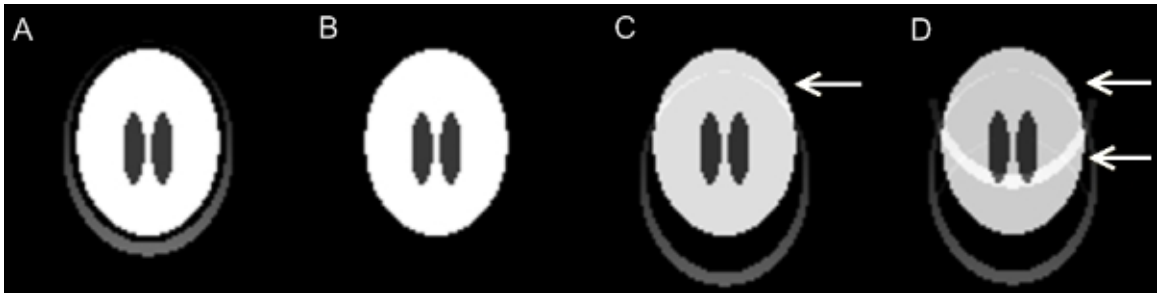

Figure A.3: The effects of incomplete fat saturation in EPI. In an inhomogeneous sample containing multiple tissue types, such as CSF (black), brain tissue (white), and subcutaneous fat (grey) (A), proper fat saturation completely suppresses the fat signal from images acquired with EPI (B). However, if fat saturation is incomplete in the EPI acquisition (C), the signal from fat is shifted along the phase encoding direction (vertically, in this case), corrupting voxels containing signal from other types of tissue (arrow). SENSE reconstruction artifacts can increase the number of corrupted voxels by causing ghosting of the artifacts into the center of the image (D).

Signal dropout due to motion

The tensor fitting algorithm in the PRIDE Fiber Tracking tool was modified to automatically detect and reject data points corrupted by signal dropout from the voxel-wise tensor fit. These corrupted data points lead to large residuals in the tensor fit, which are easily detected. We assume that the residuals of the tensor fit are normally distributed with a with a mean of zero. We screen for residuals with absolute values greater than three standard deviations (3σ) from the mean (μ), and exclude data points from the tensor recalculation with outliers that violate the threshold.

Figure A.4: Rejection of outlier residuals. The residuals of the tensor fit are assumed to be normally distributed, and data points with residuals greater than 3 standard deviations ($|z| = 3$) away from the mean are considered to be outliers.

The estimated mean and standard deviation of the residuals will be biased by outliers, so the value of σ must be calculated in way that is robust to the effects of the outliers. The standard value of each residual (r) is defined as

$$z = \frac{r - \mu}{\sigma}. \tag{A.1}$$

By determg the value of the residuals that correspond to the 25^{th} (r_{25}) and the 75^{th} (r_{75}) percentiles, the value of σ can be solved for, since μ is assumed to be zero and the standard values for the 25^{th} (z_{25}) and 75^{th} (z_{75}) percentiles can be found in any standard normal table. The values of r_{25} and r_{75} are determined by

$$r_{25} = \mathbf{MEDIAN}(r < 0) \tag{A.2}$$

and

$$r_{75} = \mathbf{MEDIAN}(r > 0), \tag{A.3}$$

respectively, and, for a normal distribution,

$$z_{25} = -0.6745 \tag{A.4}$$

and

$$z_{75} = 0.6745. \tag{A.5}$$

Plugging these values into Eq. A.1 gives

$$-0.6745 = \frac{r_{25} - \mu}{\sigma} \tag{A.6}$$

and

$$0.6745 = \frac{r_{75} - \mu}{\sigma}. \tag{A.7}$$

Rearranging and combining Eqs. A.6 and A.7 gives

$$-0.6745\sigma - r_{25} = 0.6745\sigma - r_{75}, \tag{A.8}$$

from which σ can be calculated:

$$\sigma = \frac{r_{75} - r_{25}}{1.349}. \tag{A.9}$$

Spike artifacts

A standalone program was written to detect spike artifacts on a slice-by-slice basis. The raw k-space data are generally not saved due to storage limitations, so the Fourier transform was applied to each 2D image to obtain the spectral image (K). The magnitude of the spike does not have to be large relative to the peak spectral intensity to produce the periodic artifact in the image space; it just has to be large relative to the values in its local neighborhood. Therefore, the sliding-window, median peak detector method described by Aizenberg *et al.* [2] was used. Because a large portion of the spectral power lies at the center of the spectral image, this central portion (C) of the spectrum was ignored. For all points outside the center mask, the ratio of the intensity of the current voxel $K(i,j)$ and the median value of all voxels within a window of $m \times m$ voxels, centered about the current voxel $(\underset{m\times m}{\mathbf{MED}}(K_{ij}))$, was calculated. Points where the ratio was greater than a user-determined threshold (θ),

$$\frac{K_{ij}}{\underset{m\times m}{\mathbf{MED}}(K_{ij})} \geq \theta \quad for \ (i,j) \notin C, \tag{A.10}$$

were considered to be spikes. Images with detected spikes were removed from subsequent analysis.

The size of the central mask was determined separately for each image so that it masked out a circular region containing 15% of the total power in the spectrum. The window size used was 11×11 voxels and $\theta = 10$. To reduce the number of false positives, points with $\theta > 10$ were only considered to be spikes if the spectral intensity at that location was at least 1% of the maximum spectral intensity, as this threshold was found to be necessary for significant changes in FA values.

Several steps were taken to speed up the computing time. First, only the central region of the image (64 x 64 voxels) was transformed. Second, image volumes were acquired with 92 total diffusion weighting directions, which consisted of 46 unique directions and their opposites. For each unique diffusion direction, the two images with equal but opposite weighting were subtracted, highlighting image artifacts. This difference image was transformed and subjected to the peak detector, and measures were taken to assign any detected artifacts to the proper image.

Incomplete fat saturation

Voxels corrupted by chemical shift artifacts were detected on a voxel-wise basis during tensor calculation. The residuals of the final tensor fit, after removing data points corrupted by spike artifacts and rejection of outliers due to signal dropout, were used to estimate a measure of the uncertainty in the estimation of the FA value [3]. This uncertainty measure was calculated by performing a wild bootstrap analysis with the final residuals of the tensor fit, estimating a value of FA at each iteration (FA_i^*), and then calculating the standard deviation of the FA estimates over iterations:

$$STD(FA^*) = \sqrt{\sum_{i=1}^{N} \frac{(FA_i^* - \overline{FA_i^*})^2}{N-1}}, \tag{A.11}$$

where N is the total number of iterations. If STD(FA^*) was greater than a user-defined threshold, then the voxel was considered to be corrupted and removed from further analysis.

The threshold used for the schizophrenia study was 0.065. This value was determined using six control data sets that were unaffected by major image artifacts. A histogram of the $STD(FA^*)$ values for voxels with $FA > 0.2$ from all 6 data set was created, and the $STD(FA^*)$ value associated with the 97.7^{th} percentile (2 standard deviations in a one-tailed normal distribution) was chosen as the threshold.

References

[1] Poncelet, B. P., Wedeen, V. J., Weisskoff, R. M., and Cohen, M. S. Brain Parenchyma Motion - Measurement with Cine Echo-Planar Mr Imaging. *Radiology*, 185(3):645–651, 1992.

[2] Aizenberg, I., Butakoff, C., Astola, J., and Egiazarian, K. Nonlinear Frequency Domain Filter for the Quasi-Periodic Noise Removal. In *International TICSP Workshop on Spectral Methods and Multirate Signal Processing*, TICSP Series #17, pages 147–153, Toulouse, France, 2002.

[3] Zhu, T., Liu, X., Connelly, P. R., and Zhong, J. An optimized wild bootstrap method for evaluation of measurement uncertainties of DTI-derived parameters in human brain. *NeuroImage*, 40(3):1144–56, April 2008.